Technical Physics Letters, Vol. 26, No. 4, 2000, pp. 269–271. Translated from Pis'ma v Zhurnal Tekhnicheskoĭ Fiziki, Vol. 26, No. 7, 2000, pp. 1–7.

The Effect of Hydrogenation on the Photoconductivity of Ion-Doped Gallium Arsenide Structures

V. A. Kagadeĭ[1)], Yu. V. Lilenko[1)], L. S. Shirokova[2)], D. I. Proskurovskiĭ[2)]

[1)] *Institute of Semiconductor Devices, State Research and Production Enterprise, Tomsk, Russia*

[2)] *Institute of High-Current Electronics, Siberian Division, Russian Academy of Sciences, Tomsk, 634055 Russia*

Received August 26, 1999

Abstract—It was found that the hydrogenation of ion-doped n^+–n–n_i-GaAs structures in atomic hydrogen increases the rate of conductivity relaxation in the doped layers, decreases the effect of bias voltage applied to the n^+-GaAs layer on the photoconductivity, and improves characteristics of the Schottky barrier transistors and the related integrated circuits. These phenomena are probably due to the formation of hydrogen complexes with electrically active centers in GaAs. *© 2000 MAIK "Nauka/Interperiodica".*

As is known [1, 2], the hydrogenation of single-crystal Si and GaAs by exposure to atomic hydrogen results in the passivation of many shallow and deep centers. Most investigations devoted to the hydrogenated GaAs were performed on the structures doped in the course of epitaxial growth [3, 4], while the ion-doped systems were studied to a much lower extent. The ion-doped materials differ from the epitaxially-grown ones by the presence of a large number of various defects detrimentally affecting the semiconductor properties. Therefore, investigations aimed at the development of methods for the suppression of electrical activity of deep centers in the ion-doped GaAs are obviously of importance. Recently [5] we have demonstrated that hydrogenation leads to a decrease in the level of parasitic feedback via support in the ion-doped GaAs-based structures. It would be also of interest to study how can hydrogenation affect some other properties of these structures. In this work, we have studied for the first time the effect of hydrogenation on the photoconductivity of ion-doped GaAs structures. Below, we will present data showing evidence that the exposure to atomic hydrogen has a positive effect upon the parameters of Schottky barrier transistors and related integrations.

The experiments were performed on the n^+–n–n_i structures obtained by implanting Si^+ ions into semi-insulating GaAs substrates. The electron concentration in the contact n^+-GaAs layer was $n_e = (1.5–2) \times 10^{18}$ cm^{-3}, and that in the active n-GaAs layer, $n_e = 3 \times 10^{17}$ cm^{-3}. The samples were hydrogenated in a flow of atomic hydrogen using a setup described elsewhere [6, 7]. The sample temperature during the hydrogenization was T = 100–300°C, the hydrogen pressure was 10^{-2} Pa, and the treatment duration was t = 5–90 min. The complete restoration of electron concentration in the ion-doped layer upon hydrogenation was achieved by annealing the samples at 400–475°C for 1–10 min [5] and checked by measuring the capacitance–voltage characteristics be a mercury-probe technique. The photoconductivity of the n^+–n–n_i-GaAs structures was measured by a contactless method proposed in [8, 9]. The photoconductivity kinetics was studied by measuring the photoresponse decay U_f upon excitation of the minority carriers by the pulsed radiation of a red light-emitting diode (pulse duration, 1 s; wavelength, $\lambda \cong 670$ nm) with a reverse bias voltage applied to the contact n^+ layer. The time variation of the photoconductivity was measured upon converting the $U_f(t)$ signal into a digital code, followed by storage, processing, and reproduction on a plotter.

Figure 1 shows the curves $U_f(t)$ representing kinetics of the photoconductivity signal. At the moment of arrival of the photoexcitation pulse, the U_f value exhibits a jump indicative of a sharp drop in resistivity of the n^+–n–n_i structure, which remains virtually constant during the pulse. For the initial sample (Fig. 1a), the shape of the curves describing restoration of the initial resistance after termination of the pulse is determined by two components of the photoconductivity relaxation–fast and slow. The fast relaxation of the charge carriers immediately upon termination of the photoexcitation pulse is manifested by a sharp decrease in the photoconductivity signal. The slow relaxation of the carriers proceeds over a period several seconds (6–12 s), as evidenced by a long decay in the U_f signal intensity. The duration of the signal decay increases with the bias voltage applied to the n^+-GaAs layer.

After the hydrogenation treatment (Fig. 1b), the shape of the leading front and the "step" on the $U_f(t)$ cures remains virtually unchanged, while the relaxation curves are significantly modified. The shape of these curves indicates that the photoconductivity relaxation on the whole proceeds at an increased rate, with the signal component corresponding to the slow relaxation

1063-7850/00/2604-0269$20.00 © 2000 MAIK "Nauka/Interperiodica"

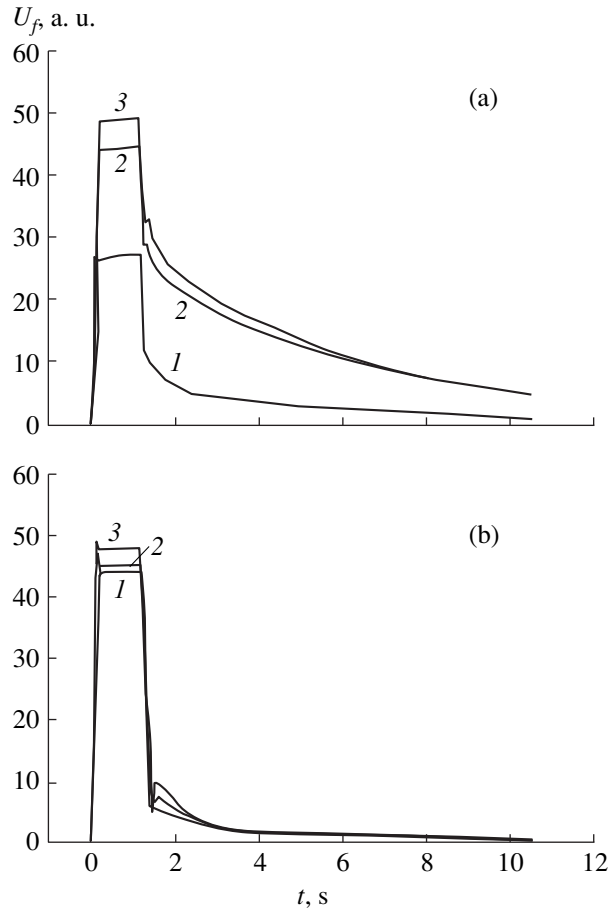

Fig. 1. Plots of the photoconductivity signal intensity U_f versus time t for the photoexcited n^+–n–n_i-GaAs structures grown on the (a) initial and (b) hydrogenated (T = 150°C, t = 30 min) and annealed substrate. The measurements were performed at a bias voltage applied to the n^+-GaAs layer (V): (*1*) 0; (*2*) 10; (*3*) 20.

being markedly decreased. This behavior suggests a decrease in the contribution of processes related to the slow relaxation. In addition, the hydrogenation treatment decreased the effect of bias voltage on the relaxation duration.

It should be also noted that the initial sample exhibits a significant dependence of the photoconductivity signal amplitude U_f^* on the reverse bias voltage applied to the contact n^+-GaAs layer (Fig. 1a). As this voltage grows from zero to 20 V, the U_f^* value increases by a factor of 1.9. Upon hydrogenation (Fig. 1b), the dependence of U_f^* on the bias voltage is markedly less pronounced: for the same increase in the bias voltage (20 V), the signal amplitude increases only by a factor of 1.1.

Previously [5], it was demonstrated that suppression of the effect of parasitic feedback via substrate, observed upon hydrogenization of the ion-doped GaAs structures, is due to the hydrogen-induced passivation of the deep centers situated at the phase boundary between active layer and substrate (n–n_i junction) and/or in the semi-insulating substrate. As is known [9], the slow photoconductivity relaxation in these systems is related to recharge of the deep centers situated in the n–n_i junction. We may suggest that a decrease in the contribution of processes responsible for the slow relaxation and, hence, a less pronounced dependence of the amplitude U_f^* on the bias voltage, are due to the passivation of these centers by atomic hydrogen. It is also possible that hydrogenization resulted in a change in the conductivity type of the GaAs substrate (e.g., from ν to π type). Note that the recombination level will be always occupied by holes and not recharged as a result of the injection of minority carriers (holes) from the n-GaAs layer to the n–n_i junction during the photoexcitation. At the same time, the observed behavior can be related to the incorporation of atomic hydrogen into the near-surface layers of GaAs and the formation of new centers [10] capable of facilitating fast recombination of the charge carriers.

We have studied possibilities of the practical implementation of the effect of hydrogenation-induced passivation of electrically active centers in the fabrication of integrations based on the Schottky field-effect transistors. In a comparative experiment, we have studied a semi-insulating GaAs substrate with n^+–n layer, possessing poor initial electrophysical characteristics. One part of the substrate was hydrogenated in a flow of atomic hydrogen, while the other part served a control. A technological scheme used for the fabrication of integrated circuits was the same for the samples of both types.

Figure 2 shows the current–voltage (I–U) characteristics of the test transistors used in the integrations. The test transistors obtained on the hydrogenated part of the substrate exhibit better characteristics (higher saturation currents, greater slope of the I–U characteristics) as compared to those of the control sample. For example, the slope of the I–U curves for transistors on the hydrogenated substrates was $\cong$1.5 times that of the control samples, and the saturation current measured for a drain–source voltage of 3 V in the former structure was $\cong$1.4 times that in the latter (control) case. In addition, the transistors fabricated on the hydrogenated substrate exhibited a lower change in the I–U characteristics upon illumination of the transistor surface. The integrated circuits based on the hydrogenated substrates exhibit a greater slope of the I–U characteristics of the working transistors and higher stability of the system operation at increasing working frequency.

Thus, we have established that hydrogenation of the ion-doped n^+–n–n_i-GaAs structures leads to an increase in the rate of photoconductivity relaxation in the ion-doped layers and a decrease in the effect of reverse bias voltage applied to the n^+-GaAs layer on the photocon-

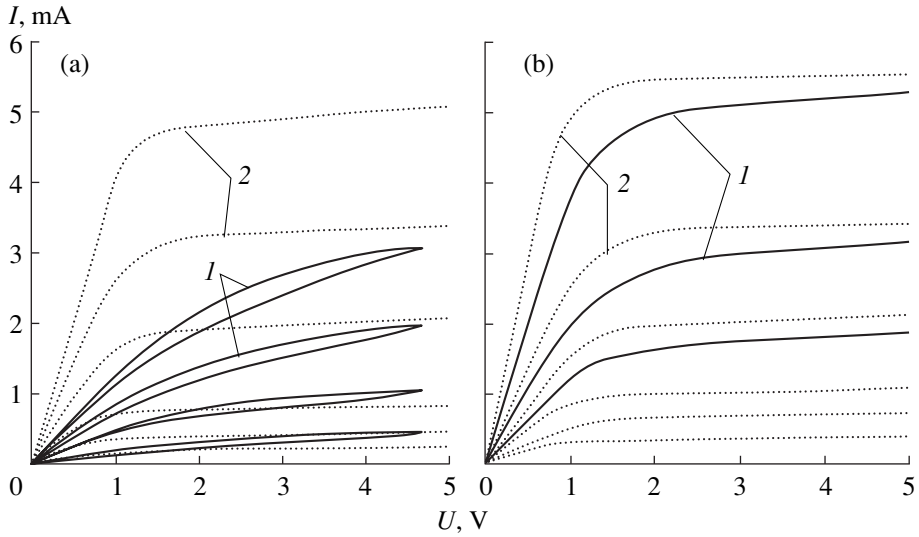

Fig. 2. The current–voltage (*I–U*) characteristics of the test transistors fabricated on the (a) initial and (b) hydrogenated substrate. The measurements were performed (*1*) without and (*2*) with illumination of the transistor structure surface.

ductivity. It was found that hydrogenization has a favorable effect on the parameters of Schottky barrier transistors and the related integrations.

REFERENCES

1. J. Chevallier and M. Aucouturier, Ann. Rev. Mater. Sci. **18**, 219 (1988).
2. J. W. Corbett, S. J. Pearton, and M. Stavola, *Defect Control in Semiconductors*, Ed. by K. Sumino (North-Holland, Amsterdam, 1990), pp. 53–63.
3. S. J. Pearton, W. C. Dautremont-Smith, J. Chevallier, *et al.*, J. Appl. Phys. **59**, 2821 (1986).
4. V. Lagovski, M. Kaminska, J. M. Parsey, *et al.*, Appl. Phys. Lett. **41**, 1078 (1982).
5. V. A. Kagadeĭ, Yu. V. Lilenko, D. I. Proskurovskiĭ, and L. S. Shirokova, Pis'ma Zh. Tekh. Fiz. **25**, 37 (1999) [Tech. Phys. Lett. **25**, 522 (1999)].
6. V. A. Kagadeĭ and D. I. Proskurovsky, J. Vac. Sci. Technol. A **16**, 2556 (1998).
7. V. A. Kagadeĭ, D. I. Proskurovsky, S. D. Reger, and L. M. Romas', Mikroélektronika **27**, 10 (1998).
8. V. Ya. Prinz, RF Patent No. 2006984 (30 January 1994).
9. V. Ya. Prinz, S. N. Rechkunov, and V. A. Smoylov, Inst. Phys. Conf. Ser. **160**, 487 (1997).
10. V. G. Bozhkov, V. A. Kagadeĭ, and N. A. Torkhov, in *Proceedings of the 6th International Conference "Current Problems in Electronics and Instrument Building," Novosibirsk, 1998* (Novosibirsk, 1998), Vol. 2, pp. 206–207.

Translated by P. Pozdeev

Technical Physics Letters, Vol. 26, No. 4, 2000, pp. 272–275. Translated from Pis'ma v Zhurnal Tekhnicheskoĭ Fiziki, Vol. 26, No. 7, 2000, pp. 8–17.

The Spectrum of Dipole-Exchange Spin Waves in Tangentially-Magnetized Metal–Ferroelectric–Ferromagnet–Ferroelectric–Metal Sandwich Structures

V. E. Demidov and B. A. Kalinikos

St. Petersburg State Electrotechnical University, St. Petersburg, Russia

Received November 12, 1999

Abstract—An equation describing the dipole-exchange spin waves in tangentially magnetized metal–ferroelectric–ferromagnet– ferroelectric–metal symmetric planar sandwich structures has been derived within the framework of the Green function tensor formalism for the Maxwell field equations. Changes in the wave spectrum in response to variation of the layer structure parameters are theoretically studied. © *2000 MAIK "Nauka/Interperiodica".*

The determination of the wave spectrum in multilayer structures containing ferromagnetic and ferroelectric layers is a task of considerable practical importance. SHF devices implementing these structures would combine the advantages of electric and magnetic control mechanisms. Of additional interest can be the nonlinear effects caused by the simultaneous manifestation of nonlinearities in the magnetic and electric subsystems of a multilayer structure under consideration.

The interaction between the magnetization waves and the electromagnetic waves in contacting ferromagnetic and ferroelectric layers was studied by Afinogenov *et al.* [1, 2]. In particular [1], a dispersion equation describing the surface magnetostatic waves in a ferroelectric–dielectric–ferromagnetic structure was derived and the spectrum of these waves was studied. The calculation was performed with neglect of the exchange interaction and the effect of electromagnetic wave retardation outside the ferroelectric layer.

The task of determining the spectrum of spin waves in a sandwich structure of the metal–dielectric–ferrite–dielectric–metal type was solved [3] with an allowance for the exchange interaction. However, the solution was obtained in a magnetostatic approximation, which makes the results inapplicable to description of the systems of some other types, in particular, involving ferroelectric and ferromagnetic layers.

The purpose of this work was to study the spectrum of dipole-exchange spin waves in tangentially magnetized symmetric planar sandwich structures of the metal–ferroelectric–ferromagnet–ferroelectric–metal type taking into account the effect of electromagnetic wave retardation.

Let us consider a plane-parallel (planar) multilayer structure unbounded in the *YOZ* plane, comprising an isotropic ferromagnetic layer with a thickness L (characterized by the saturation magnetization M_0 and the permittivity ϵ_L), separated from ideal conducting metal screens on both sides by dielectric films (with a thickness a and permittivity ϵ_a). The origin of the coordinate system coincides with the center of the ferromagnetic layer, so that the whole structure is symmetric with respect to the *YOZ* plane. The ferromagnetic layer is assumed to be magnetized to saturation by a constant homogeneous magnetic field with a strength H_0, oriented along the *Z*-axis. The spins on the magnetic layer boundaries are assumed to be free.

The task of determining the spin wave spectrum in the above planar sandwich structure is solved by jointly integrating the equation of magnetization wave motion and the complete system of Maxwell field equations. This can be performed using a theoretical approach based on the Green functions for the Maxwell field equations, which has been developed previously [3, 4] for description of the dipole-exchange spin waves in ferromagnetic films.

The solution of the boundary problem formulated above leads to an approximate transcendental dispersion equation establishing a relationship between the wave frequency ω and the longitudinal wavenumber k_ζ of the waves propagating at an angle φ to the magnetic field direction. For the nth eigenwave, the equation is as follows:

$$(\Omega_{nk} - \omega_M A_n^{xx})[\Omega_{nk} - \omega_M(A_n^{yy}\cos^2\varphi + A_n^{zz}\sin^2\varphi)] - \omega^2 = 0, \quad (1)$$

where

$$\Omega_{nk} = \omega_H + \omega_M \alpha k_n^2,\ \omega_H = \gamma H_0,\ \omega_M = \gamma M_0,$$

$$\gamma = 2\pi 2.8 \times 10^6\ \text{rad/(s Oe)},\ \alpha = 3 \times 10^{-12}\ \text{cm}^2,$$

1063-7850/00/2604-0272$20.00 © 2000 MAIK "Nauka/Interperiodica"

$$A_n^{xx} = -1 + \frac{k_\zeta^2}{\gamma_L^2 + \kappa_n^2}\left\{1 - \frac{\gamma_L}{\gamma_L^2 + \kappa_n^2} \times \frac{4}{L(1+\delta_{0n})\sinh(\gamma_L(2a+L))N} C_n^1(D_a(-1)^n - T_a)\right\},$$

$$A_n^{yy} = \frac{k_{0L}^2}{\gamma_L^2 + \kappa_n^2}\left\{1 - \frac{\gamma_L}{\gamma_L^2 + \kappa_n^2} \times \frac{4}{L(1+\delta_{0n})\sinh(\gamma_L(2a+L))N^y} \times C_n^2(D_a^y(-1)^n + T_a^y)\frac{\epsilon_L\gamma_a}{\epsilon_a\gamma_L}\tanh(\gamma_a a)\right\},$$

$$A_n^{zz} = -\frac{\gamma_L^2}{\gamma_L^2 + \kappa_n^2}\left\{1 - \frac{\gamma_L}{\gamma_L^2 + \kappa_n^2} \times \frac{4}{L(1+\delta_{0n})\sinh(\gamma_L(2a+L))N} \times C_n^2(D_a(-1)^n + T_a)\frac{\gamma_L}{\gamma_a}\tanh(\gamma_a a)\right\},$$

$$C_n^1 = \cosh(\gamma_L(a+L))(-1)^n - \cosh(\gamma_L a),$$

$$C_n^2 = \sinh(\gamma_L(a+L))(-1)^n - \sinh(\gamma_L a),$$

$$D_a = \sinh(\gamma_L(a+L)) + \frac{\gamma_L}{\gamma_a}\tanh(\gamma_a a)\cosh(\gamma_L(a+L)),$$

$$D_a^y = \sinh(\gamma_L(a+L)) + \frac{\epsilon_L\gamma_a}{\epsilon_a\gamma_L}\tanh(\gamma_a a)\cosh(\gamma_L(a+L)),$$

$$T_a = \sinh(\gamma_L a) - \frac{\gamma_L}{\gamma_a}\tanh(\gamma_a a)\cosh(\gamma_L a),$$

$$T_a^y = \sinh(\gamma_L a) - \frac{\epsilon_L\gamma_a}{\epsilon_a\gamma_L}\tanh(\gamma_a a)\cosh(\gamma_L a),$$

$$N = \sinh(\gamma_L L)\left(1 + \left(\frac{\gamma_L}{\gamma_a}\tanh(\gamma_a a)\right)^2\right) + 2\cosh(\gamma_L L)\frac{\gamma_L}{\gamma_a}\tanh(\gamma_a a),$$

$$N^y = \sinh(\gamma_L L)\left(1 + \left(\frac{\epsilon_L\gamma_a}{\epsilon_a\gamma_L}\tanh(\gamma_a a)\right)^2\right) + 2\cosh(\gamma_L L)\frac{\epsilon_L\gamma_a}{\epsilon_a\gamma_L}\tanh(\gamma_a a),$$

$$\gamma_L^2 = k_\zeta^2 - k_{0L}^2,\ k_{0L}^2 = \omega^2\epsilon_0\mu_0\epsilon_L,$$

$$\gamma_a^2 = k_\zeta^2 - k_{0a}^2,\ k_{0a}^2 = \omega^2\epsilon_0\mu_0\epsilon_a,$$

$$k_n^2 = k_\zeta^2 + \kappa_n^2,\ \kappa_n = \frac{n\pi}{L}.$$

The dispersion equation (1) has to be numerically solved for various values of the sandwich structure parameters. Each set of parameters leads to a family of dispersion curves, among which we may distinguish the curve corresponding to a slow magnetization wave, the curve corresponding to a zero-cutoff electromagnetic wave (lowest mode), and several curves representing electromagnetic waves of higher modes with the cutoff frequencies determined by thicknesses of the ferromagnetic and ferroelectric layers.

Figure 1 shows dispersion curves of the waves propagating in the direction of constant magnetization (longitudinal waves) for three values of the ferroelectric layer thickness. The calculation was performed using the values of parameters typical of the yttrium–iron garnet (YIG): $M_0 = 1750$ G; $L = 20$ μm; $\epsilon_L = 14$. The magnetization field strength was taken equal to $H_0 = 3000$ Oe, and the permittivity of the ferroelectric films was assumed to be $\epsilon_a = 1000$.

For $a = 100$ μm, the cutoff frequencies of the higher electromagnetic wave modes are markedly greater than the characteristic frequencies of spin waves in the system without exchange. In this case, only interaction of the spin waves with the lowest electromagnetic wave modes is significant, which is manifested by "separation" of the corresponding dispersion curves. As a

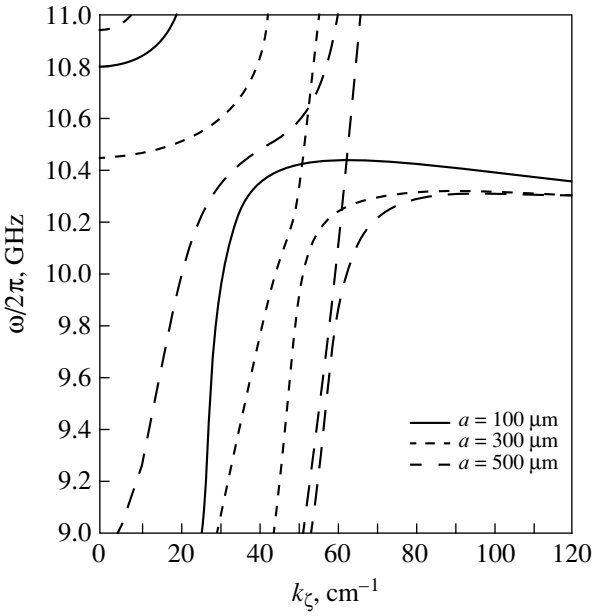

Fig. 1. The spectrum of longitudinal waves in sandwich structures with different thicknesses a of the ferroelectric layers.

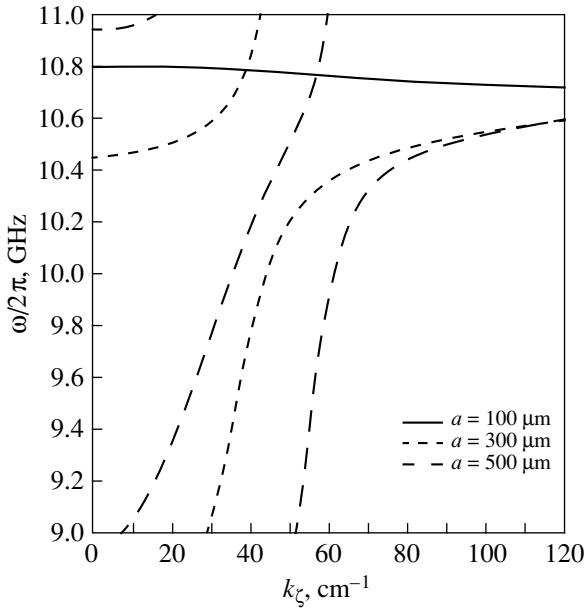

Fig. 2. The spectrum of transverse waves in sandwich structures with different thicknesses a of the ferroelectric layers.

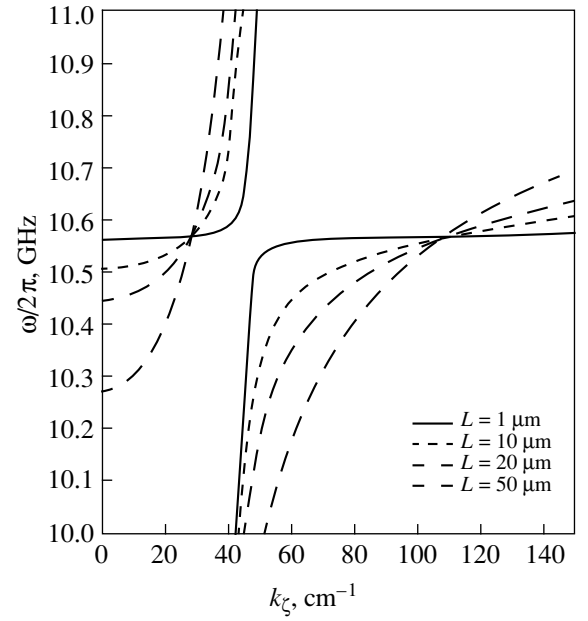

Fig. 3. The spectrum of transverse waves in sandwich structures with different thicknesses L of the ferromagnetic layers.

result, the lowest electromagnetic wave modes acquire a nonzero cutoff, while the frequency of spin waves tends to zero with $k_\zeta \longrightarrow 0$. As the ferroelectric layer thickness increases, the cutoff frequencies of the highest electromagnetic wave modes shift down and the curve of the lowest electromagnetic wave mode (with decreasing cutoff frequency) closely approaches the dispersion curve of the spin waves.

An analysis showed that a change in the direction of wave propagation from longitudinal to transverse, whereby φ varies from 0 to 90°, is accompanied by gradual decrease in the interaction of spin waves with the lowest electromagnetic wave mode. This is manifested by decreasing "gap" between the corresponding dispersion curves, until the separation would completely vanish at φ = 90°. The strictly transverse (from the standpoint of mutual orientation of the wavevector and the magnetization direction) spin waves do not interact with the lowest electromagnetic wave mode and the corresponding dispersion curves intersect. This result is explained by the fact that, in the linear approximation, the only nonzero magnetic field component (h_z) of the lowest electromagnetic wave mode is not related to the variable magnetization components (m_x and m_y) of the transverse spin wave.

Figure 2 presents the dispersion curves (calculated using the same parameters as above) for the transverse spin waves and for the highest electromagnetic wave modes interacting with these spin waves. As seen, the curve for the spin waves in a system with a = 100 μm exhibits no hybridization. The absence of interaction with the lowest electromagnetic wave modes renders properties of the transverse spin waves virtually independent of the parameters of ferroelectric layers at small a values. As the thickness on the ferroelectric layers increases, the cutoff frequencies of the highest electromagnetic wave modes tend to decrease and, hence, the interaction between spin and electromagnetic waves increases as reflected by hybridization of the dispersion characteristics. This leads to the same manifestations as in the case of longitudinal waves.

Figure 3 shows the dispersion curves of the transverse waves calculated for various thicknesses of the ferromagnetic layer. The calculation was performed for M_0 = 1750 G, H_0 = 3000 Oe, ϵ_L = 14, a = 300 μm, and ϵ_a = 1000. By these data, we may follow the variation of the interaction between the first higher electromagnetic wave harmonic and the spin waves in the system with increasing ferromagnetic layer thickness. As seen, the efficiency of this interaction increases with L, as manifested by growing "gap" between the corresponding dispersion curves.

The effect of hybridization of the dispersion curves of spin waves, accompanying variation of the parameters of ferroelectric layers, can be used to control the spectrum of spin waves in the system under consideration. There are two possible variants of such a control. In the longitudinal wave geometry, the dispersion of spin waves at small thicknesses of the ferroelectric layers can be controlled based on a change in the spectrum of the lowest electromagnetic wave mode depending on ϵ_a. However, this mechanism has proved to be ineffective. A much more effective control is that based on the hybridization of the dispersion curves of spin waves and the first highest electromagnetic wave mode.

Figure 4 demonstrates the possibility of controlling the spectrum of transverse spin waves based on variation of the cutoff frequency of the first highest electro-

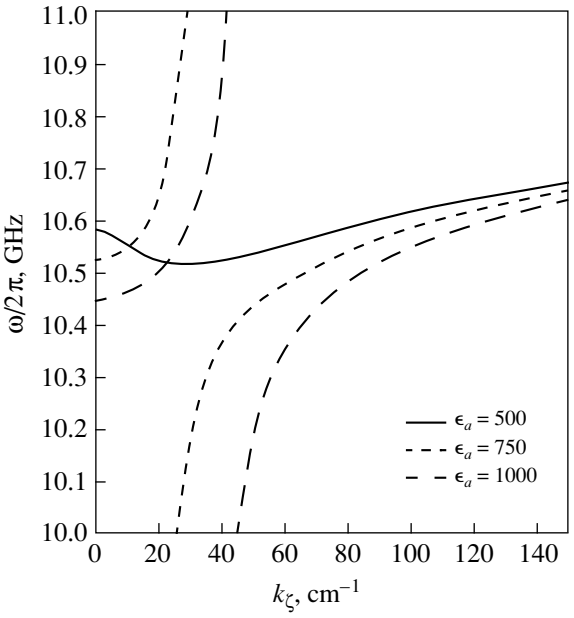

Fig. 4. The spectrum of transverse waves in sandwich structures with different permittivities ϵ_a of the ferroelectric layers.

magnetic wave mode, the latter variation being achieved by changing permittivity of the ferroelectric layers. The dispersion curves were calculated for M_0 = 1750 G, H_0 = 3000 Oe, L = 20 μm, ϵ_L = 14, and a = 300 μm. As the ϵ_a value decreases from 1000 to 500, the dispersion curve of the first highest electromagnetic wave mode shifts toward higher frequencies. This results in decreasing interaction of this electromagnetic wave mode with the spin waves. The dispersion curve of spin waves changes accordingly: the intrinsic frequency of spin waves at k_ζ = 60 cm^{-1} changes by approximately 200 MHz and the group velocity drops several times.

Thus, the above results indicate that the interaction of slow dipole-exchange spin waves with fast electromagnetic waves in tangentially magnetized symmetric planar structures of the metal–ferroelectric–ferromagnet–ferroelectric–metal type leads to separation of the corresponding branches of the dispersion curves. This phenomenon allows the dispersion characteristics of spin waves to be controlled by changing permittivity of the ferroelectric layers. The most effective control is observed in the case when the intrinsic frequency of the first highest electromagnetic wave mode is close to the frequency of spin waves. Using on this principle, it is possible to create electric-field-controlled tunable SHF resonators, filters, delay lines, and phase-shifting devices.

This work was supported by the Russian Foundation of Basic Research (project no. 99-02-16370) and by the Ministry of General Professional Education of the Russian Federation (grant no. 97-8.3-13).

REFERENCES

1. V. B. Anfinogenov, T. N. Verbitskaya, Yu. V. Gulyaev, *et al.*, Radiotekh. Élektron. (Moscow) **34**, 494 (1989).
2. V. B. Anfinogenov, T. N. Verbitskaya, Yu. V. Gulyaev, *et al.*, Radiotekh. Élektron. (Moscow) **35**, 320 (1990).
3. V. F. Dmitriev and B. A. Kalinikos, Izv. Vyssh. Uchebn. Zaved., Fiz. **31**, 24 (1988).
4. B. A. Kalinikos, Izv. Vyssh. Uchebn. Zaved., Fiz. **24**, 42 (1981).

Translated by P. Pozdeev

Technical Physics Letters, Vol. 26, No. 4, 2000, pp. 276–278. Translated from Pis'ma v Zhurnal Tekhnicheskoĭ Fiziki, Vol. 26, No. 7, 2000, pp. 18–23.

Optical Reflection from a Semiinfinite Nonlinear Crystal

K. D. Lyakhomskaya, P. I. Khadzhi, and D. A. Markov

Pridnestrovsk State University, Tiraspol, Moldova

Received November 12, 1999

Abstract—Multistability of the reflection coefficient as a function of incident amplitude is theoretically demonstrated to be possible for a semiinfinite optically homogeneous medium with the Kerr nonlinearity. The multistability arises at certain relations between the system parameters. The treatment is essentially free from the assumption that field envelopes vary slowly in space. Underlying physical processes are described. © *2000 MAIK "Nauka/Interperiodica".*

It is generally agreed that a multistable reflection or transmission function is feature of a plane-parallel plate made of a nonlinear semiconductor, whereas the reflection from a semiinfinite homogeneous absorbing nonlinear medium may have at most two stable states [1–7]. Note that these results were obtained under the assumption that field envelopes vary slowly in space. The multistability in the former system is due to the reflection from the rear face, which produces feedback and nonlinear constructive interference. No such reflection takes place in the latter case for the approximation adopted. We have found that multistability does exist in the semiinfinite medium as well outside the framework of the approximation of slowly varying envelopes. A more general approach reveals the reflection caused by abrupt spatial variations in the nonlinear refractive index under strong excitation conditions. The resultant backward wave constructively interferes with the forward wave to provide for the feedback.

This paper presents the main findings of a theoretical investigation into the nonlinear reflection from a semiinfinite optically homogeneous isotropic semiconductor with the Kerr nonlinearity. The permittivity of the medium is

$$\varepsilon = \varepsilon_1 + i\varepsilon_2 + (-\alpha + i\beta)|E|^2, \qquad (1)$$

where ε_1 and ε_2 are the real and the imaginary part of the permittivity in the zero-field limit and E is the wave amplitude. The complex factor $\alpha + i\beta$ allows for the Kerr effect. In the context of a nonlinear oscillator model for the medium, the coefficients α and β usually obey the following relationships:

$$\alpha = \alpha_0\delta(\delta^2 + 1)^{-1}, \quad \beta = \alpha_0(\delta^2 + 1)^{-1}, \qquad (2)$$

where α_0 is the Kerr constant and $\delta = \Delta/\gamma$ is the normalized detuning parameter; the latter is expressed as $\delta = (\omega - \omega_0)/\gamma$, where ω and ω_0 are the frequency of the incident radiation and that of the quantum transition, respectively, and γ is the attenuation constant. Note that expressions (2) are the same as those derived for the two-photon generation of biexcitons from the ground state of a crystal [8]; as is known, the process features giant oscillator strength.

Let an electromagnetic wave with the electric field amplitude E_i and the frequency ω come from vacuum to the flat surface of the medium. The incident wave partly penetrates into the medium and propagates there. The permittivity of the crystal changes as a result of nonlinear interaction with the wave filed according to (1). A stationary field distribution in the medium can be obtained from the nonlinear wave equation

$$\frac{d^2E}{dz^2} + \frac{\omega^2}{c^2}(\varepsilon_1 + i\varepsilon_2 + (-\alpha + i\beta)|E|^2)E = 0, \qquad (3)$$

where c is the velocity of light in vacuum and z is the coordinate in the direction of propagation. Let the surface be situated at $z = 0$. The boundary conditions are determined by the continuity of the tangential field components:

$$E_i = E_r = E|_{z=0}, \quad E_i - E_r = -i\frac{\partial E}{\partial z}\bigg|_{z=0}, \qquad (4)$$

where E_i and E_r are the amplitudes of the incident and the reflected wave field, respectively [9–12]. The medium being semiinfinite and absorbing implies that a physical solution to equation (3) must obey the condition $E(z) \longrightarrow 0$ for $z \longrightarrow \infty$.

It is convenient to normalize the field amplitudes as follows:

$$F(z) = \frac{E(z)}{\sqrt{\alpha_0}}, \quad F_r = \frac{E_r}{\sqrt{\alpha_0}}, \quad F_i = \frac{E_i}{\sqrt{\alpha_0}}. \qquad (5)$$

Since nonlinear equation (3) cannot be rigorously solved in the analytical form, we resort to a numerical technique. Also note that the numerical integration of (3) cannot start from $z = 0$, because the reflected wave amplitude E_r is unknown [see (4)]. Our approach is as follows. Let the normalized field amplitude be infinitesimal at a certain $z = z_0$ inside the medium,

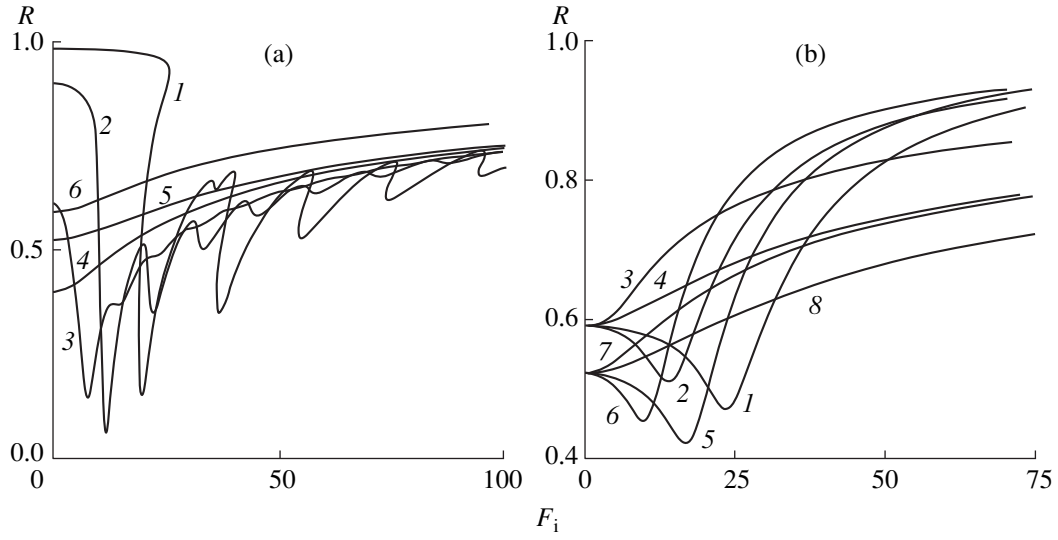

Fig. 1. The plots of reflection coefficient R vs. normalized incident amplitude F_i for different δ, ε_1, and ε_2. For panel a: $\delta = -15$, $\varepsilon_2 = 1.5$, and $\varepsilon_1 =$ (*1*) –17, (*2*) –5, (*3*) –1, (*4*) 5, (*5*) 10, or (*6*) 15. For panel b: $\varepsilon_2 = 1.5$ and δ and ε_1 are (*1*) 15 and 15, (*2*) 5 and 15, (*3*) 0 and 15, (*4*) –5 and 15, (*5*) 15 and 10, (*6*) 5 and 10, (*7*) –15 and 10, or (*8*) –5 and 10, respectively.

which implies that $|F(z)| \ll 1$. Such a point does always exist due to absorption. Then the nonlinear term in (3) vanishes and the solution represents simply a forward wave:

$$F(z) = F(z_0)\exp\left[i\sqrt{\varepsilon_1 + i\varepsilon_2}(z - z_0)\right]. \qquad (6)$$

The integration of (3) starts from $z = z_0$ and moves in the backward direction. According to (4) and (6), the field and its derivative are known at z_0, these values determining the solution of (3) for z varying from z_0 to 0. This gives us spatial distribution of the complex function $F(z)$, and the incident $F_i(z)$ and reflected $F_r(z)$ wave fields.

The figure shows the reflection coefficient $R = |F_r|^2/|F_i|^2$ plotted against the normalized amplitude F_i for different values of the parameters ε_1, ε_2, and δ. Note the multistability arising at $\varepsilon_1 < 0$ and $\delta < 0$. For the other tested values of ε_1 and δ, the reflection coefficient is a single-valued nonlinear function. Let us trace the source of multistability and bistability. At a low incident wave amplitude, the real part of the permittivity is negative so that the reflection is virtually total (no transmitted wave). As the amplitude grows both on the surface and in the medium, the real part decreases in magnitude, vanishes, becomes positive, and increases in magnitude further. The medium thus becomes loss reflective and more transparent. Eventually, sharp peaks arise in the reflection coefficient (see figure). Thus, the medium is rendered optically inhomogeneous at high excitation levels. This inhomogeneity is responsible for the backward wave, which in turn produces the feedback underlying multistability of the reflection coefficient. However, Fig. 1 (panel b) also indicates that the multistability disappears at an excessively high incident wave amplitude. In this case, the peaks of reflection coefficient move deep into the medium so that the reflected wave dies away before it reaches the surface, making constructive interference impossible. Also note (in panel a) that decreasing the magnitude of ε_1 (for $\varepsilon_1 < 0$) gradually suppresses the multistability, the reflection coefficient becoming a single-valued nonlinear function with oscillating behavior.

At $\varepsilon_1 < 0$ and $\delta > 0$, the surface reflection coefficient sharply changes to become essentially a single-valued function, although it remains nonlinear. This is because the real part of the permittivity is negative and grows in magnitude as the incident wave amplitude increases. The field penetrates to a depth less than the light wavelength and creates a thin layer with a large reflection coefficient in the vicinity of the surface. At $\varepsilon_1 > 0$, the surface reflection coefficient is a single-valued nonlinear function (see panel b).

To sum up, we have demonstrated that, with the approximation of slowly varying envelopes, rejected, the reflection coefficient as a function of the incident amplitude may under certain conditions exhibit multistability even in the case of a semiinfinite medium with the Kerr nonlinearity. The multistability stems from the reflection peaks arising in the medium due to the redistribution of the refractive index and the absorption coefficient. A high level of excitation imparts optical inhomogeneity to an originally homogeneous nonlinear medium, so that feedback is created.

REFERENCES

1. H. M. Gibbs, *Optical Bistability: Controlling Light with Light* (Academic Press, New York, 1985; Mir, Moscow, 1988).

2. P. I. Khadzhi, G. D. Shibarshina, and A. Kh. Potaru, *Optical Bistability in a System of Coherent Excitons and Biexcitons in Semiconductors* (Shtiintsa, Kishinev, 1988).
3. D. A. B. Miller, IEEE J. Quantum Electron. **17**, 306 (1981).
4. W. Chen and D. L. Mills, Phys. Rev. B **35**, 524 (1987).
5. A. E. Kaplan, Pis'ma Zh. Éksp. Teor. Fiz. **24**, 132 (1976) [JETP Lett. **24**, 114 (1976)]; A. E. Kaplan, Zh. Éksp. Teor. Fiz. **72**, 1710 (1977) [Sov. Phys. JETP **45**, 896 (1977)].
6. V. S. Butylkin, A. E. Kaplan, Yu. G. Khronopulo, and E. I. Yakubovich, *Resonance Interactions Between Light and Matter* (Nauka, Moscow, 1977).
7. B. B. Boĭko and N. S. Petrov, *Reflection of Light from Amplifying and Nonlinear Media* (Nauka i Tekhnika, Minsk, 1988).
8. P. I. Khadzhi, in *Nonlinear Optical Processes in Systems of Excitons and Biexcitons in Semiconductors* (Shtiintsa, Kishinev, 1985).
9. L. Roso-Franco, Phys. Rev. Lett. **55**, 2149 (1985); J. Opt. Soc. Am. B **4**, 1878 (1987).
10. V. Malyshev and E. C. Jarque, J. Opt. Soc. Am. B **12**, 1868 (1995).
11. V. A. Malyshev and E. C. Jarque, Opt. Spektrosk. **82**, 630 (1997) [Opt. Spectrosc. **82**, 582 (1997)].
12. E. C. Jarque and V. Malyshev, Opt. Commun. **142**, 66 (1997).

Translated by A. A. Sharshakov

Technical Physics Letters, Vol. 26, No. 4, 2000, pp. 279–281. Translated from Pis'ma v Zhurnal Tekhnicheskoĭ Fiziki, Vol. 26, No. 7, 2000, pp. 24–30.

The Effect of Optical Attenuation of Laser Radiation in a Fullerene-Containing COANP–Polyimide System

N. V. Kamanina[1], L. N. Kaporskiĭ[1], Alex Leyderman[2], and Alfonso Barrientos[2]

[1] *Unitary Enterprise at the Vavilov State Optical Institute, All-Russia Scientific Center, St. Petersburg, 190164 Russia*

[2] *Department of Physics, UPR-RUM, Mayagüez, Puerto-Rico, 00680- 9016 USA*

Received November 17, 1999

Abstract—The optical attenuation of laser radiation was studied in a 2-cyclooctylamino-5-nitropyridine–polyimide (COANP–PI) system with C_{70} fullerene additives, which is a promising nonlinear optical medium. The experiments were performed using the second-harmonic radiation of a pulsed neodymium laser. Data on the optical attenuation effect observed in the samples with different fullerene content are presented and analyzed proceeding from a qualitative model based on the possible complex formation in the system studied. © *2000 MAIK "Nauka/Interperiodica".*

Experimental investigations of the optical attenuation of laser radiation in fullerene-containing materials open way to using these media in laser shutters capable of protecting the eyes and sensors from intensive radiation. On the other hand, these experiments provide important information concerning the fundamental properties of nonlinear optical media [1–3]. The shutters implementing fullerenes are capable of functioning in a broad range of laser radiation intensities; the threshold intensity characterizing the optical attenuator is determined by the content of fullerene additive, rather than by the type of fullerene-based sensitizer.

Organic polymers with intramolecular donor–acceptor complexes offer convenient matrices for the introduction of fullerene-based sensitizers. Fullerenes possess greater electron affinity as compared to that of the acceptor fragments of many polymer molecules and are capable of forming complexes with charge transfer, which have an absorption cross-section exceeding that of the donor–acceptor complexes of the polymer matrix. The introduction of fullerenes may lead to the luminescence quenching, favor an increase in the photoconductivity, facilitate manifestations of the reverse absorption saturation of a nonlinear medium, and give rise to the shape memory effect. For example, Kost *et al.* [4] studied the effect of optical attenuation in a system of poly(methyl methacrylate)–C_{60}. Hosoda *et al.* [5] reported data on the spectral features of a polysilane–C_{60} structure and considered a mechanism of photoconductivity increase in this system. Belousov *et al.* [6] experimentally observed a four-wave mixing in orthoxylene–C_{60} samples. Ouyang *et al.* [7] synthesized a new complex based on a thin-film bicyanovinylpyridine–C_{60} composition and demonstrated manifestations of the bistability effect in this system.

Previously [8, 9], we have performed first experiments on the reverse absorption saturation (and, hence, the optical attenuation) in a system of photosensitive polyimide–6b-fullerene. The absorption cross-section of a new complex calculated for an analogous structure [10] has proved to be higher by several orders of magnitude than the value for the polymer matrix employed. Bruening and Fridman [11] proposed a theoretical model describing the mechanism of a photoinduced charge-transfer complex formation in the π-conjugated polymer systems with fullerenes and estimated the time of electron transfer to a C_{60} fullerene molecule.

Below, we report and analyze the first experimental data on the optical attenuation of laser radiation in thin films of 2-cyclooctylamino-5-nitropyridine–polyimide (COANP–PI) with C_{70} fullerene additives.

The nonlinear optical properties of the COANP structure were studied in [12–15]. An interest in this system is explained by its high electrooptical coefficients, small optical response time, and the presence of weakly bound π-electrons (which provides for the ability of readily modifying the properties of COANP molecules). An adequate general formula of this system was obtained in [14]. Based on these data, we performed the experiments with 2.5 and 5% COANP solutions in tetrachloroethane. The concentration of C_{70} fullerene was varied from 0.1 to 5 wt %. A nonphotosensitive polyimide of grade 81A (PI-81A) was used as the plasticizer component. The final composition was applied by a centrifuging technique onto glass substrates carrying preliminarily deposited indium–tin oxide (ITO) conducting layers, which allowed the samples to be used for the photoconductivity measurements. The total sample film thickness was 1–10 μm.

The optical attenuation of laser radiation in the fullerene-containing medium described above was

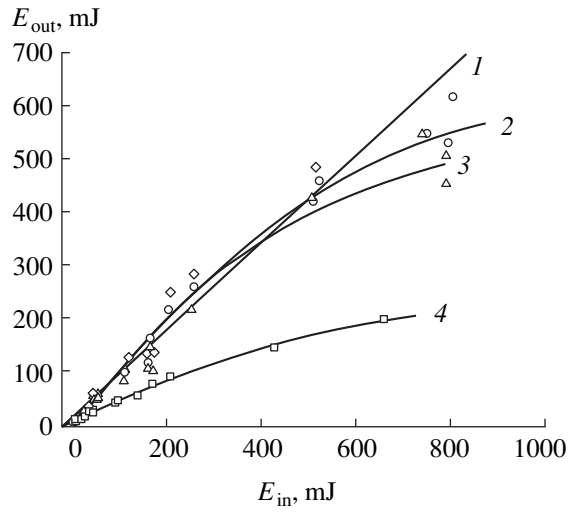

Fig. 1. The plots of output radiation energy (E_{out}) versus the input energy (E_{in}): (*1*) COANP–PI-81A system without fullerene additive; (*2*, *3*) COANP–PI-81A (1 : 1) system with 0.5 and 5 wt % of C_{70} fullerene, respectively; (*4*) COANP–PI-81A (2 : 1) system with 5 wt % of C_{70}.

studied using a single-pass scheme [3] implemented in an experimental setup described elsewhere [9]. The radiation source was based on a pulsed Nd:YAG laser with a pulse duration of 15 ns. The wavelength of the incident radiation upon the second-harmonic conversion was 532 nm. The laser spot diameter on a sample was 3 mm. We have measured the energy incident on a system studied and that transmitted through the sample. The incident radiation energy was varied with the aid of calibrated light filters. The input and output signals were determined directly by using the laser radiation energy meters.

Figure 1 shows the plots of output radiation energy (E_{out}) versus the input energy (E_{in}) for four samples. Sample *1* represents a COANP–PI-81A system without fullerene additive; samples *2* and *3* correspond to the same structure containing 0.5 and 5 wt % of C_{70} fullerene, respectively, with a 1 : 1 ratio of the photosensitive (COANP) and the plasticizer (PI-81A) components; finally, sample *4* refers to a system analogous to *3* but with a different (2 : 1) COANP to plasticizer ratio. As seen from these data, all the fullerene-containing systems studied exhibit the absorption saturation beginning with an input energy level of $E_{in} \sim 600$–700 mJ. This corresponds to an incident energy density of ~8.5–10 J/cm^2, which is a sufficiently high optical attenuation level that allows the materials studied to be applied in attenuators of intense laser beams.

It should be noted that the phenomenon of optical attenuation in fullerene-containing systems is based on the fact that a fullerene molecule absorbing a light quantum with $\lambda = 532$ nm passes to a triplet state, in which the absorption cross-section is several times the value for the nonexcited molecule [1]. The absorption increases with the incident laser radiation intensity because of the growing population of the excited states. Since the laser pulse duration in out experiments ($\tau_p \sim$ 15 ns) is greater than the time of singlet–triplet interaction ($\tau_p > \tau_{S1 \to T1}$) ~1.2 ns [3]), we may conclude that the excited states are accumulated in the form of triplet molecules. The mechanism of optical attenuation of the laser radiation operates via the $T_1 \longrightarrow T_n$ channel. A difference in absorption between samples *2* and *3* is determined by the increased content of fullerene molecules in the latter composition. Note that the attenuation coefficient of sample *4* (Fig. 1) is two times that of sample *3*, although the concentration of fullerene in the two samples is the same.

Thus, the curve shape depends both on the content of the optically-active component (fullerene) in the system and on the possibility of complex formation between a donor fragment of the COANP molecule and fullerene. It should be recalled that the electron affinity of fullerene (2.65 eV [1]) is markedly higher compared to that of the acceptor fragments of most organic molecules. In particular, the acceptor fragment of COANP is an NO_2 molecule bound to the donor fragment via a benzene ring. For a separate NO_2 molecule or radical, the electron affinity is 2.3 eV. However, in a compound with benzene ring, the electron affinity of the NO_2 group decreases to 0.54 eV [16] and becomes smaller than 1/4 of the value for fullerene. In addition, it is known [17] that organic molecules with the donor and acceptor fragments absorbing near $\lambda < 360$ and $\lambda <$ 320 nm, respectively, exhibit a characteristic absorption in the region of $\lambda > 400$ nm (frequently, the absorption is shifted toward the near-IR range). Therefore, the appearance of absorption peaks in the IR spectral range may be evidence of the possible complex formation in the system. In order to check for this possibility, we have studied the absorption spectrum of a COANP–PI-81A system with fullerene additive.

Figure 2 shows the absorption spectrum of the system studied (curve *1*) in comparison with the spectra of pure plasticizer (curve *2*), plasticizer with C_{70} fullerene (curve *3*), and plasticizer with COANP (curve *4*). The appearance of a rather broad absorption band (with a maximum at ~810 nm) in the near-IR range does not contradict the assumption of the charge-transfer complex formation between COANP and C_{70}. Moreover, we have observed a change in the film color from light-yellow (for pure COANP) to light–brown (COANP with fullerene) and a tenfold increase in the light sensitivity of the fullerene-containing system. The photosensitivity measurements were performed using a method described in [18] with application of an electric field with a strength of 60 V/μm. Therefore, taking into account that the role of fullerenes as sensitizers for organic molecules is commonly accepted and the above data indicate the possible complex formation in the π-conjugated system studied, we may conclude that the process of complexation may affect the efficiency of

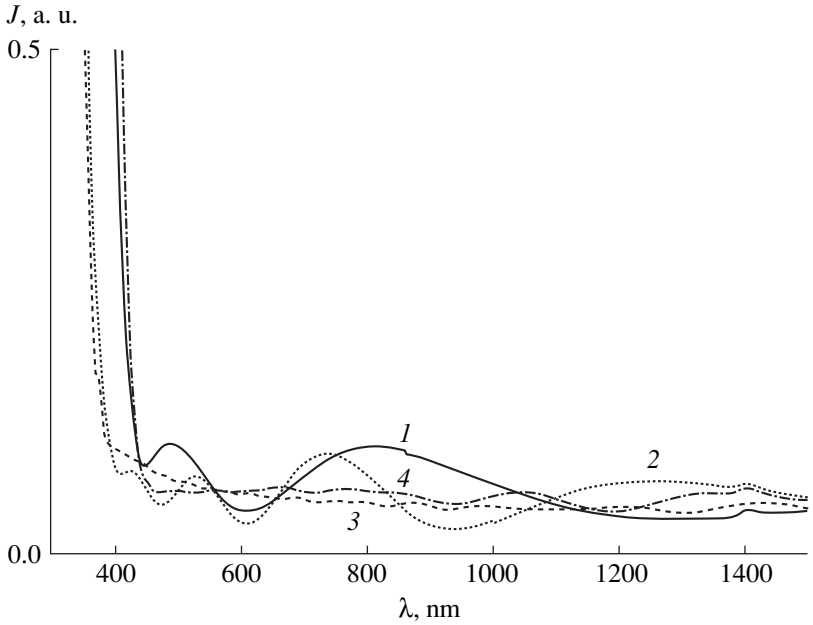

Fig. 2. Optical absorption spectra: (*1*) COANP–PI-81A system with C_{70} fullerene additive; (*2*) pure polyimide 81A; (*3*) polyimide 81A with C_{70} fullerene; (*4*) polyimide 81A with COANP.

optical attenuation of the laser radiation in agreement with the experiment.

Thus, we have experimentally studied the phenomenon of optical attenuation of laser radiation in a fullerene-containing COANP–polyimide system. The levels of incident energy density and attenuation coefficients were determined, the absorption spectrum of the new structure was measured, and evidence was obtained for the formation of charge-transfer complex between COANP molecule and fullerene in the system studied.

The authors are grateful to N.A. Vasilenko and B.V. Kotov (Karpov institute of Physical Chemistry, Moscow) and E.L. Aleksandrova (Vavilov State Optical Institute, St. Petersburg) for their help in work.

This work was partly supported by the Federal Program “Optoelectronic and Laser Technologies.”

REFERENCES

1. A. V. Eletskiĭ and B. M. Smirnov, Usp. Fiz. Nauk **165**, 977 (1995) [Phys. Usp. **165**, 935 (1995)].
2. S. Couris, E. Koudoumas, A. A. Ruth, and S. Leach, J. Phys. B **28**, 4537 (1995).
3. V. P. Belousov, I. M. Belousova, V. P. Budtov, *et al.*, Opt. Zh. **64**, 3 (1997).
4. A. Kost, L. Tutt, M. B. Klein, *et al.*, Opt. Lett. **18**, 334 (1993).
5. K. Hosoda, K. Tada, M. Ishikawa, and K. Yoshino, Jpn. J. Appl. Phys., Part 2 **36** (3B), L372 (1997).
6. V. P. Belousov, I. M. Belousova, V. G. Bespalov, *et al.*, Opt. Zh. **64**, 82 (1997).
7. M. Ouyang, K. Z. Wang, H. X. Zhang, and Z. Q. Xue, Appl. Phys. Lett. **68**, 2441 (1996).
8. N. V. Kamanina, L. N. Kaporskiĭ, and B. V. Kotov, Opt. Comm. **152**, 280 (1998).
9. N. V. Kamanina, Opt. Comm. **162**, 228 (1999).
10. Y. A. Cherkasov, N. V. Kamanina, E. L. Alexandrova, *et al.*, Proc. SPIE **3471**, 254 (1998).
11. J. Bruening and B. Fridman, J. Chem. Phys. **106**, 9634 (1997).
12. J. Hulliger, B. Brezina, and M. Ehrensperger, J. Cryst. Growth. **106**, 605 (1990).
13. Ch. Bosshard, K. Sutter, and P. Günter, J. Opt. Soc. Am. B **6**, 721 (1989).
14. M. Eich, H. Looser, Y. Yoon Do, *et al.*, J. Opt. Soc. Am. B **6**, 1590 (1989).
15. A. Leyderman and Y. Cui, Opt. Lett. **23**, 909 (1998).
16. L. V. Gurvich, G. V. Karachevtsev, V. N. Kondrat’ev, *et al.*, *Energies of Chemical Bond Breakage, Ionization Potentials, and Electron Affinity* (Nauka, Moscow, 1974), p. 351.
17. A. V. Vannikov and A. D. Grishina, *Photochemistry of Polymer Donor–Acceptor Complexes* (Nauka, Moscow, 1984).
18. I. A. Akimov, Yu. A. Cherkasov, and M. I. Cherkashin, *Sensitized Photoeffect* (Nauka, Moscow, 1980).

Translated by P. Pozdeev

Technical Physics Letters, Vol. 26, No. 4, 2000, pp. 282–283. Translated from Pis'ma v Zhurnal Tekhnicheskoĭ Fiziki, Vol. 26, No. 7, 2000, pp. 31–34.

Zinc Oxide Molecules and Clusters Formed in a Quasiclosed Volume of Reactive Gas-Discharge Plasma

E. I. Burylin, A. A. Veselov, A. G. Veselov, A. S. Dzhumaliev, S. N. Ivanov, and O. A. Kiryasova

Saratov Department, Institute of Radio Engineering and Electronics, Russian Academy of Sciences, Saratov, Russia

Received August 3, 1999

Abstract—Plasma-deposited zinc oxide films were studied and it was established that oxide molecules may form and their clusters nucleate within a recombination burning zone in the volume of plasma, provided that the ion range does not exceed the size of a discharge chamber. The nucleation zone is rather narrow and its position depends on the gas pressure in the chamber. The zinc oxide films grown in this zone possess a texture with small misorientation angle and are characterized by small thickness of the nucleation texture and high piezoelectric activity. © *2000 MAIK "Nauka/Interperiodica".*

Solving the task of growing zinc oxide films possessing high piezoelectric activity and small thickness of the nucleation texture requires detailed investigation of the effect of radiation and other external factors on the nucleation process.

Danilin and Syrchin [1] described fabrication of the piezoactive zinc oxide films in a classical planar magnetron sputtering system [1] with the substrates conventionally placed outside the region of plasma burning. During the process, the substrate is maintained at a high temperature [2] in order to thermally activate nucleation in the deposit.

However, films grown by this method possess low piezoelectric activity and exhibit a texture with large misorientation angle. This is explained by the formation of stable condensed phase islands in the initial growth stage, in which the optical axes may have different (sometimes, even opposite) orientations. It is not unless the deposit thickness reaches certain critical value (about a few tenths of micron) that a piezoactive film would form. These films are characterized by considerable nucleation texture and cannot be used for the generation of hypersonic oscillations with frequencies above 10 GHz.

The purpose of this work was to study the surface ion recombination as a factor affecting the electrophysical parameters of zinc oxide films, with a view to obtaining the films featuring small thickness of the nucleation texture and possessing high piezoelectric activity.

The experiments were conducted in a classical planar magnetron sputtering system with an argon–oxygen atmosphere. The gas pressure was effectively controlled within a quasiclosed volume of a quartz cylinder with a radius of 60 mm and a height of 15 mm.

The target represented a disk of chemically pure zinc soldered (to provide for effective cooling) to the central part of a magnetic guide system. The magnetic system configuration and the electric field strength were selected so as to obtain the negative glow region (i.e., the plasma burning zone) having a torch shape such as depicted in the figure. In order to determine the region of formation of zinc oxide molecules, several polished quartz substrates (of sufficiently small diameter, 4–5 mm) were mounted at various distances from the target. The substrates were arranged at different heights and shifted in the radial direction so that not to shadow each other (see the figure).

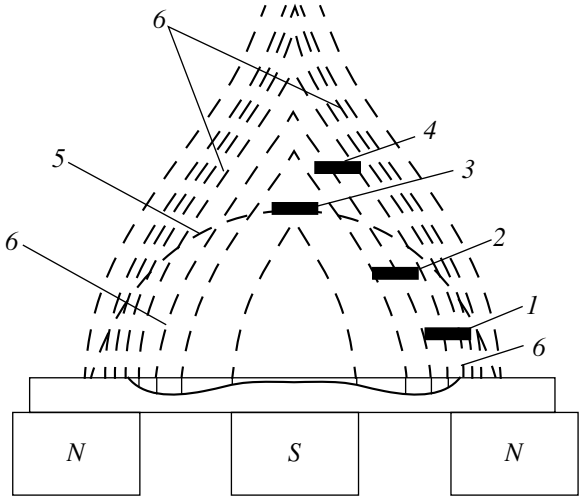

Schematic diagram of the experimental geometry: (*1–4*) substrates; (*5*) boundary of the nucleation zone; (*6*) plasma burning zone (extends from the region of maximum cathode potential drop and is bounded by the zero line of the normal magnetic field component).

1063-7850/00/2604-0282$20.00 © 2000 MAIK "Nauka/Interperiodica"

The main technological regime was characterized by standard parameters: gas mixture composition, 70% oxygen + 30% argon; substrate temperature, 400°C; discharge current, 100 mA; discharge voltage, 600 V. The gas pressure, determining the mean ion free path length (ion range), was varied within a broad range (from 10^{-1} to 10^{-4} Torr). At a minimum possible pressure of 10^{-4} Torr, all substrates were coated with pure zinc because the ion range exceeded linear dimensions of the quasiclosed reactor volume. As the pressure was increased, the upper substrates were coated with zinc oxide (i.e., remained transparent), while the lower substrates were still coated with metal zinc.

The results of numerous experiments showed that the nucleation zone of zinc oxide molecules is 2–3 mm thick and spaced from the erosion zone by a distance equal to the ion range. On the passage across the nucleation zone, the film resistance changes from a value corresponding to the pure metal to that typical of an insulator. In the pressure range studied, the nucleation (condensation) boundary occurred within the quasiclosed volume. The films grown on the substrates placed exactly on the boundary of the nucleation zone exhibited stoichiometric composition. The films deposited on the substrates situated above this zone contained excess oxygen (and, accordingly, possessed greater resistivity), while the films obtained below this level contained excess zinc. Both these compositions deviated from stoichiometry.

It is important to note that films grown on the substrates in position *3* (see the figure), occurring in the zone of (conventionally speaking) "moderate" plasma burning (with the near-cathode potential drop against this position not exceeding 20–30 V), exhibited high piezoelectric activity. These films, at a thickness of 0.18 μm, were capable of effectively generating hypersonic oscillations in an yttrium–aluminum garnet (YAG) crystal at frequencies up to 18 GHz.

In the conventional magnetron systems, the glow zone occurs at a considerable distance from substrates and the nucleation process is activated by the substrate temperature. Should the substrates be placed within the zone of "intensive" plasma burning (corresponding to a near-cathode potential drop exceeding 100 V), the films will acquire a distorted growth texture ("turbidity" zone). In our case, such a zone was also observed in the upper region of the torch.

The fact that zinc oxide molecules are nucleated in the zone of recombination plasma burning was confirmed in another experiment. If the gas pressure in the chamber is sufficiently high (i.e., the ion range is small), the nucleated molecules would "grow up" so as to form clusters. The clusters, sticking to the anode or the walls of the quasiclosed volume, may grow to reach macroscopic dimensions and acquire a hexagonal shape repeating that of the zinc oxide unit cell. As the weight of such a macroscopic cluster reaches certain level, the particle (a few millimeters in size) breaks off from the surface and falls onto the target. This process, which is readily realized under the conditions described above, may probably serve a base for the obtaining of macroscopic clusters of various materials for microelectronics (reactive gas discharge plasma synthesis).

Thus, we have experimentally demonstrated that recombination (or kinetic) energy of ions in the region of plasma burning is not necessarily a detrimental factor in the synthesis of textured films. Under certain conditions (the concentrations of recombining ions), now only experimentally determined, these energies may favor activation of the nucleation of molecules and clusters on the substrate surface and/or in the volume of plasma.

REFERENCES

1. B. S. Danilin and V. K. Syrchin, *Magnetron Sputtering Systems* (Radio i Svyaz', Moscow, 1982).
2. *Handbook of Thin-Film Technology*, Ed. by L. I. Maissel and R. Glang (McGraw-Hill, New York, 1970; Sov. Radio, Moscow, 1977), Vol. 2.

Translated by P. Pozdeev

Technical Physics Letters, Vol. 26, No. 4, 2000, pp. 284–287. Translated from Pis'ma v Zhurnal Tekhnicheskoĭ Fiziki, Vol. 26, No. 7, 2000, pp. 35–42.

Hydrogen Microdoping of the Near-Surface Layers of Gallium Arsenide

V. V. Anisimov[1)], V. P. Demkin[1)], I. A. Kvint[2)], S. V. Mel'nichuk[2)], and B. S. Semukhin[2)]

[1)] *Tomsk State University, Tomsk, 634050 Russia*

[2)] *Institute of Strength Physics and Materials Science, Siberian Division, Russian Academy of Sciences, Tomsk, 634055 Russia*

Received November 16, 1999

Abstract—A method of the semiconductor surface microdoping with hydrogen ions in a plasma–beam discharge is proposed. The results of experiments with GaAs showed the new method to be comparable in efficiency with the conventional methods of surface modification by ion beams. *© 2000 MAIK "Nauka/Interperiodica".*

The ion microdoping of the near-surface layer of semiconductors is used for the obtaining of materials with microcomposite structures possessing new properties.

The low-temperature ion doping of the near-surface layer of a semiconductor material leads to the low-temperature binding of these ions in the saturated surface region and is accompanied by migration of a considerable number of ions deep into the bulk [1]. Various elements have been used for the surface doping, hydrogen ions (H^+) being among the most widely used dopants. There are several methods for incorporating hydrogen into the near-surface layer of semiconductors, including hydrogenation, implantation, and microdoping (protonation) [2].

The microdoping is most frequently performed using high-power ion beams [2]. However, this method of surface processing is rather expensive and labor-consuming. Moreover, the ion-beam surface modification fails to give satisfactory results in case of high purity requirements (high vacuum, absence of impurities, etc.).

We propose a new method of microdoping based on the plasma treatment of a material surface. Plasma is a source of ions formed as a result of plasmachemical processes. The most convenient plasma source for our purposes is offered by plasmachemical reactors [3] using high-voltage electric discharge.

As is well known, the plasma generated by a high-voltage pulsed discharge is characterized by the presence of fast electrons with energies close to eU_0, where U_0 is the amplitude of the voltage applied to electrodes [4]. Thus, using a narrow discharge gap with a grid anode, we may obtain a beam of fast electrons capable of creating an ion flux of considerable density.

We have used a He–H_2 gas mixture as a working medium in the plasmachemical reactor. Helium, playing the role of a buffer gas, provided high energetics of the electron beam, rendering it capable of producing H^+ ions traveling over macroscopic distances (of the order of a few centimeters) from anode [5]. Protons interacting with the target surface are capable, provided that their concentration is sufficiently high, of effectively saturating near-surface layers of the target material. In order to create a sufficiently high proton concentration at the target surface, one has to select proper discharge parameters and the working He–H_2 mixture composition (component ratio).

The purpose of this work was to evaluate parameters of the high-voltage plasma–beam discharge by spectroscopic methods and determine the range of conditions necessary to provide for the optimum saturation of the near-surface layer of a semiconductor material (GaAs).

The optimum ratio of He and H_2 in the working gas mixture was selected so as to obtain a maximum intensity of lines corresponding to emission from highly-excited states of He ions and H atoms. The results of our experiments showed that optimum discharge conditions for a He–H_2 mixture with a component ratio of 8 : 1 and a total pressure of P = 9 Torr are as follows: voltage pulse amplitude U_0 = 2 kV (at a discharge gap width of d = 0.9 mm), pulse duration τ = 2 μs; pulse repetition frequency f = 2.5 kHz.

The concentration of hydrogen ions was estimated using the results of spectroscopic measurements of the intensity of He and He^+ emission lines at various distances from the grid anode. These data were compared to the results of calculation of the electron beam degradation spectra in the He–H_2 plasma [6]. It was found that a hydrogen ion concentration in the plasma column under the given discharge conditions is 10^{13}–10^{14} cm^{-3}, which provides for an H^+ ion flux density of 10^{17}–10^{18} cm^{-2} s^{-1} on the target surface.

1063-7850/00/2604-0284$20.00 © 2000 MAIK "Nauka/Interperiodica"

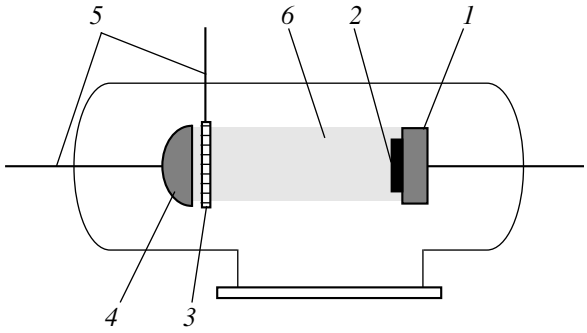

Fig. 1. Schematic diagram of a gas-discharge tube used in the protonation experiments: (*1*) table; (*2*) sample; (*3*) grid anode; (*4*) cathode; (*5*) electrodes; (*6*) plasma column.

For an experiment on the protonation of GaAs (Fig. 1), sample *2* was mounted on table *1* and placed into a gas-discharge tube at a distance of 15 mm from grid anode *3*. The GaAs samples were treated with hydrogen ions by exposure to the discharge plasma for Δt = 1, 2, or 7 min.

The surface of plasma-treated GaAs samples was examined in an optical microscope and the sample structure was studied by X-ray diffractometry.

Figure 2 shows photographs of the surface of GaAs samples (a) before the treatment and after the plasma treatment for (b) 1 min, (c) 2 min, and (d) 7 min (magnification, ×1000). As seen from Fig. 2b, there are almost no changes in the optical image contrast upon the 1-min plasma treatment. The protonation for 2 or 7 min (Figs. 2c and 2d) leads to the formation of blocks uniformly distributed over the samples surface. The dimensions of block formed in the two regimes are different, not exceeding 5 μm for the 2-min plasma treatment and reaching 20 μm for the 7-min exposure. Figure 2e shows a photograph of the edge face (section) of a plasma-treated GaAs sample. It was established that

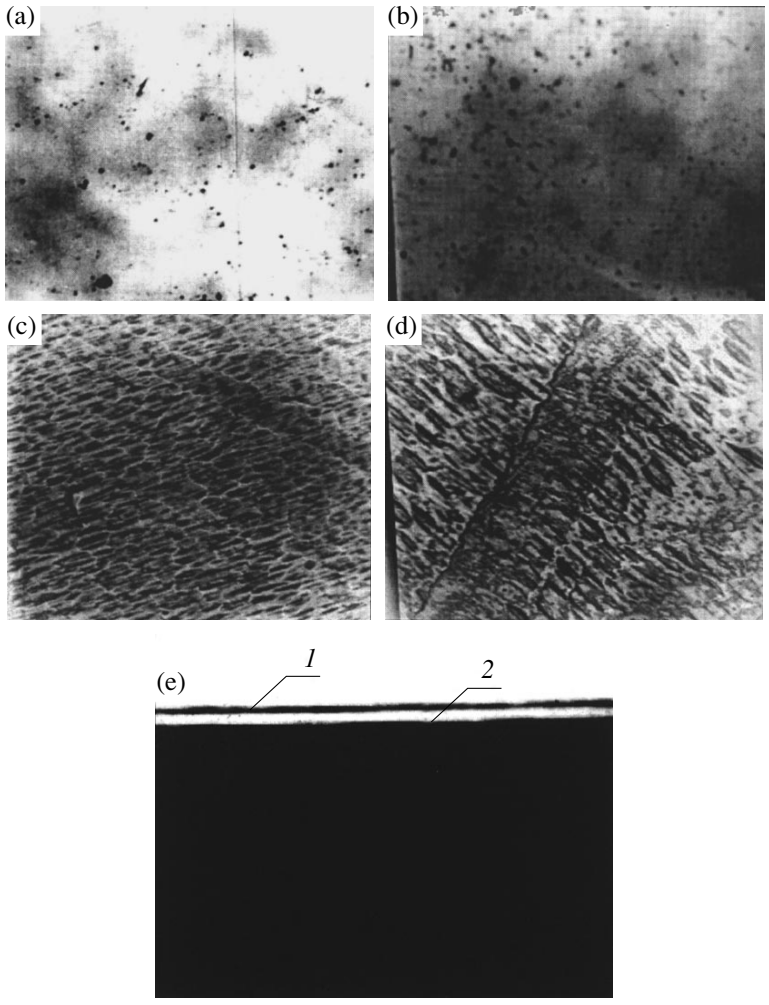

Fig. 2. Photographs of the surface of (a) initial (untreated) and (b–d) protonated GaAs sample surface exposed to plasma for Δt = 1 (b), 2 (c), or 7 min (d); photograph (e) presents the side view (negative) of a plasma-treated sample showing (*1*) the layer of blocks formed as a result of protonation on the surface of (*2*) GaAs matrix (magnification, ×1000).

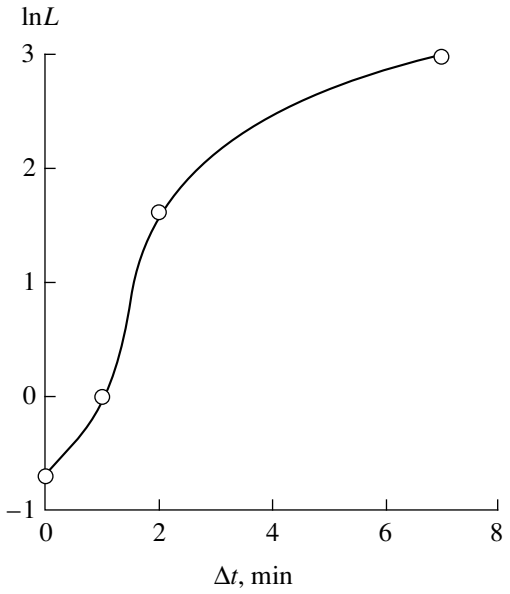

Fig. 3. Plots of the block size (ln*L*) versus exposure time (Δ*t*) for the plasma treated (100)GaAs surface.

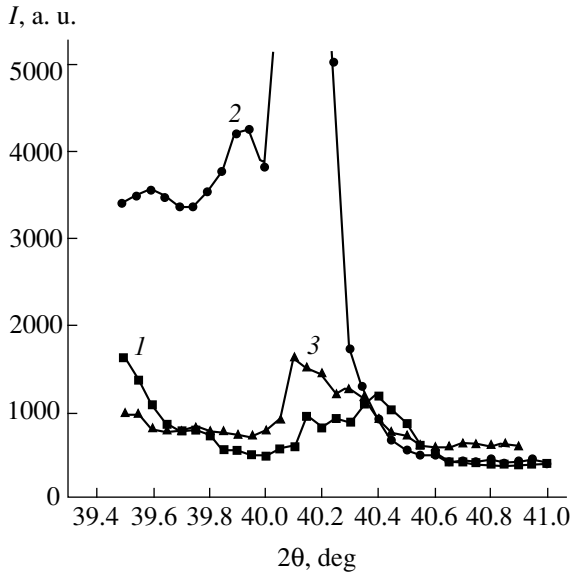

Fig. 4. The rocking curves representing the (200) reflection intensity *I* versus the Bragg angle 2Θ for the X-ray diffraction from GaAs samples (*1*) in the initial state and upon the plasma treatment for (*2*) 2 min and (*3*) 7 min.

the uppermost layer (1) containing the protonation-induced blocks has a thickness of 6 μm and is separated from the substrate matrix (2) by a sharp invariant boundary. Figure 3 shows a plot of the block size *L* versus the exposure time *t*. As is seen, the curve approaches an equilibrium level already after a 2-min plasma treatment of the GaAs sample.

Figure 4 presents fragments of an X-ray diffraction pattern [integral intensity *I* of the (200) reflection versus the Bragg angle 2Θ] for a GaAs sample exposed to the plasma for various times. As is seen, the integral intensity of the (200) reflection increases 4–5 times upon the 2-min exposure. Note that both the initial reflection and that observed upon the 7-min treatment exhibit a complex structure, while the peak observed after the 2-min exposure exhibits a smooth shape well described by the Gauss function. These data indicate that crystal structure of the surface layer (10–15-μm-thick) upon the 2-min plasma treatment is a more perfect compared to that in the nonprotonated state, although the initial sample surface represented a polished (100) single crystal face.

Size of the coherent scattering domains in the initial and protonated GaAs samples

Sample	*D*, Å
Initial	344
	420
	631
Protonated (2 min)	420
Protonated (7 min)	344
	473

The observed redistribution of the reflection intensity may indicate that a series of blocks with different size, representing the coherent scattering domains, are formed the protonated samples. The results of determination of the size of these domains using the well-known Warren method [7] are presented in the table. As seen, the 2-min treatment leads to the development of domains with dimensions of the order of 400 Å, while the 7-min exposure reduces the domain size to 250 and 340 Å rendering the sample structure more homogeneous and closer to ideal.

Thus, the results of our investigations show that the plasma-induced modification of the material reduces to the formation of a near-surface layer with homogeneous block structure on various levels.

In order to prove the role of hydrogen ions in the modification process studied, we have performed similar experiments using pure He and H_2 as the working media. The results of microscopic investigations showed that no surface modification took place in the He atmosphere, while the same positive effect as above was observed in pure hydrogen. However, the pure hydrogen plasma is characterized by markedly lower energetic characteristics of the electron beam, which requires increased exposure durations for the material modification.

In concluding, the use of a He–H_2 discharge–beam plasma for the production of hydrogen ions and their transport to the surface processed provides for a technologically simple method of protonation, while still ensuring an effective ionization process. These features

allow the given plasma type to be employed in simple technologies for the surface modification of materials.

REFERENCES

1. A. N. Sergeev, G. E. Remnev, and S. V. Rudnev, *Thin-Layer Proton-Ion Modification* (Izd. Tomsk. Univ., Tomsk, 1993).
2. H. A. Davis, G. E. Remnev, R. W. Stinnett, and K. Yatsui, in *Intense Ion-Beam Treatment of Materials*, MRS Bull., No. 8, 58 (1996).
3. A. V. Karelin, V. P. Demkin, and S. V. Melnichuk, in *Proceedings of International Conference on Lasers (LASER'96), 1996*, p. 653.
4. Yu. P. Raĭzer, *The Physics of Gas Discharge* (Nauka, Moscow, 1997).
5. V. P. Demkin, S. V. Mel'nichuk, and I. I. Murav'ev, Opt. Atm. Okeana, No. 3, 253 (1993).
6. V. P. Demkin and N. L. Kupchinskiĭ, in *Ionization Processes Involving Excited Atoms* (Leningrad, 1988), pp. 168–169.
7. B. E. Warren, Phys. Rev. **59**, 693 (1941).

Translated by P. Pozdeev

Technical Physics Letters, Vol. 26, No. 4, 2000, pp. 288–291. Translated from Pis'ma v Zhurnal Tekhnicheskoĭ Fiziki, Vol. 26, No. 7, 2000, pp. 43–50.

The Current Column Contraction and Ion Charge Increase Induced by the Current Build-Up in a Pulsed Vacuum Discharge

E. A. Zverev and I. A. Krinberg

Irkutsk State University, Irkutsk, Russia

Received June 3, 1999

Abstract—It is shown that three current build-up regimes may be realized in a pulsed vacuum discharge, depending on the relationship between the pulse duration τ and the characteristic times of the plasma flow (τ_L) and the cathode spot spreading (τ_S). For a rapid build-up ($\tau < \tau_L$), the cathode plasma jet exhibits the neck formation with high values of the plasma temperature and density. At a slow current increase ($\tau_L < \tau < \tau_S$), the current column is subject to a uniform magnetic contraction, while at a very slow current growth rate ($\tau > \tau_S$), the contraction becomes insignificant. The first two cases give rise to additional nonequilibrium ionization in the current column, which leads to the ion charge increasing with the current. The third case is characterized by a "frozen" ion composition corresponding to the plasma parameters in the near-cathode region. © *2000 MAIK "Nauka/Interperiodica".*

1. Introduction. As is known [1–5], the maximum electron temperature $T_e = T_m \approx 4$–8 eV in a cathode plasma column is observed near the cathode surface, at a distance (r) of the order of (or smaller than) the cathode spot size ($r_m \approx 1$ μm), since the electron density in this region is $N_e = N_m \approx 10^{26}$–$10^{27}$ m^{-3} [4–6], the frequency of elastic and inelastic collisions in the plasma is sufficient for the establishing of an ionization equilibrium described by the Saha equations. As the plasma expands with the distance from cathode, the electron concentration rapidly drops by the law $N_e(r) \approx N_m r_m^2/r^2$ and the inelastic collisions become rare. As a result, the plasma exhibits a fast transition from the local thermodynamic equilibrium to a nonequilibrium state. The transition is so rapid that the plasma cannot relax to an equilibrium charged state corresponding to the new values of $T_e(r)$ and $N_e(r)$. As a result, the relative ion composition virtually remains unchanged ("frozen") [7, 8] and corresponds to the initial T_m and N_m values established in the near-cathode region [9, 10]. For this reason, measurements of the ion composition at various distances from the cathode (r = 1–5 cm) give almost the same results [11].

According to [12, 13], the ion composition (and, hence, the average ion charge $Z_0 = 1$–3) is also almost independent of the current in the range $50 < I < 1000$ A, provided that the current pulse duration is sufficiently large ($\tau \geq 250$ μs). These experimental data agree with the commonly accepted notions [14], according to which an increase in the current I only leads to a proportional growth in the number of cathode microspots and the plasma microjets emitted from these spots with the same plasma parameters T_m and N_m. On the other hand, the measurements using pulses with a duration of $\tau = 6$–60 μs showed a significant increase in the average ion charge ($Z > Z_0$) in the range of currents $I = 600$–800 A [15] or even at $I \approx 300$ A in the case of chaotic current fluctuations with $\tau \cong 10^{-2}$ μs [16].

The purpose of this work was to study the effect of current strength on the ion composition of the cathode plasma column at various pulse durations.

2. Mechanism. A natural physical mechanism responsible for the increase in the ion charge with the current strength is apparently the plasma column contraction by the intrinsic magnetic field. The field strength at the plasma jet boundary is determined by a relationship $B = 2I/cR$, where R is the jet radius and c is the velocity of light. The extent of contraction markedly depends on the ratio of the characteristic time of current enhancement (i.e., the pulse duration τ), the time of plasma spreading over the interelectrode gap ($\tau_L \approx L/V \approx 1$ μs, where $L \cong 1$ cm is the gap width and $V \cong (1$–$3) \times 10^6$ cm/s is the plasma velocity) [17], and the time of spot spreading over the cathode surface (τ_S). The latter quantity can be estimated as $\tau_S \approx 100$ μs, which corresponds to the time of establishing of a stable ion composition in a steady-state electric arc in vacuum [12]; approximately the same estimate is obtained from the results of investigation of the cathode spot diffusion [18].

In the case on $\tau > \tau_S$ (called below the regime of very slow current build-up), the new microspots (emission centers [14]) formed in the course of the current build-up can distribute inside the macroscopic cathode spots with an equal surface density [19]. For this reason, the

1063-7850/00/2604-0288$20.00 © 2000 MAIK "Nauka/Interperiodica"

radius of the near-cathode part of the plasma column changes as $R_0 \propto \sqrt{I}$, while the magnetic field strength increases as $B \propto I/R_0 \propto \sqrt{I}$. Since the slow current build-up is accompanied by the formation of several macroscopic cathode spots (separated by distances markedly greater than the microspot spacing [5, 19]), the radius of the cathode plasma column formed upon merging of the separate plasma jets would increase at a greater rate than the magnetic field strength. Therefore, the plasma would exhibit rather insignificant contraction and heating at distances $r \le 3$ cm from the cathode [5]. Consequently, no significant additional ionization would take place and the ion composition remains "frozen" ($Z \approx Z_0$).

As demonstrated previously [17], the case of $\tau < \tau_L \ll \tau_S$ corresponds to a rapid current build-up, whereby the plasma cannot distribute over the interelectrode gap. As a result, the plasma column exhibits rapid contraction (the neck formation) at a distance of $r \approx 1$–2 mm from the cathode and the temperature and electron density increase up to $T_e \approx 10^2$ eV and $N_e \approx 10^{23}$–10^{24} m^{-3}, respectively. Thus, a new special region (in addition to the near-cathode space) representing a dense and hot plasma appears in the column, which features further ionization of the ions supplied from the near-cathode space with $Z_0 = 1$–3. This regime is realized during the chaotic current outbursts (characteristic of the high-voltage breakdown stage) with $\tau \cong 10^{-2}$ μs, whereby the ion charge increases up to 6–7 [16].

Finally, an intermediate regime may take place for $\tau_S > \tau > \tau_L$ (referred to below as the slow current build-up mode). In this case, the plasma is rather uniformly distributed along the discharge gap, but the macroscopic cathode spot and the plasma column base still retain the initial dimensions. The possibility that the macroscopic spot size exhibits small changes is related to the circumstance that new microspots (responsible for the current build-up) are formed under the existing plasma [14, 20]. In this case, $R_0 \cong$ const and $B \propto I$, which implies that the magnetic contraction of the cathode plasma column markedly increases with the current. However, the condition $\tau > \tau_L$ implies that no neck is formed and the column contraction and heating are more uniform and less significant.

3. Calculation. The slow current build-up regime was studied using a magnetodynamic model of the cathode plasma column described in detail in [5, 17]. The boundary conditions in the near-cathode space were determined by taking $R_0 = 150$ μm, the ion velocity $V_0 \approx 4(5Z_0T_m/3m)^{1/2}$ (m being the ion mass), and $T_e = 0.4\ T_m$ [5]. Here $Z_0 = 2$, $T_m = 5$ eV (for a Cu or Ti cathode) and $Z_0 = 3$, $T_m = 7$ eV (for W cathode) [10, 11]. The supply of substances through the boundary cross-section was assumed to be proportional to the current strength [17]. The current strength variation with time was described by the function $I(t) = I_0 + I_1(\sin(\pi t/\tau))$.

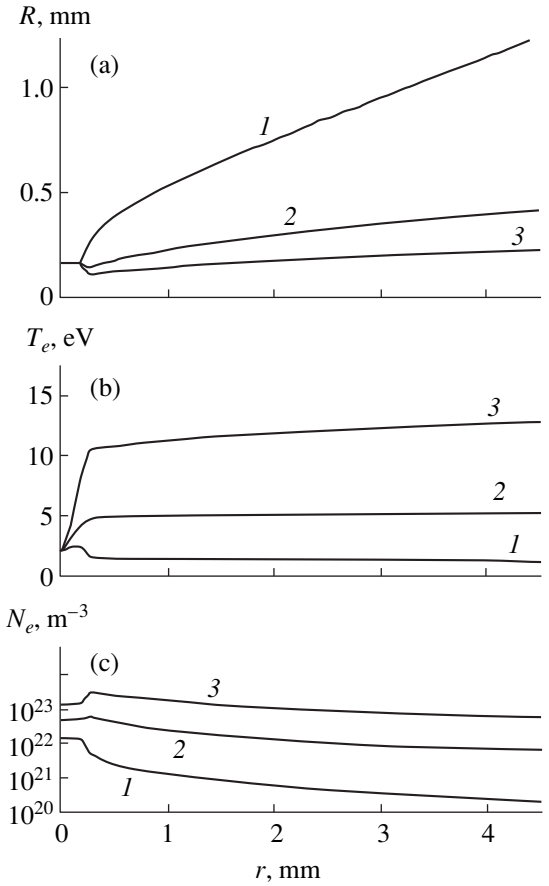

Fig. 1. Distributions of the cathode plasma column parameters along the column calculated at the peak of a current pulse with the amplitude $I = 200$ (*1*), 700 (*2*) and 1800 A (*3*) (r is the distance from cathode): (a) column radius R; (b) electron temperature T_e; (c) electron concentration N_e.

The initial distributions were represented by the $T_e(r)$ and $N_e(r)$ functions calculated for a stationary current of $I_0 = 200$ A, at which the effect of the magnetic field on the cathode plasma column parameters at a distances $r < 3$ cm can be neglected [5]. The calculations were performed for current pulses with the duration $\tau = 6$ μs and the amplitudes $I_1 = 500$ A and 1600 A.

Figure 1 shows distributions of the cathode plasma column parameters calculated for the current pulse peak ($t = \tau/2$, $I = I_p = I_0 + I_1$). As is seen, an increase in the current is accompanied by decreasing column cross-section and increasing temperature and density of the plasma. In comparison to the case of low-current arc ($I_1 = 0$, $I_p = I_0 = 200$ A), the plasma density increases by one–two orders of magnitude but still remains markedly lower than the value N_m characteristic of the near-cathode region. At the same time, the electron temperature in most part of the plasma column increases up to T_m or even above this level, which may lead to additional ionization of the ions coming from the near-cathode region.

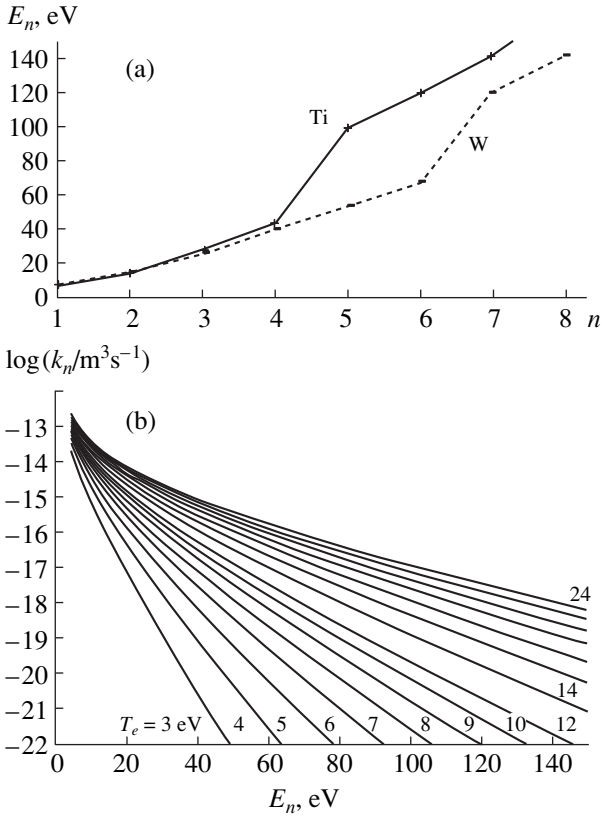

Fig. 2. Ionization characteristics for the formation of ions with the charge n: (a) ionization energy E_n; (b) ionization coefficient k_n.

4. Results and discussion. The estimates obtained for $N_e \le 10^{23}$ m^{-3} (Fig. 1) and a characteristic plasma column size of $L = 1$ cm show that the equilibrium ionization regime is not established and the Saha equations are inapplicable to calculation of the ion composition. Since the rate of the ternary recombination process is proportional to N_e^2 and the rate of impact ionization is proportional to N_e, the recombination can be neglected in the column part outside the near-cathode space (where $N_e \ll N_m$). The probability of ion formation with a charge n during the flight time τ_L can be evaluated from the relationship $P_n = \tau_n/\tau_L$, where τ_n is the characteristic ionization time. The latter quantity is determined from the formula $\tau_n^{-1} = \langle v_e \sigma_n \rangle N_e$, where $\sigma_n(v_e)$ is the cross-section of ionization of an ion with the charge $n-1$ by an electron moving with the velocity v_e. Using the Grizinskiĭ formula [21] for the electron impact ionization cross-section of ions and averaging over the Maxwell electron velocity distribution, we obtain [2]

$$k_n = \langle v_e \sigma_n \rangle = \sigma_0 \left(\frac{8T_e}{\pi m_e}\right)^{1/2} \left(\frac{E_0}{E_n}\right)^2 \exp(-E_n/T_e), \quad (1)$$

where $\sigma_0 \approx 10^{-20}$ m^2, $E_0 = 13.6$ eV, and E_n and k_n are the ionization energy and coefficient. The results of calculations according to formula (1), performed for various T_e and E_n values, are presented in Fig. 2.

As is seen from Fig. 1, the electron concentration and temperature in the system with $I \ge 700$ A exhibit rather weak variation along the plasma column axis and can be replaced by their mean values $\bar{N}_e$ and $\bar{T}_e$ (see table). Assuming that $P_n = 1$, we obtain an approximate relationship $k_n(E_n, \bar{T}_e) = (\tau_L \bar{N}_e)^{-1}$ which can be used to determine the energy $E_n(n)$ (for any given values of $\bar{N}_e$ and $\bar{T}_e$) and the charge n (from the E_n as function of n). The value of n (probably, fractional) determined by this method approximately corresponds to an average ion charge ($Z \approx n$), since there is probability ($P_{n+1} < 1$) of forming ions with a charge of $n + 1$, on the one hand, and the possibility that ions with a charge smaller than n are partly retained or newly formed, on the other hand.

The results of determination of the average ion charge $Z \approx n$ for a cathode plasma column with the model parameters studied (Fig. 1) are presented in the table. As seen, the $\bar{N}_e$ and $\bar{T}_e$ values characteristic of the current I strength = 200 A lead to no additional ionization in the main part of the plasma column (the calculate E_n value is below the minimum ionization energy). Therefore, the system would retain the initial ("frozen") ion composition corresponding to the

Variation of the plasma column parameters depending on the current strength

Cathode	I, A	$\bar{T}_e$, eV	$\bar{N}_e$, m^{-3}	E_n, eV	Z	Z_{exp}	I_{exp}, A	τ_{exp}, μs
Ti	200	1.5	10^{21}	$<E_1$	(2.0)	2.2 ± 0.2	200	250
	700	5	10^{22}	22	2.6	2.4 ± 0.3	560	60
	1800	12	10^{23}	57	4.3	3.5 ± 0.3	1860	6
W	200	2	10^{21}	$<E_1$	(3.0)	3.0 ± 0.3	200	100
	700	7	10^{22}	30	3.4	4.4 ± 0.4	800	6–12
	1800	17	10^{23}	76	6.2	5.9 ± 0.6	1860	6–12

parameters of plasma in the near-cathode region (these Z_0 values are given in the table in parentheses). For $I > 500$ A, the ion charge increase becomes significant ($Z > Z_0$) because of the additional nonequilibrium ionization in the plasma column. The calculated Z values agree well with the experimental data (Z_{exp}) reported [15] for the current pulses with the parameters I_p and τ close to the values used in our model calculations.

REFERENCES

1. B. Ya. Moĭzhes and V. A. Nemchinskiĭ, Zh. Tekh. Fiz. **50**, 78 (1980) [Sov. Phys. Tech. Phys. **25**, 43 (1980)].
2. C. Wieckert, Contrib. Plasma Phys. **27**, 309 (1987).
3. I. A. Krinberg, M. P. Lukovnikova, and V. L. Papernyĭ, Zh. Éksp. Teor. Fiz. **91**, 806 (1990) [Sov. Phys. JETP **70**, 451 (1990)].
4. B. Jüttner and A. Forster, in *Proceedings of the 17th International Symposium on Discharges and Electrical Insulation in Vacuum, Berkeley, 1996*, Vol. 1, pp. 118–122.
5. I. A. Krinberg and E. A. Zverev, Fiz. Plazmy **25**, 88 (1999) [Plasma Phys. Rep. **25**, 82 (1999)].
6. A. Anders, S. Anders, B. Juttner, and H. Luck, IEEE Trans. Plasma. Sci. **24**, 69 (1996).
7. S. Anders and A. Anders, J. Phys. D: Appl. Phys. **21**, 213 (1988).
8. A. Anders, Phys. Rev. E **55**, 969 (1997).
9. I. A. Krinberg and M. P. Lukovnikova, J. Phys. D: Appl. Phys. **28**, 711 (1995).
10. I. A. Krinberg and M. P. Lukovnikova, J. Phys. D: Appl. Phys. **29**, 2901 (1996).
11. I. G. Brown and J. E. Galvin, IEEE Trans. Plasma Sci. **17**, 679 (1989).
12. J. E. Galvin, I. G. Brown, and R. A. MacGill, Rev. Sci. Instrum. **61**, 583 (1990).
13. A. G. Nikolaev, E. M. Oks, and G. Yu. Yushkov, Zh. Tekh. Fiz. **43**, 39 (1998) [Tech. Phys. **43**, 514 (1998)].
14. G. A. Mesyats, Usp. Fiz. Nauk **165**, 601 (1995) [Phys. Usp. **165**, 567 (1995)].
15. A. Anders, I. G. Brown, M. R. Dickinson, and R. A. MacGill, Rev. Sci. Instrum. **67**, 1202 (1996).
16. E. D. Korop and A. A. Plyutto, Zh. Tekh. Fiz. **41**, 1055 (1971) [Sov. Phys. Tech. Phys. **16**, 830 (1971)].
17. E. A. Zverev and I. A. Krinberg, Pis'ma Zh. Tekh. Fiz. **24**, 50 (1998) [Tech. Phys. Lett. **24**, 728 (1998)].
18. A. Anders, S. Anders, B. Jüttner, and I. G. Brown, IEEE Trans. Plasma Sci. **21**, 305 (1993).
19. P. Siemroth, T. Schulke, and T. Witke, IEEE Trans. Plasma Sci. **23**, 919 (1995).
20. V. F. Puchkarev and M. B. Bochkarev, J. Phys. D: Appl. Phys. **27**, 1214 (1994).
21. B. M. Smirnov, *Atomic Collisions and Elementary Processes in Plasma* (Atomizdat, Moscow, 1968).

Translated by P. Pozdeev

Technical Physics Letters, Vol. 26, No. 4, 2000, pp. 292–294. Translated from Pis'ma v Zhurnal Tekhnicheskoĭ Fiziki, Vol. 26, No. 7, 2000, pp. 51–56.

Reverse Current in Semiconductor Diodes with Inhomogeneous Base

B. S. Sokolovskiĭ

Franko State University, Lviv, 290005 Ukraine

Received April 13, 1999; in final form, November 15, 1999

Abstract—The reverse current in a semiconductor diode with inhomogeneous base has been calculated. The base was modified so as to contain a layer with increased bandgap, adjacent to the ohmic contact. It is demonstrated that this modification may dramatically reduce the reverse current related to the thermal carrier generation both in the base and at the ohmic contact. © *2000 MAIK "Nauka/Interperiodica".*

Reducing the reverse current of *p–n* junctions is an important problem both in engineering and in academic research, since it can significantly improve the performance of many devices constructed on the basis of semiconductor diodes, in particular, detectors, radiation counters, solar cells, etc., as well as in other junction-based electronic components [1]. One way to solve this task is to reduce the contribution of diffusion current, related to the thermal generation of minority carriers in the quasineutral base of a reverse-biased diode. It is a common practice to reduce the diffusion current component by raising the doping level of the base. However, possibilities of this approach are limited, since strong doping leads to concomitant shortening of the lifetime of minority carriers and narrowing of the bandgap, these factors hindering a decrease in the rate of carrier production. Another factor that adds to reverse current is the thermal carrier generation in the ohmic contact, which becomes a challenge if the length of the base is close to or shorter than the diffusion length of minority carriers. To compensate for this effect, one may increase the dopant concentration near the ohmic contact (inhomogeneous doping). Unfortunately, the strategy would work poorly, since the barrier for the carriers supplied from the contact can only be raised by about kT or so [1].

This study theoretically demonstrates that the reverse current of a *p–n* junction can be decreased appreciably if an isotype region with increased bandgap is created in the base of the diode.

The reverse current of a semiconductor diode will be calculated in terms of the energy band diagram depicted in Fig. 1. Let the diode base have the *p*-type conductivity, be uniformly doped with acceptors to a concentration of N_a and contain two regions with homogeneous bandgaps, the region adjacent to the ohmic contact having a larger bandgap E_{gl} as compared to that (E_{gs}) in the other part of the diode ($E_{gl} > E_{gs}$). The small-bandgap and the large-bandgap regions have thicknesses d_{ns} and d_{nl}, respectively, and are separated by a variband layer of thickness d_{nv}. We assume that d_{nv} is much smaller than d_{nl}, d_{ns}, and the electron diffusion length.

In order to evaluate the reverse current, we must know the nonequilibrium electron concentration $n(x)$ in the base when a reverse bias U is applied to the *p–n* junction, that the electric field in the base under reverse bias can be neglected and the uniform-bandgap regions are quasilinear, we obtain the continuity equations

$$\frac{d^2n}{dx^2} - \frac{1}{L_{ns,l}^2}\left(n - \frac{n_{is,l}^2}{N_a}\right) = 0 \qquad (1)$$

for $0 \le x \le d_{ns}$ and $d_{ns} + d_{nv} \le x \le d_{ns} + d_{nv} + d_{nl}$, corresponding to subscripts "s" and "l", respectively. Here, n_{is} and n_{il} are the intrinsic carrier concentrations and L_{ns} and L_{nl} are the electron diffusion lengths in the small-bandgap and the large-bandgap regions, respectively. The diffusion lengths are related to the corresponding electron diffusion coefficients, D_{ns} and D_{nl}, and the electron lifetimes, τ_{ns} and τ_{nl}, as $L_{ns,l} = (D_{ns,l}\tau_{ns,l})^{1/2}$.

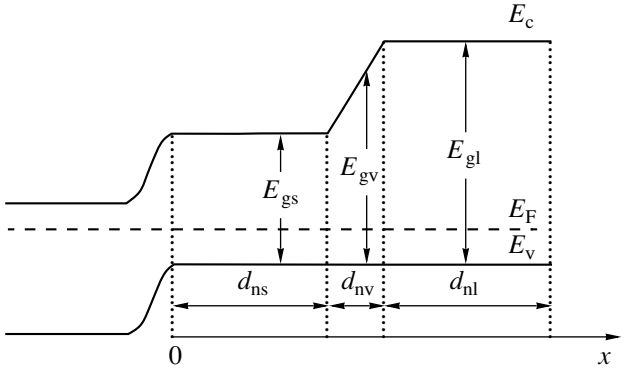

Fig. 1. Equilibrium energy band diagram of a *p–n* diode.

1063-7850/00/2604-0292$20.00 © 2000 MAIK "Nauka/Interperiodica"

At $x = 0$ and $x = d_n \equiv d_{ns} + d_{nv} + d_{nl}$, the boundary conditions for equations (1) are traditional:

$$n(0) = \frac{n_{is}^2}{N_a}\left[\exp\left(\frac{U}{kT}\right) - 1\right] (U < 0), \quad (2)$$

$$n(d_n) = \frac{n_{il}^2}{N_a}. \quad (3)$$

Equations (2) and (3) must be supplemented with conditions at the boundaries of the variband region, reflecting constant electron current and the Boltzmann distribution of charge carriers in the variband region [2]:

$$D_{ns}\frac{dn}{dx}\bigg|_{x = d_{ns}} = D_{nl}\frac{dn}{dx}\bigg|_{x = d_{ns} + d_{nv}}, \quad (4)$$

$$\frac{n(d_{ns})}{n(d_{ns} + d_{nv})} \equiv \zeta = \frac{N_c(d_{ns})}{N_c(d_{ns} + d_{nv})}\exp\left(\frac{E_{gl} - E_{gs}}{kT}\right), \quad (5)$$

where $N_c = 2(2\pi m_n^* kT/h^2)^{3/2}$ is the effective density of states in the conduction band and m_n^* is the effective electron mass (generally, coordinate-dependent).

Once equations (1) with the boundary conditions (2)–(5) are solved to determine the nonequilibrium electron density profile in the homogeneous base regions, one can evaluate the density of reverse current, or more correctly, the electron current component. Using relationships

$$j_{nr} = j_n(0) = eD_{ns}\frac{dn}{dx}\bigg|_{x = 0}, \quad (6)$$

we obtain for $|U| \gg kT$

$$j_{nr} = \frac{eD_{ns}n_{is}^2}{L_{ns}N_a}\frac{\kappa\cosh\frac{d_{ns}}{L_{ns}}\cosh\frac{d_{nl}}{L_{nl}} + \zeta\sinh\frac{d_{nl}}{L_{nl}}\sinh\frac{d_{ns}}{L_{ns}}}{\kappa\sinh\frac{d_{ns}}{L_{ns}}\cosh\frac{d_{nl}}{L_{nl}} + \zeta\sinh\frac{d_{nl}}{L_{nl}}\cosh\frac{d_{ns}}{L_{ns}}}, \quad (7)$$

where $\kappa = \frac{L_{nl}\tau_{ns}}{L_{ns}\tau_{nl}}$.

Note that, for $d_{nl} = 0$ (i.e., when the base contains no large-bandgap region) equation (7) gives well-known expressions for the diffusion reverse current [1]:

$$j_{nr} = j_{nr}^* = \frac{eD_{ns}n_{is}^2}{L_{ns}N_a}, \quad (8)$$

$$j_{nr} = \frac{eD_{ns}n_{is}^2}{L_{ns}N_a}\coth\frac{d_{ns}}{L_{ns}}, \quad (9)$$

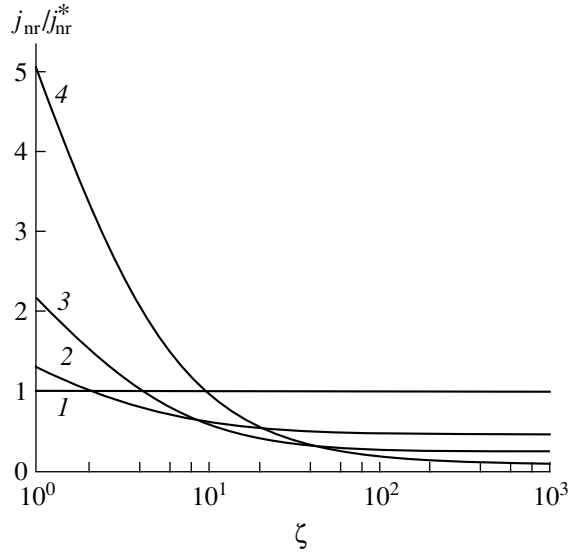

Fig. 2. The plots of relative reverse current density vs. base inhomogeneity parameter for $\kappa = 1$, $d_{ns} = d_{nl}$, $L_{ns} = L_{nl}$, and $d_n/L_{ns} = (1)$ 5, (2) 1, (3) 0.5, or (4) 0.2.

corresponding to the cases of $d_{ns} \gg L_{ns}$ (thick homogeneous base) or $d_{ns} \leq L_{ns}$ (thin base).

Formula (7) indicates that the reverse current is reduced owing to the presence of a large-bandgap region separated from the space-charge region by a distance of the order of minority carrier diffusion length (or shorter). The effect is stronger for a greater difference between E_{gl} and E_{gs} or a shorter distance between the large-bandgap region and the metallurgical boundary of the p–n junction (see Fig. 2). For $\zeta \gg L_{ns}L_{nl}/(d_{ns}d_{nl})$ and $|U| \gg kT$, formula (7) can be simplified as follows:

$$j_{nr} = \frac{eD_{ns}n_{is}^2}{L_{ns}N_a}\tanh\frac{d_{ns}}{L_{ns}}. \quad (10)$$

Thus, at a large ζ, the reverse current due to the ohmic contact is virtually eliminated even if the contact lies near the space-charge region ($d_n \ll L_{ns}, L_{nl}$). Moreover, the reverse current proves to be even smaller than the minimum value j_{nr}^* for a diode with the homogeneous base, since the large-bandgap region inhibits a decrease in the overall thermal carrier production rate in the base. According to equations (9) and (10) for $d_{ns} \ll L_{ns}$ and $\zeta \gg L_{ns}L_{nl}/(d_{ns}d_l)$, respectively, the ratio of reverse currents of the homogeneous and heterogeneous diodes with the same d_{ns} is

$$\frac{j_{nr}^{hom}}{j_{nr}^{het}} = \left(\frac{L_{ns}}{d_{ns}}\right)^2 \gg 1. \quad (11)$$

This result is evidence in favor of the heterogeneous diode structure suggested above.

In conclusion, we will estimate the effect of the base inhomogeneity on the reverse current of an n^+–p photodiode based on a $Cd_xHg_{1-x}Te$ system with $x = 0.21$. Let the p region thickness be 50 μm, the electron mobility 4×10^4 cm^2/(V s), and the electron lifetime 1 μs (at 77 K) [3]. If the large-bandgap region adjacent to the ohmic contact has $x = 0.23$ (so that $\zeta = 110$) and a thickness of 30 μm, the reverse current is reduced by a factor of 19. As a result, the noise level decreases by a factor of 4.4.

REFERENCES

1. S. Sze, *Physics of Semiconductor Devices* (Wiley, New York, 1981; Mir, Moscow, 1984).
2. O. V. Konstantinov and G. V. Tsarenkov, Fiz. Tekh. Poluprovodn. (Leningrad) **10**, 720 (1976) [Sov. Phys. Semicond. **10**, 427 (1976)].
3. N. N. Berchenko, V. E. Krevs, and V. G. Sredin, *Semiconducting Solid Solutions: Properties and Applications* (Izd. MO SSSR, Moscow, 1982).

Translated by A. A. Sharshakov

Technical Physics Letters, Vol. 26, No. 4, 2000, pp. 295–297. Translated from Pis'ma v Zhurnal Tekhnicheskoĭ Fiziki, Vol. 26, No. 7, 2000, pp. 57–63.

Mesastripe Single-Mode Separately Bounded Lasers Based on InGaAsP/InP Heterostructures Obtained by VPE of Organometallic Compounds

E. G. Golikova, V. A. Gorbylev, Yu. V. Il'in, V. A. Kureshov, A. Yu. Leshko, A. V. Lyutetskiĭ, N. A. Pikhtin, Yu. A. Ryaboshtan, V. A. Simakov, I. S. Tarasov, E. A. Tret'yakova, and N. V. Fetisova

Ioffe Physicotechnical Institute, Russian Academy of Sciences, St. Petersburg, Russia

Received November 10, 1999

Abstract—Mesastripe single-mode InGaAsP/InP laser diode heterostructures with an optical emission power of 200 mW in the continuous lasing mode at two wavelengths (1.3 and 1.55 μm) were obtained by metalorganic VPE. In the samples with a mesastripe contact width of $W = 5$ μm, the single-mode lasing regime was observed in the entire range of pumping currents. For a cavity length of 1.0–2.5 mm, the threshold current densities varied within 450–600 A/cm^2. The differential quantum efficiency reached 30–40%. The internal optical losses in the mesastripe laser heterostructures are reduced to 7.7 cm^{-1}. The output power–pumping current characteristics of control samples remained unchanged upon testing for 1500 h at 50°C. © *2000 MAIK "Nauka/Interperiodica".*

The concept of increasing the power of laser diodes by decreasing internal optical losses is now commonly recognized [1–3]. A similar approach has been successfully used to create laser heterostructures emitting in the long-wavelength range (λ = 1.3–1.55 μm) [4, 5]. From the standpoint of the long-wavelength range, of special interest are the single-mode laser diode structures. The single-mode laser heterostructure technology involves some post-growth operations (etching of mesastripes, healing, etc.) introducing additional internal optical losses.

The purpose of this work was to develop the concept of separately bounded (SB) laser heterostructures with low internal optical losses for high-power single-mode laser diodes emitting in the 1.3–1.5 μm wavelength. The technology is based on the method of vapor-phase epitaxy of organometallic compounds (metalorganic-hydride VPE) [6] and the post-growth technology of mesastripe single-mode lasers [7].

Using the metalorganic-hydride VPE technique, we have fabricated SB double InGaAsP heterostructures with two 50-Å-thick stressed quantum wells on *n*-InP substrates. The sample structures were prepared with the InGaAsP solid solution compositions corresponded to the wavelengths λ = 1.3 and 1.55 μm. The quantum wells were separated by an intermediate waveguide layer with a thickness of 150 Å, and the total waveguide layer thickness was about 1 μm for both samples structures. The bandgap widths of the solid solutions in the waveguide layers were E_g = 1.25 eV and 1.1 eV for the structures emitting at 1.3 and 1.55 μm, respectively. Neither the active region nor the waveguide layers were intentionally doped. A 1.2-μm-thick *P*-emitter was doped to a carrier concentration of 7×10^{17} cm^{-3} and a contact *p*-type layer with a thickness of 0.3 μm had a hole concentration of 2×10^{18} cm^{-3}.

The mesastripe laser diodes were fabricated using the above heterostructures by conventional procedures described elsewhere [7]. An important modification consisted in replacing the operation of chemical pickling by ion-plasma etching of the mesastripes to a preset depth (0.1–05 μm toward a waveguide layer). This operation was effected on an Alkatel Model 350 setup. The mesastripe contact width was 5 μm. The samples were provided with ZnAu and TeAu ohmic contacts deposited by thermal evaporation in vacuum. The resonator edges were coated with Si/SiO_2 mirrors with a reflection coefficient of $R > 0.95$ and clarifying layers with $R < 0.04$. Finally, the laser diode samples were mounted by soldering onto copper heat-exchangers. The optical lengths of the resonator varied within 500–2500 μm.

Figure 1 shows the plots of output power *P* versus pumping current *I* for the typical laser diodes with λ = 1.3 and 1.55 μm. At an output power of 150–200 mW and a pumping current of the order of one ampere, the *P–I* curves exhibit bending caused by heating of the active region. The differential resistance of these laser diodes (about 0.5 Ω) was somewhat inferior to that of the four-cleavage samples because of the post-growth operations. For a resonator length of 1200 μm, the differential quantum efficiency in the initial portion of the *P–I* curve was retained on a level of 30–40%. The threshold current of the laser diodes was 25–35 mA, which corresponded to a threshold current density of 450–600 A/cm^2. In the four-cleavage samples prepared

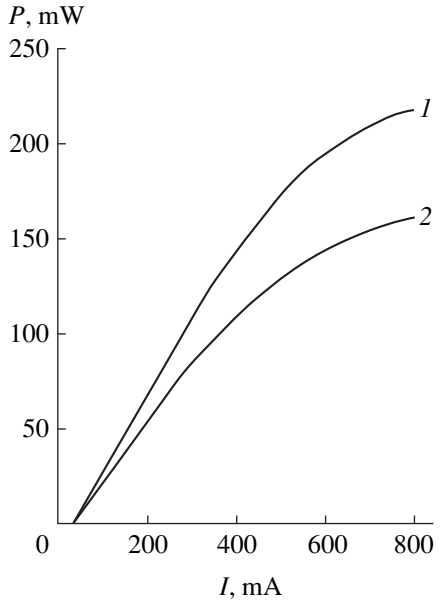

Fig. 1. The plots of output power P versus pumping current I for the mesastripe single-mode laser diodes with a resonator length L = 1200 μm emitting at λ = 1.3 (*1*) and 1.55 μm (*2*) in the continuous lasing regime at 20°C.

using the same structures, the threshold current density was 160–200 A/cm^2. We believe that the difference is explained by lower resonator length and by additional internal optical losses introduced during the formation of narrow mesastripes.

The samples with a mesastripe contact width of W = 5 μm exhibited a singe-mode lasing in the entire range of pumping currents studied. Figure 2 shows a pattern of the long-range field in a plane parallel to the p–n junction ($\theta_\parallel = 15°$). The absence of significant changes in the long-range field distribution is evidence of a sufficiently high waveguide effect in the mesastripe contact. The long-range field pattern in the plane perpendicular to the p–n junction was also indicative of a zero-mode generation ($\theta_\perp = 45°$) despite a waveguide layer thickness of 1 μm.

The emission spectrum of the single-mode laser diode exhibited broadening with the pumping current (Fig. 3), which was caused by two factors: the gain saturation in the quantum-size regions and the heating of these regions. The samples of laser diodes based on the heterostructures of both types studied (with λ = 1.3 and 1.55 μm) had T_0 = 70–80 K.

Figure 4 shows the plots of inverse differential quantum efficiency $1/\eta_d$ versus the resonator length L for the laser diodes with wide (W = 100 μm) and mesastripe (W = 5 μm) contacts. The internal optical losses in the mesastripe structure (7.7 cm^{-1}) are somewhat greater as compared to those (4.2 cm^{-1}) in the lasers with wide contact. This increase in the optical losses is caused by the post-growth operations involved in the mesastripe structure fabrication. The further increase in the output power in these lasers can be achieved by optimizing the laser heterostructure parameters and the single-mode laser design.

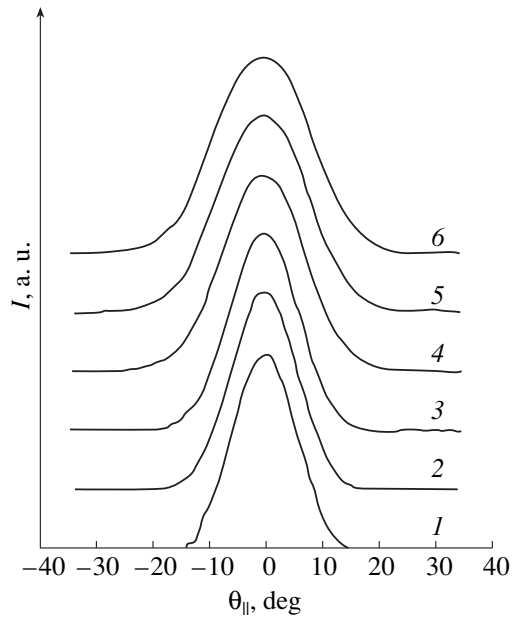

Fig. 2. The pattern of long-range field distribution in a plane parallel to the p–n junction of a mesastripe single-mode laser diode operating at λ = 1.55 μm in the continuous lasing regime at 20°C and various pumping currents I = 50 (*1*); 100 (*2*); 200 (*3*); 300 (*4*); 400 (*5*); 500 mA (*6*).

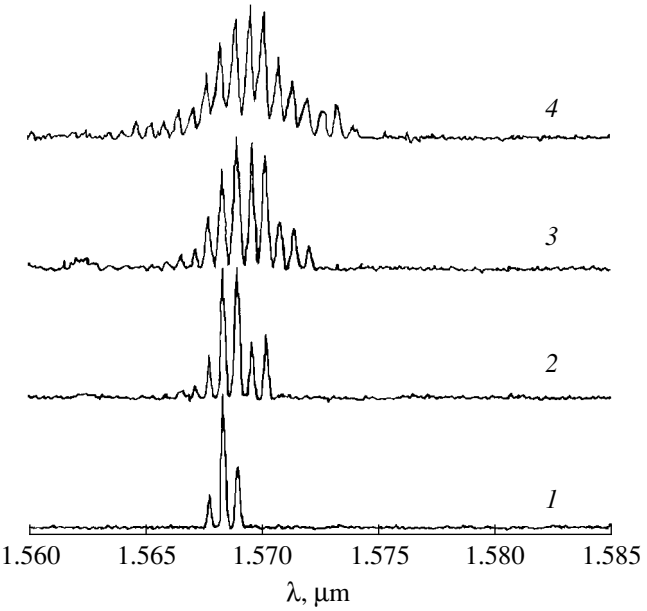

Fig. 3. Emission spectra of a single-mode laser diode operating at 20°C in the continuous lasing regime at various pumping currents I = 50 (*1*); 100 (*2*); 300 (*3*); 500 mA (*4*).

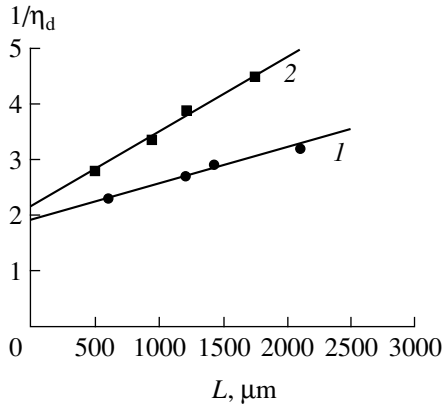

Fig. 4. The plots of inverse differential quantum efficiency $1/\eta_d$ versus the resonator length L for 1.55-μm laser heterostructures (*1*) with a single wide contact (W = 100 μm) and (*2*) a mesastripe contact (W = 5 μm): (*1*) η_i = 53%, α_i = 4.2 cm^{-1}; (*2*) η_i = 47%, α_i = 7.7 cm^{-1}.

A series of five samples was tested for the durability of operation at an elevated temperature of 50°C. Each sample was tested at a working current corresponding to half of the maximum optical output power. No changes in the *P–I* characteristics of all the samples were observed upon a 1500-h testing.

Thus, we have fabricated and studied single-mode InGaAsP/InP laser diodes with an optical output power of 200 mW emitted in the continuous regime at the wavelengths 1.3 and 1.55 μm, respectively. The laser heterostructures were fabricated using the metalorganic-hydride VPE method and a post-growth mesastripe laser technology. The level of internal optical losses in mesastripe lasers is reduced to 7.7 cm^{-1}.

The work was supported by the State Interinstitution Scientific-Technological Program “Physics of Solid-State Nanostructures,” project nos. 97-1035, 99-2037, and 99-2038.

REFERENCES

1. J. K. Wade, J. L. Mawst, D. Botez, *et al.*, Appl. Phys. Lett. **72**, 4 (1998).
2. J. Wang, B. Smith, X. Xie, *et al.*, Appl. Phys. Lett. **74**, 1525 (1999).
3. L. J. Mawst, A. Bhattacharya, J. López, *et al.*, Appl. Phys. Lett. **69**, 532 (1996).
4. D. Garbuzov, L. Xu, S. R. Forrest, *et al.*, Electron. Lett. **32**, 1717 (1996).
5. A. Bhattacharya and D. Botez, Appl. Phys. Lett. **72**, 138 (1999).
6. E. G. Golikova, V. P. Duraev, S. A. Kozikov, *et al.*, Kvant. Élektron. (Moscow) **22**, 105 (1995).
7. M. A. Ivanov, N. D. Il’inskaya, Yu. V. Il’in, *et al.*, Pis’ma Zh. Tekh. Fiz. **21**, 70 (1995) [Tech. Phys. Lett. **21**, 198 (1995)].

Translated by P. Pozdeev

Technical Physics Letters, Vol. 26, No. 4, 2000, pp. 298–301. Translated from Pis'ma v Zhurnal Tekhnicheskoĭ Fiziki, Vol. 26, No. 7, 2000, pp. 64–69.

Single-Crystalline GaAs, AlGaAs, and InGaAs Layers Grown by Metalorganic VPE on Porous GaAs Substrates

Yu. N. Buzynin, S. A. Gusev, V. M. Danil'tsev, M. N. Drozdov, Yu. N. Drozdov, A. V. Murel', O. I. Khrykin, and V. I. Shashkin

Institute of Microstructure Physics, Russian Academy of Sciences, Nizhni Novgorod, Russia

Received September 23, 1998; in final form, November 15, 1999

Abstract—Conditions for the growth of single-crystalline GaAs, AlGaAs, and InGaAs layers by metalorganic VPE were established and the corresponding semiconductor films were obtained on porous GaAs substrates. Comparative data on the morphology, structure, and electrical homogeneity of the epitaxial layers grown on the porous and monolithic substrates are presented. It was found that passage to the porous substrates leads to changes in the film growth rate and morphology, the concentration of electrically active defects, and their distribution in depth of the epitaxial structures. *© 2000 MAIK "Nauka/Interperiodica".*

Porous substrates are promising materials for the obtaining of both homo- and heteroepitaxial semiconductor layers possessing perfect structure. It was reported [1] that defect-free silicon layers were obtained by MBE on porous silicon substrates. Perfect layers of lead sulfide [2] and lead telluride [3], suited for the fabrication of optoelectronic devices, were grown on porous silicon substrates despite a considerable difference in the lattice constants and the temperature expansion coefficients between film and substrate.

In this paper, we report on the properties of single-crystalline GaAs, AlGaAs, and InGaAs layers grown for the first time on porous gallium arsenide by VPE from organometallic compounds and arsine. The substrates were represented by tellurium-doped ($N = 2 \times 10^{18}$ cm^{-3}) single-crystalline GaAs(100) wafers. One part of the wafer was modified by electrochemical etching so as to form a porous GaAs layer [4], while the other part was free of such layer. This allowed us to perform a comparative study of layers obtained on the porous and monolithic parts of the same substrate under identical growth conditions. The initial organometallic compounds included trimethylgallium, trimethylaluminum, trimethylindium, and arsine. The films were grown at atmospheric pressure in a vertical induction-heated reactor using Pd-filtered hydrogen as the carrier gas. The GaAs, InGaAs, and AlGaAs layers were grown at 620, 550, and 700°C, respectively. The as-grown films were studied by electron microscopy, X-ray diffraction, secondary-ion mass spectrometry (SIMS), and electrochemical *C–V* depth profiling.

It was established that properties of the initial porous GaAs layer, containing excess As and having a lattice parameter decreased as compared to that of the initial single-crystalline GaAs ($\Delta\alpha/\alpha_\perp = -2.5 \times 10^{-4}$), slightly changed upon preliminary annealing of the substrates. The lattice parameter increased, approaching that of the monolithic single-crystalline GaAs, and the excess As atoms coalesced to form clusters with a size of 1–10 nm and an atomic density reaching up to 4×10^{18} cm^{-3}. At the same time, the porous GaAs layer retained single-crystalline structure of the initial monolithic substrate and had a mirror-smooth surface suited for epitaxial growth.

Morphology of the outer surface and transverse cleavages of the epitaxial layers of GaAs, AlGaAs, and InGaAs layers grown on monolithic and porous substrates were studied by scanning electron microscopy (SEM) on a Jeol JEM-2000 EX electron microscope. The SEM images showed that layers formed on the porous substrates had, as a rule, more smooth and homogeneous surface and exhibited a lower density of growth defects, as compared to analogous properties of the films grown on monolithic parts of the same samples. Figure 1 shows a typical pattern of surface morphology of the epitaxial AlGaAs layers grown on the monolithic and porous gallium arsenide. A characteristic feature of the epitaxial films grown on the porous GaAs is the presence of step echelons, which is evidence of the lateral growth mechanism. Examination of the transverse cleavages of the epitaxial structures obtained on porous substrates (Figs. 1c and 1d) clearly reveals the porous GaAs layer with a skeleton of pores and spacers.

The structure of epitaxial layers was studied by X-ray diffractometry. The measurements were performed on a double-crystal spectrometer with GaAs(100) single crystal monochromator using a Cu$K\alpha$1 radiation. It was established that GaAs, AlGaAs, and InGaAs layers grown on both monolithic

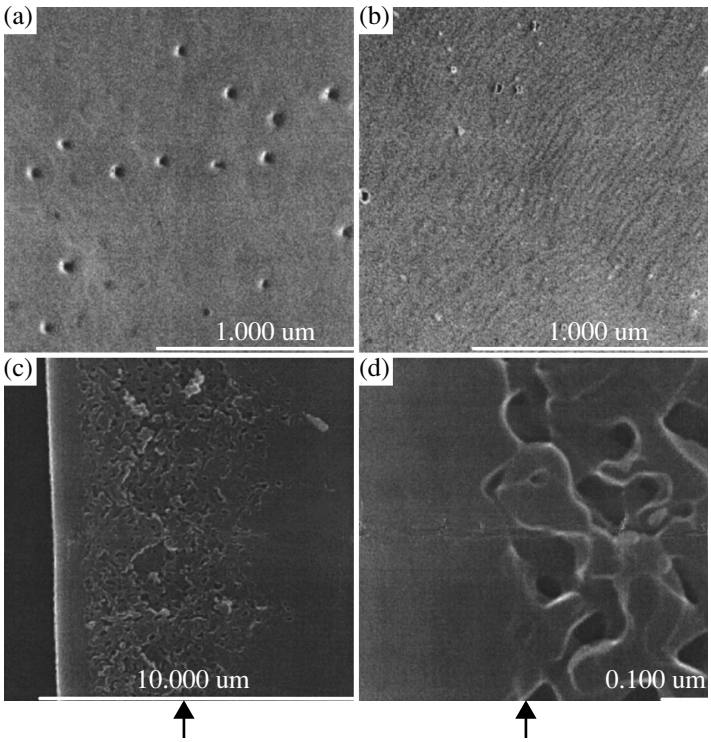

Fig. 1. SEM images of the (a, b) outer surface and (c, d) transverse cleavages of epitaxial AlGaAs layers grown on (a) monolithic and (b–d) porous GaAs substrates. Arrows indicate the boundary between epitaxial film and porous substrate.

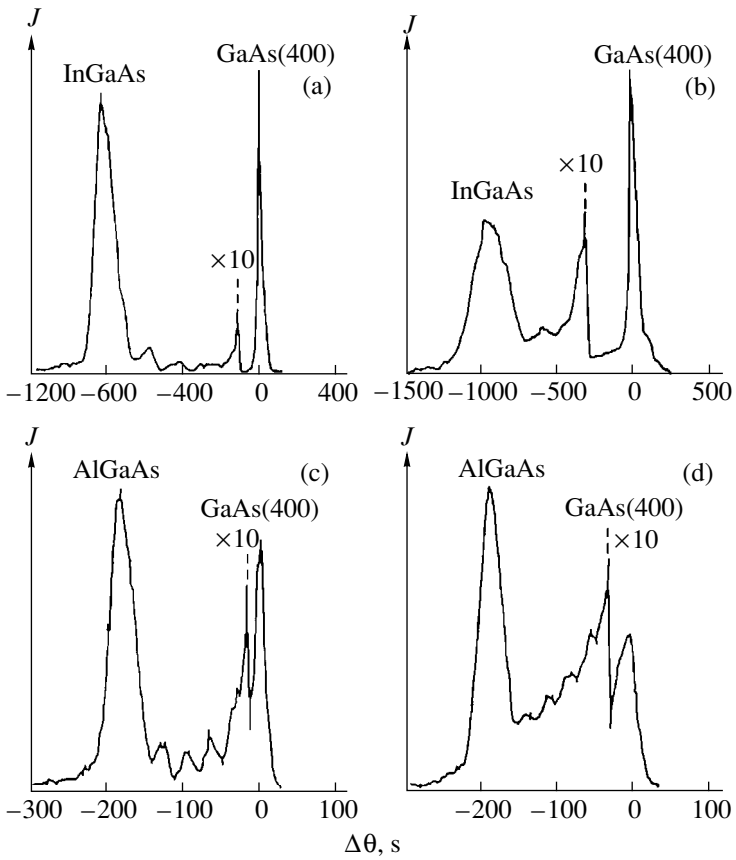

Fig. 2. The rocking curves of X-ray diffraction in the region of the GaAs(400) reflection from epitaxial (a, b) InGaAs and (c, d) AlGaAs layers grown on (a, c) monolithic and (b, d) porous GaAs substrates.

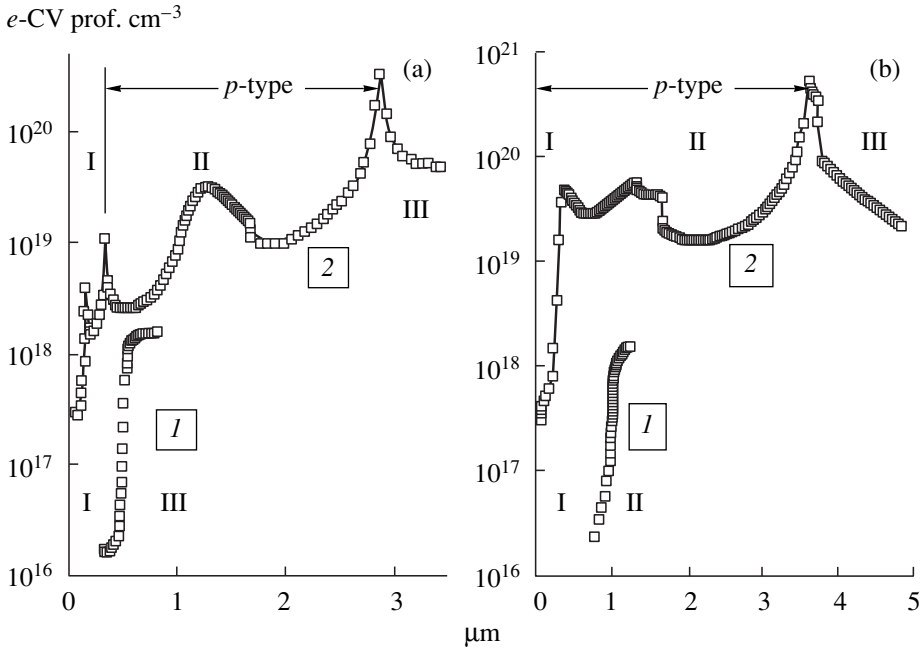

Fig. 3. Electrochemical *C–V* profiles of epitaxial (a) GaAs and (b) AlGaAs layers grown on (*1*) monolithic and (*2*) porous GaAs substrates: (I) epitaxial film; (II) porous GaAs layer; (III) monolithic GaAs substrate.

and porous substrates possess a highly perfect single-crystalline structure. Figure 2 shows the rocking curves measured in the region of the GaAs(400) reflection for AlGaAs and InGaAs layers on both porous and monolithic substrates. Clearly distinguished are large peaks from the substrates and epitaxial layers, as well as side maxima due to the thickness contrast. The latter maxima are evidence of a coherent character of the crystal lattice across the layer and a uniform thickness of the layer over the area studied (0.2×0.5 mm^2). This is also confirmed by a small width of the rocking curves, which is close to the theoretical limit corresponding to a given film thickness.

A study of the distribution of In atoms in depth of the InGaAs layer by the method of SIMS profiling showed a considerable smearing of the In profile at the boundary between epitaxial layer and porous substrate, which was much more pronounced as compared to the interface between film and monolithic substrate. This difference can be explained by In atoms entering into pores in the initial growth stage.

We have also studied the structure of epitaxial layers by the method of electrochemical *C–V* profiling [5]. Figure 3 presents typical capacitance–voltage curves obtained at a frequency of 10 kHz. As seen from Fig. 3a (curve *1*), the epitaxial layer of GaAs on a monolithic GaAs substrate has a thickness of 0.5 μm and an electron concentration of 2×10^{16} cm^{-3}. The other part of the same sample, representing a GaAs film grown on the porous substrate, contains an epitaxial layer with approximately the same thickness (curve *2*, region I) and somewhat inhomogeneous electrical characteristics. This layer is followed by region II representing porous GaAs (with a thickness of 2.5 μm). This region is characterized by a high density of deep acceptorlike levels, also somewhat inhomogeneously distributed in depth. At a depth of about 3 μm, the curve exhibits the passage to the monolithic substrate (region III).

Similar results were obtained for undoped AlGaAs epitaxial layers grown on monolithic and porous GaAs substrates (Fig. 3b). A 1-μm-thick AlGaAs layer grown on the monolithic substrate (curve *1*) has a small concentration of charge carriers, which results in a complete depletion of this layer. The AlGaAs layer grown on the porous substrate apparently contains (similarly to the substrate) a rather large number of deep acceptorlike levels, as confirmed by the *C–V* profile measurements.

Thus, we have demonstrated that structurally perfect single-crystalline layers of GaAs, AlGaAs, and InGaAs with mirror-smooth surface can be obtained on porous GaAs substrates by metalorganic VPE technique. Differences in the properties of layers obtained under similar growth conditions on the porous and monolithic substrates are probably related to certain features of the structure and the surface state of porous GaAs, which may influence the mechanism and kinetics of epitaxy.

This work was supported by the Russian Foundation for Basic Research (project no. 98-02-16624) and the

Interinstitution Scientific-Technological Program "Physics of Solid-State Nanostructures."

REFERENCES

1. T. Unagami and S. J. Masashiro, J. Electrochem. Soc. **125**, 1339 (1979).
2. V. P. Bondarenko, N. N. Voronov, and V. V. Dikareva, Pis'ma Zh. Tekh. Fiz. **20**, 5 (1994) [Tech. Phys. Lett. **20**, 410 (1994)].
3. L. P. Belyakov, I. B. Zakharova, and T. I. Zubkova, Fiz. Tekh. Poluprovodn. (St. Petersburg) **31**, 93 (1997) [Semicond. **31**, 76 (1997)].
4. Yu. Buzynin, S. Gusev, Yu. Drozdov, *et al.*, *Proceedings of International Symposium ALT'95*, Proc. SPIE **2777**, 43 (1995).
5. I. V. Irin and A. V. Murel', Prib. Tekh. Éksp., No. 6, 150 (1993).

Translated by P. Pozdeev

Technical Physics Letters, Vol. 26, No. 4, 2000, pp. 302–304. Translated from Pis'ma v Zhurnal Tekhnicheskoĭ Fiziki, Vol. 26, No. 7, 2000, pp. 70–74.

Evaluation of Spectral Parameters for Second-Order Nonlinear Systems

V. A. Dvinskikh and S. V. Frolov

Chernyshevsky State University, Saratov, 410071 Russia

Received October 14, 1999

Abstract—A nonlinear conservative Lyapunov system is treated analytically and numerically. The results of the two approaches show satisfactory agreement. The spectra of forced oscillations in a related nonlinear system are examined. © *2000 MAIK "Nauka/Interperiodica".*

As is known, the discrete Fourier transform is insensitive to a small-scale structure of the spectrum [1]. The use of parametric methods of spectrum analysis based on the time-series models [2], requiring preliminary sample solutions, still does not allow one to distinguish closely spaced spectral components of a quasi-periodic oscillation. In this work, we have used an approach in which the sample sequence is approximated by a first-order trigonometric polynomial [3], which provided improved spectral resolution.

Consider the equation of a conservative nonlinear Lyapunov system,

$$\frac{d^2x}{dt^2} + x + x^3 = 0, \tag{1}$$

and change the independent variable as follows:

$$t \cong \tau(1 + h_2c^2 + h_4c^4 + \ldots), \tag{2}$$

where h_2, h_4, ... are constants to be computed. Substituting (2) into (1) yields

$$\frac{d^2x}{d\tau^2} + (x + x^3)(1 + h_2c^2 + h_4c^4 + \ldots) = 0. \tag{3}$$

Following [4], let us seek for a solution of (3) in the form

$$x(\tau) = c\cos\tau + c^3x_3(\tau) + c^5x_5(\tau) + \ldots, \tag{4}$$

where $x_3(\tau)$, $x_5(\tau)$, ... are periodic functions having period 2π and satisfying the initial conditions

$$x_3(0) = x_5(0) = \ldots = 0;\ \left.\frac{d_{x_3}}{d\tau}\right|_0 = \left.\frac{dx_5}{d\tau}\right|_0 = \ldots = 0. \tag{5}$$

Then

$$\frac{d^2x_3}{d\tau^2} + x_3 = \left(\frac{3}{4} - 2h_2\right)\cos\tau + \frac{1}{4}\cos3\tau. \tag{6}$$

The condition of periodicity implies that the coefficient at $\cos\tau$ is zero, so that

$$h_2 = 3/8. \tag{7}$$

The solution of (6) subject to (5) is

$$x_3(\tau) = \frac{1}{32}(\cos\tau - \cos3\tau). \tag{8}$$

The equation for $x_5(\tau)$ is

$$\frac{d^2x_5}{d\tau^2} + x_5 = \left(-2h_4 + \frac{57}{128}\right)\cos\tau + \frac{3}{16}\cos3\tau - \frac{3}{128}\cos5\tau, \tag{9}$$

which yields

$$h_4 = 57/256. \tag{10}$$

Restricting consideration to the above solutions, we arrive at

$$x(\tau) \cong x_1\cos\tau - x_3\cos3\tau - \frac{c^5}{1024}\cos5\tau, \tag{11}$$

where

$$x_1 = c + \frac{c^3}{32} + \frac{23c^5}{1024}, \quad x_3 = \frac{c^3}{32} - \frac{3c^5}{128}$$

with the period

$$T \cong 2\pi\left(1 - \frac{3c^2}{8} - \frac{57c^4}{254}\right). \tag{12}$$

Equation (1) was also solved numerically by a fourth-order Runge–Kutta method with the step size

1063-7850/00/2604-0302$20.00

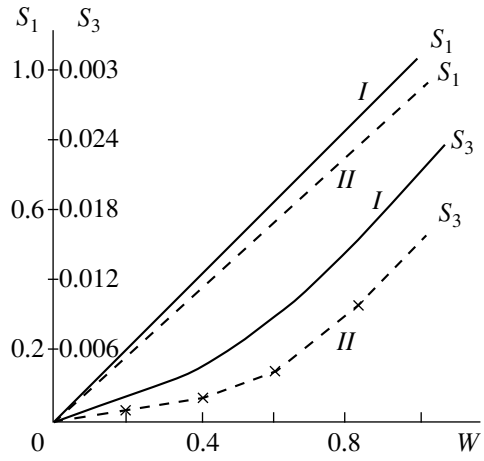

Fig. 1. Analytical and numerical solutions of the Lyapunov equation: the amplitudes of the first (S_1) and the third (S_3) harmonic vs. the initial parameter *W*. Lines *I* and *II* represent experiment and theory, respectively.

0.05 for several values of the initial condition *W*. Figure 1 shows the amplitudes of the first and the third harmonic as functions of *W*: the solid and the broken lines are obtained using the analytical and the numerical techniques, respectively. According to our evaluation, the experimental and theoretical results are also close to each other in terms of the period.

Furthermore, we studied the Feigenbaum equation [5]

$$\frac{d^2x}{dt^2} + \mu\frac{dx}{dt} + x^3 = b\sin t \qquad (13)$$

with constant parameters $\mu \ll 1$ and $b < 1$. Figure 2 shows the waveforms and the corresponding spectra. The time diagrams were computed for $b = 0.9$ and $\mu = 0.049$, 0.0491, or 0.0492. An analysis of these diagrams indicates the appearance of amplitude modulation due

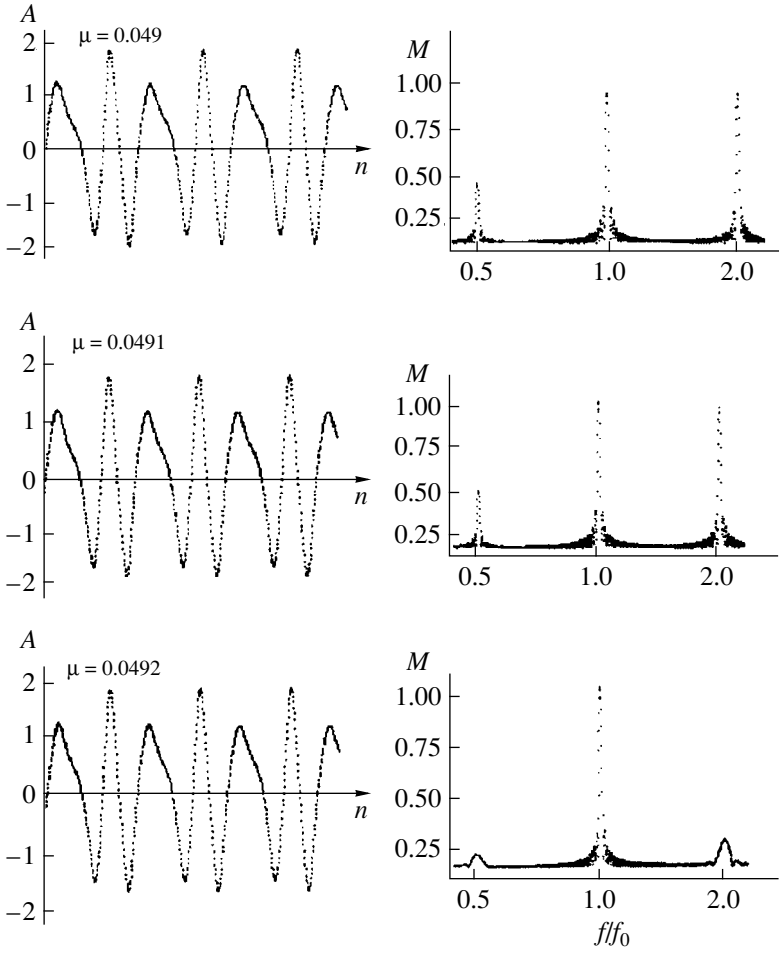

Fig. 2. Time diagrams representing solutions to the Feigenbaum equation (computed at $b = 0.9$ and different values of μ) (left) and the corresponding experimental spectra. *A* is the absolute value of amplitude, *n* is the number of a waveform sample, f/f_0 is the frequency of a spectral component, f_0 is the frequency of the external signal, and *M* is the modulus of spectral amplitude.

to instability in the transients. The modulation is manifested by side peaks with the heights decreasing with increasing μ. The left and the right neighboring peak stem from period doubling of the external signal or the induced second-harmonic, respectively.

REFERENCES

1. A. S. Dmitriev and V. Ya. Kislov, *Stochastic Oscillations in Radiophysics and Electronics* (Nauka, Moscow, 1989).
2. S. L. Marple, Jr., *Digital Spectral Analysis with Application* (Prentice-Hall, Englewood Cliffs, N.J., 1987; Mir, Moscow, 1989).
3. V. A. Dvinskikh, Zh. Tekh. Fiz. **62**, 168 (1992) [Sov. Phys. Tech. Phys. **62**, 1213 (1992)].
4. I. G. Malkin, *Some Problems in the Theory of Nonlinear Oscillations* (Gostekhizdat, Moscow, 1956).
5. M. I. Feigenbaum, Los Alamos Sci. **1**, 4 (1980).

Translated by A. A. Sharshakov

Technical Physics Letters, Vol. 26, No. 4, 2000, pp. 305–306. Translated from Pis'ma v Zhurnal Tekhnicheskoĭ Fiziki, Vol. 26, No. 7, 2000, pp. 75–79.

Hypersensitive Avalanche Photodiode with Surface Transport of Charge Carriers

Z. Ya. Sadygov, M. K. Suleĭmanov, and T. Yu. Bokova

Joint Institute for Nuclear Research, Dubna, Moscow oblast, Russia

Received October 14, 1999

Abstract—The principles of design and operation of a new avalanche photodiode structure are considered. The photodiode, comprises a silicon substrate, a semitransparent titanium gate separated from semiconductor by an insulating layer, and a drain electrode ensuring the surface transport of multiplicated charge carriers along the semiconductor—insulator interface. It is shown that multielement avalanche photodiode structures can be created, including charge-coupled-device matrices with the intrinsic photosignal gain above 10^4. © *2000 MAIK "Nauka/Interperiodica".*

A promising direction in the development of comparatively low-cost multichannel avalanche photodetectors is related to the use of silicon-based metal–insulator–semiconductor (MIS) [1, 2] and metal–resistive layer–semiconductor (MRS) [3, 4] structures with local stabilization of the avalanche process.

Previously [5, 6], we have proposed a new silicon-based avalanche photodiode structure implementing a more effective and technologically advantageous method of local stabilization of the avalanche process. Below we report for the first time on the principles of design and operation of the new device and present the main results of testing of an experimental sample of this avalanche photodiode.

Figure 1a shows a schematic diagram of the cross-section of the new avalanche photodiode. In a working regime, the titanium gate and the guard ring are operated under negative potentials providing development of the avalanche multiplication of charge carriers in the planar *p*–*n* junction amplifying the photocurrent. Upon the signal amplification, the charge carriers are transported along the Si–SiO_2 interface toward the guard ring (drain electrode). A special feature of operation of this photodiode consists in that the character of the avalanche process is determined by the surface conductivity of the Si–SiO_2 interface. The thickness of a *p*-type semiconductor layer and the concentration of impurities in this layer are selected so as to provide that the depletion region would reach the Si–SiO_2 interface at a working potential on the photodetector (Fig. 1b). In this case, the Si–SiO_2 interface features an ultrathin (~10 nm thick) *p*-type layer with a resistance determined by the gate potential. It is the surface resistance of this ultrathin layer that determines the efficiency of local stabilization of the avalanche process.

During the development of the avalanche process initiated by a single electron, the main part of generated holes is accumulated within a small region at the Si–SiO_2 interface. A characteristic size of this region is comparable to the thickness of the depletion region formed at the planar *p*–*n* junction (~3 μm). This leads to a local decrease in the electric field strength within the corresponding region of the *p*–*n* junction, which provides stabilization of the avalanche rate. The photo-

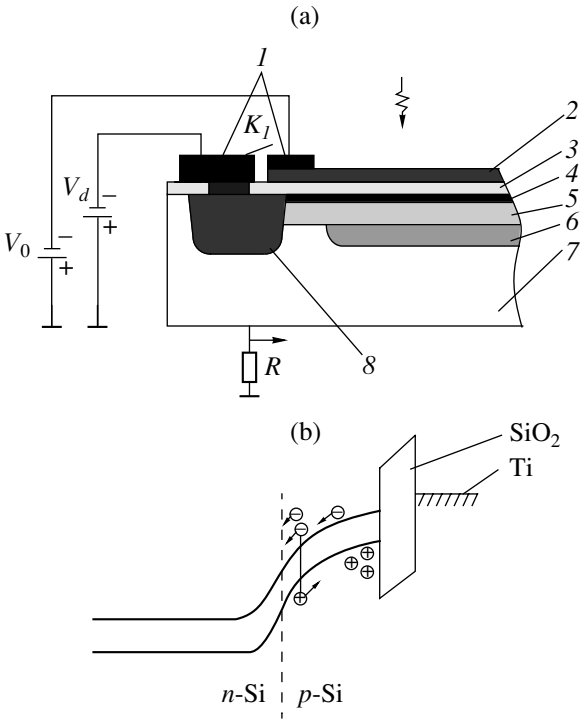

Fig. 1. Schematic diagrams showing (a) the cross-section and (b) the energy band diagram of the new avalanche photodiode: (*1*) aluminum contacts; (*2*) semitransparent titanium gate electrode; (*3*) silicon dioxide; (*4*) *p*-type layer ensuring the surface transport of multiplicated charge carriers; (*5*) *p*-type silicon layer; (*6*) *n*-type silicon layer with the impurity concentration increased relative to substrate; (*7*) *n*-type silicon substrate; (*8*) guard ring.

1063-7850/00/2604-0305$20.00 © 2000 MAIK "Nauka/Interperiodica"

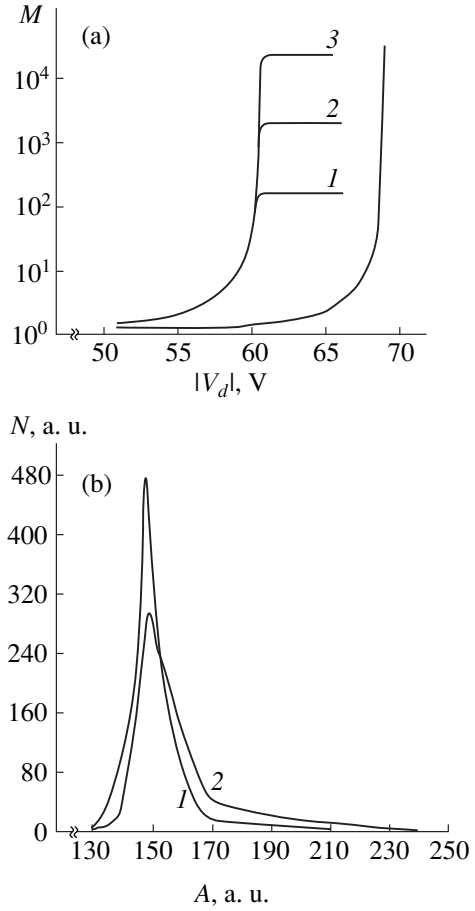

Fig. 2. Results of experimental testing of the new avalanche photodiode: (a) plots of the photocurrent gain M versus the drain potential V_d for V_g = –68.5 (*1*), –69.0 (*2*), and –69.5 V (*3*) and $V_g = V_d$ (*4*) (K_1 switch in Fig. 1 closed); (b) the output pulse amplitude distribution (*1*) in the dark and (*2*) under illumination with light pulses containing on the average one photon per pulse.

response signal is formed as the bias current in the insulator capacitance.

Figure 2a shows the plots of the pulsed photocurrent gain M versus the voltage V_d applied to the drain electrode of an experimental avalanche photodiode sample, measured at various values of the titanium gate potential V_g. The working area of the sample had a diameter of ~1 mm. The test results showed that the M versus V_d plots measured at a fixed titanium gate potential always exhibit saturation. This effect is related to the conductivity cutoff at the Si–SiO_2 boundary, which leads to limitation of the drain current in the photodiode. However, the pulsed luminance–current characteristic of the photodiode still remains linear because of a low capacitive impedance of the gate insulator.

The presence of a saturation region in the M versus V_d curve suggests a unique possibility of using the proposed device structure for creating multielement avalanche photodiode structures characterized by a high spatial gain homogeneity.

Figure 2b shows the output pulse amplitude distribution of the avalanche photodiode operated at $V_d = V_g$ = –69 V (K_1 switch in Fig. 1 closed). The measurements were performed in the signal lock-in mode at a window width of ~100 ns. The light source was represented by a light-emitting diode (LED) emitting at a wavelength of ~480 nm. The light pulse duration did not exceed 70 ns. The number of photons in the LED pulse was determined using a FEU-130 multiplier phototube.

Curve *1* in Fig. 2b shows a distribution of the output pulses initiated by dark electrons in the avalanche photodiode studied. The average interval between the dark pulses was ~200 ns. Curve *2* was measured under conditions of the avalanche photodiode illumination with light pulses containing on the average one photon per pulse. As seen, assuming the lower detection threshold to be equal to the pulse amplitude in the 155th channel, the probability of detecting single-photon light pulses reaches a level of ~25%. Note that the probability of single photon detection using FEU-130 did not exceed ~15%.

There is another regime of operation of the proposed avalanche photodiode. As is seen from Fig. 1, the design and principle of operation of the avalanche photodiode is essentially a prototype of the new charge-coupled device (CCD) with intrinsic photosignal amplification. Using three-phase pulsed supply voltages (e.g., V_g = –69.5, –55, and –45 V at V_d = –63 V = const) for the titanium gate, we have succeeded in detecting, recording, and transmitting photosignals induced by single photoelectrons. This is possible due to the intrinsic photosignal gain exceeding 10^4 at the moment of application of a pulsed voltage with the amplitude V_g = –69.5 V to the titanium gate.

Thus, we have designed, constructed, and tested a new silicon-based avalanche photodiode capable of detecting single light quanta at room temperature. It was demonstrated that multielement hypersensitive photodetectors can be created based on the new device, including CCD matrices with a high spatial homogeneity of the working characteristics.

REFERENCES

1. N. N. Gol'braĭkh, A. F. Plotnikov, and V. É. Shubin, Kvant. Élektron. (Moscow) **2**, 2624 (1975).
2. A. Ya. Vul', A. E. Dideĭkin, and A. I. Kosarev, Pis'ma Zh. Tekh. Fiz. **16**, 15 (1990).
3. A. G. Gasanov, Z. Ya. Sadygov, *et al.*, Pis'ma Zh. Tekh. Fiz. **14**, 706 (1988) [Sov. Tech. Phys. Lett. **14**, 313 (1988)].
4. Z. Y. Sadygov *et al.*, IEEE Trans. Nucl. Sci. **43**, 1009 (1996).
5. Z. Ya. Sadygov, RF Patent No. 2086047 (30 May 1996).
6. Z. Ya. Sadygov, Doctoral Dissertation in Mathematical Physics (Moscow, 1997).

Translated by P. Pozdeev

Technical Physics Letters, Vol. 26, No. 4, 2000, pp. 307–310. Translated from Pis'ma v Zhurnal Tekhnicheskoĭ Fiziki, Vol. 26, No. 7, 2000, pp. 80–86.

Oscillation of the Mirror and Fractional RHEED Reflections during Homoepitaxy on the (2 × 4)-Reconstructed GaAs(001) Surface

Yu. G. Galitsyn, S. P. Moshchenko, A. I. Toropov, and A. K. Bakarov

Institute of Semiconductor Physics, Siberian Division, Russian Academy of Sciences, 630090 Novosibirsk, Russia

Received October 22, 1998

Abstract—Oscillations of the intensity of mirror and fractional RHEED reflections during homoepitaxy on the GaAs(001)–(2 × 4) reconstructed surface were studied. A considerable difference was observed in the patterns of intensity variation for the mirror and the fractional (0 1/4) and (0 3/4) reflections corresponding to the α and β phases on the reconstructed surface. A kinetic scheme of elementary processes occurring on the Ga(001) surface upon the homoepitaxial growth initiation is proposed. The activation energy for the nucleation process was experimentally determined (5-eV). It is shown that the temperature dependence of the probability of critical nucleus formation is determined by the desorption of As_2 dimers. © *2000 MAIK "Nauka/Interperiodica".*

A kinetic model describing the build-in of As_4 particles into the lattice sites in the course of the homoepitaxial growth process on the GaAs(001)–(4 × 2) reconstructed surface has been developed and studied in much detail [1–8]. It was established that a considerable role in the epitaxial growth belongs to processes such as the adsorption and desorption of As_4 tetramers, desorption of As_2 dimers, and the bimolecular interaction of two tetramers. The same processes must undoubtedly take place during epitaxial growth on the As-stabilized (2 × 4)-reconstructed surface. However, elucidation of the role of these processes in the surface reconstruction was hindered by the circumstance that the growth rate was controlled only by the supply of gallium. For this reason, the period of oscillations in the mirror reflection intensity measured by high-energy electron diffraction in the reflection mode (RHEED) was independent of the As_4 pressure and the surface temperature within rather broad limits of variation of these parameters.

Nevertheless, some important results were obtained during investigation of the elementary growth process on the (2 × 4)-reconstructed surface (see [9] and references therein). Analysis of the two-dimensional nucleation on the GaAs(001) surface featuring the β-(2 × 4) reconstruction led to a conclusion that the appearance of two-dimensional GaAs islands was initiated by pair interactions between Ga adatoms in the so-called "missing dimer trenches" of the ideal β-(2 × 4) structure. It was ascertained that filling of the trenches proceeds by build-in of the pairs of Ga adatoms as a result of the second-order reaction of dissociative As_4 chemisorption (that is, a bimolecular reaction between two As_4 particles) [9].

However, a real structure of the β-(2 × 4) phase, which is the most ordered phase of the family of As-stabilized (2 × 4) reconstructions (including α, β, and γ), is by no means ideal [10, 11]. In our opinion, the β-(2 × 4) reconstruction can be considered not only as a system of "missing arsenic dimer trenches." An alternative model represents periodically arranged chains of arsenic dimers elongated in the same direction $[\bar{1}10]$ as the trenches [9–12]. Examination of the images of this structure obtained by scanning tunneling microscopy (STM) indicates that the most characteristic type of defects in this phase appears as missing chain units (vacancies). As a result, the average length of the undamaged dimer chain is determined by an average statistical concentration of these vacancies $N(T)$. The average chain length may vary from 50 to 300 Å. We may define a long-range order parameter as $\eta(T) = N_0/N(T)$, where N_0 is the minimum thermodynamically equilibrium concentration of vacancies in the region of existence of the β phase. This parameter directly describes the intensity both of the fractional reflections due to the β-(2 × 4) phase observed in the azimuthal direction $[\bar{1}10]$ and of the mirror-reflected beam.

An analysis of the pattern of oscillations of the intensity of mirror and fractional reflections, with an allowance for a real structure of the β-(2 × 4) phase allowed us to suggest a model describing two-dimensional nucleation during the homoepitaxial growth from As_4 and Ga flows, which is somewhat different from the scheme adopted in [9].

The experiments were performed in a Riber MBE-32 commercial molecular beam epitaxy system using the samples with an area of 3 × 3 mm. Oscillations in the

1063-7850/00/2604-0307$20.00

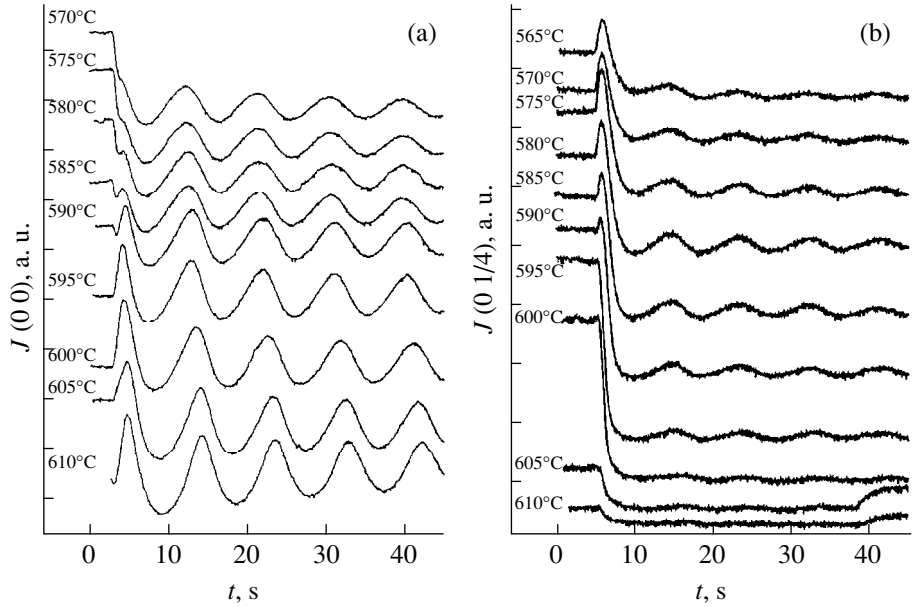

Fig. 1. Oscillations in the intensity J of (a) the mirror (0 0) and (b) the fractional (0 1/4) reflections observed at various temperatures. As the temperature increases, the first oscillation of the mirror reflection changes from decrease to increase, while the fractional reflection exhibits the opposite trend.

intensity of the mirror-reflected beam (0 0) and the fractional reflections (0 1/4), (0 3/4), and (0 2/4) were measured at a glancing incidence angle of ~1.5° in the azimuthal direction $[\bar{1}10]$ and determined for an ~1 mm^2 area on the diffractometer screen. The measurements were performed in the temperature interval 560–620°C corresponding to the region of existence of α- and β-(2 × 4) reconstructions at $P(As_4) = 2 \times 10^{-6}$ Torr.

Figure 1 shows the pattern of oscillations observed for the mirror and the fractional (0 1/4) reflections during the growth initiated in the temperature interval 610–570°C corresponding to a transition from high-temperature α-(2 × 4) phase to the low-temperature β-(2 × 4) ordered reconstruction. As the β phase begins to grow, the mirror reflection intensity decreases, while intensity of the fractional reflections (0 1/4) and (0 3/4) increases. In contrast, in the range of temperatures (T_s > 590°C) corresponding to existence of the α phase, the mirror reflection intensity exhibits rapid initial growth, while intensities of the fractional reflections drop. As is seen from Fig. 1, the period of the first oscillation increases with the temperature. Indeed, the first oscillation period at T_s = 575°C virtually coincides with the periods of subsequent oscillations, while the value observed at T_s = 610°C increases by 20%. Note that the shape of oscillations also changes with increasing substrate temperature: from sinusoidal for the β phase to cups-like for the α phase. This variation of the shape of oscillations is evidence of a considerable increase in the diffusion mobility of adatoms with the temperature [13, 14].

Let us consider the behavior of reflection intensity oscillations for the β phase in more detail. An increase in intensity of the (0 1/4) beam upon the growth initiation must be associated with increasing degree of ordering of the β phase. We believe that a dominating process in the initial growth stage is the trapping of gallium adatoms by vacancies. In fact, this is equivalent to "linking" of the separate segments of dimer chains. As a result, the average chain length increases and, hence, the intensity of the fractional beams (0 1/4) and (0 3/4) grows. At the same time, the mirror reflection intensity must significantly decrease because the total electron flux is conserved. Indeed, the experiment (Figs. 1 and 2a) shows that the reflection intensity variations are related to initiation of the β phase growth. The appearance of two-dimensional nuclei on the surface leads to a sharp decrease in the stationary concentration of adatoms. Under these conditions, the equilibrium value of the long-range order parameter $\eta(T)$ restores and the (1 1/4) fractional reflection intensity returns to the initial value I_0. This conclusion was confirmed by an additional experiment: interrupt in the flow of Ga atoms at the maximum intensity (I_m) results in the rapid $I_m \longrightarrow I_m$ relaxation (Fig. 2c).

A different pattern of growth initiation was observed for the α phase. This phase has a less ordered structure and the trenches of missing dimers in this phase are filled with gallium atoms. Indeed, the STM data show evidence for the appearance of local disordered structures of the (1 × 2) type containing excess gallium [10, 15]. In the (1 × 2) phase, the surface gallium atoms do not form dimers and are only bound to two arsenic atoms in the underlying atomic plane.

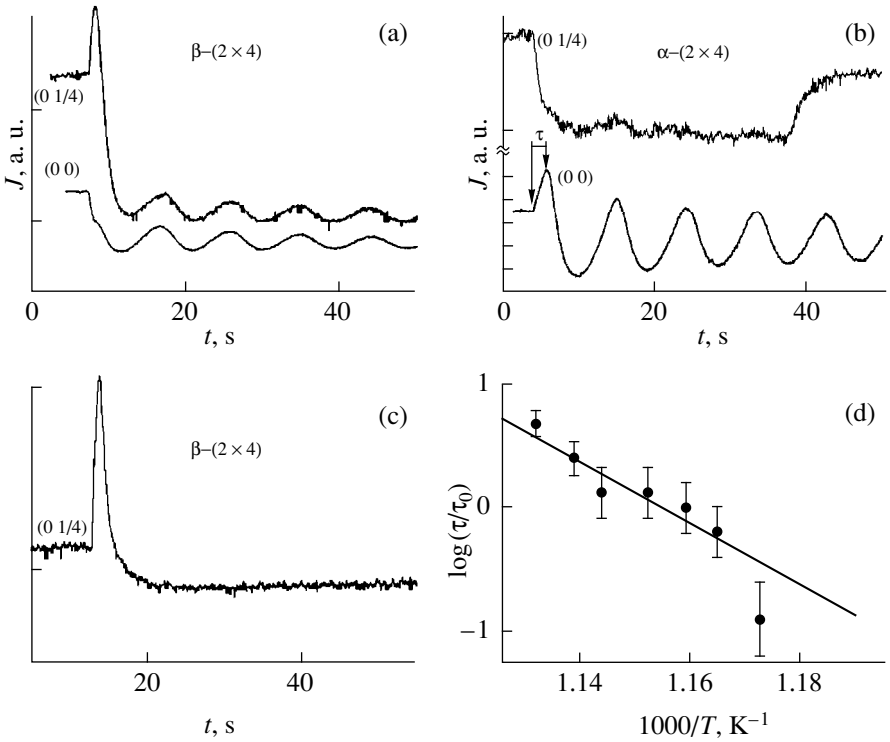

Fig. 2. Oscillations in the intensity J of fractional reflections during the growth initiated in various phases: (a) β-(2 × 4) (T = 575°C); (b) α-(2 × 4) (T = 605°C); (c) relaxation of the (1 1/4) reflection intensity upon interrupt (indicated by an arrow) in the flow of Ga atoms; (d) the Arrhenius plot of the duration of the growth initiation stage τ (normalized to 1 s) versus reciprocal temperature.

Therefore, Ga adatoms may directly form regions representing the aforementioned disordered phase. Upon the growth initiation in this system, the surface disorder would increase further. As a result, intensity of the (0 1/4) and (0 3/4) beams must decrease, while that of the mirror reflected beam must increase (provided that the diffraction scattering process dominates)—in agreement with experiment (Fig. 2b).

. For the α phase growth, the duration of the induction period τ for the formation of two-dimensional nuclei becomes a measurable quantity. Assuming that the formation of a critical two-dimensional nucleus requires a pair of arsenic dimers, which may form as a result of a bimolecular interaction between two As_4 particles, we obtain

$$\tau \sim f(n)/\Theta_{As}^2,$$

where Θ_{As} is the degree of surface coverage by arsenic dimers, $f(n)$ is a function of the Ga adatom concentration, which also weakly depends on the temperature. As demonstrated previously [7, 8], the temperature variation of Θ_{As} is obeys the relationship

$$\Theta_{As} \sim k_1 P/k_5(T),$$

where k_1 is the As_4 adsorption constant, P is the As_4 pressure, and k_5 is the coefficient of desorption of arsenic dimers from the surface (the desorption activation energy is 2.5 eV [16]. Therefore, the Arrhenius plot of τ must be approximated by a straight line with a slope corresponding to $E_{eff} = 2E_5 \sim 5$ eV. This conclusion agrees with experiment (Fig. 2d).

Thus, the experimental data obtained on the initial growth stages for the α and β phases show evidence that these processes have significantly different dynamics. For the ordered β phase, the initial supply of components leads first to additional surface ordering. In contrast, the initiation of growth on the disordered α phase results in increasing disorder.

Thus, analysis of the pattern of oscillations in the intensity of mirror and fractional reflections, with an allowance for a real structure of the (2 × 4)-reconstructed GaAs(001) surface, allows us to ascertain that epitaxial growth in the β-phase begins with restoration of the missing units in arsenic dimer chains, rather than with filling the missing dimer trenches as was suggested in [9]. In the α phase, the growth initiation leads to the formation of arsenic-deficient disordered phases.

Duration of the nucleation stage increases with the temperature. According to the model proposed, the desorption of arsenic dimers plays a dominating role in the temperature dependence of the nucleation rate.

This work was supported by the Russian Foundation for Basic Research, project no. 96-03-33916a.

REFERENCES

1. E. S. Tok, J. H. Neave, J. Zhang, *et al.*, Surf. Sci. **374**, 397 (1997).
2. C. T. Foxon and B. A. Joyce, Surf. Sci. **50**, 434 (1975).
3. J. C. García, C. Neri, and J. Massies, J. Cryst. Growth **98**, 1 (1989).
4. A. K. Ott, S. M. Casey, A. L. Alstrin, and S. R. Leone, J. Vac. Sci. Technol. B **14**, 2742 (1996).
5. Yu. G. Galitsyn, V. G. Mansurov, and I. I. Marahovka, Phys. Low-Dimens. Semicond. Struct. **5**, 75 (1997).
6. Yu. G. Galitsyn, V. G. Mansurov, and I. I. Marahovka, Phys. Low-Dimens. Semicond. Struct. **7**, 55 (1997).
7. Yu. G. Galitsyn, I. I. Marakhovka, S. P. Moshchenko, and V. G. Mansurov, Pis'ma Zh. Tekh. Fiz. **24**, 31 (1998) [Tech. Phys. Lett. **24**, 260 (1998)].
8. Yu. G. Galitsyn, I. I. Marakhovka, S. P. Moshchenko, *et al.*, Dokl. Akad. Nauk SSSR **359**, 48 (1998) [Dokl. Phys. **42**, 25 (1998)].
9. A. R. Avery, H. T. Dobbs, D. M. Holms, *et al.*, Phys. Rev. Lett. **79**, 3938 (1997).
10. Q. Xue, T. Hashizume, A. Ichimiya, *et al.*, Sci. Rep. Res. Inst. Tohoku Univ. A **44**, 113 (1997).
11. T. Hashizume, Q. Xue, J. Zhou, *et al.*, Phys. Rev. Lett. **73**, 2208 (1994).
12. A. R. Avery, D. M. Holms, J. Sudijono, *et al.*, Surf. Sci. **323**, 91 (1995).
13. L. M. Peng and M. Whelan, Proc. Roy. Soc. London **432**, 195 (1991).
14. A. K. Myers Beaghton and D. D. Vvedensky, Surf. Sci. **232**, 161 (1990).
15. J. Behrend, M. Wassermeier, and K. H. Ploog, Surf. Sci. **372**, 307 (1997).
16. C. Sasaoka, Y. Kato, and A. Usui, Appl. Phys. Lett. **62**, 2338 (1993).

Translated by P. Pozdeev

Technical Physics Letters, Vol. 26, No. 4, 2000, pp. 311–314. Translated from Pis'ma v Zhurnal Tekhnicheskoĭ Fiziki, Vol. 26, No. 7, 2000, pp. 87–94.

Laser-Induced Surface Decomposition of Al_2O_3 Excited in the V-center Absorption Band

A. A. Lisachenko and A. A. Glebovskiĭ

Institute of Physics, St. Petersburg State University, St. Petersburg, Russia

Received November 3, 1999

Abstract—The primary products of desorption from Al_2O_3 surface excited by laser pulses (pulse duration $\tau \sim$ 15 ns; wavelength λ = 354 nm, radiant power density $P/S < 10^8$ W/cm^2) in the V-center absorption band were studied by the time-of-flight (TOF) spectroscopy. The TOF spectra show evidence of the desorption of one "cold" (T_1 = 300 K) and two "hot" (T_2 = 1000 K, T_3 = 4300 K) groups of oxygen molecules with the Maxwell velocity distributions, as well as of the hot Al and O atoms with nonequilibrium energy distributions (E_1 = 0.37 eV, E_2 = 0.38 eV). A model describing the oxygen desorption as initiated by the electron transitions is suggested, in which escape of the cold O_2 molecules from the surface is related to discharge of the O_2^- anions adsorbed on the V-centers, desorption of the hot atoms is attributed to discharge of the surface O^- anions, and the appearance of the hot O_2 molecules is related to the associative desorption of two O^- anions localized at the same V-center discharged by a pair of excitons. © *2000 MAIK "Nauka/Interperiodica"*.

The phenomena of spectral-selective laser-induced adsorption, desorption, and surface chemical reactions find increasing application for the development of methods of the surface diagnostics and directed modification of the physicochemical properties of solid surfaces. Oxides are frequently used as the base materials in various technologies, because substances of this class may exhibit the properties of insulators, wide- and narrow-bandgap semiconductors, metals, and high-temperature superconductors. The properties of an oxide surface are highly sensitive to the oxygen content, which can be changed using the oxygen photoadsorption or photodesorption effects [1]. These effects give rise to special surface structures usually not observed in the same oxide system upon thermal activation [2]. The oxide photoactivation mechanisms are qualitatively different for irradiation in the regions of intrinsic and impurity absorption [3]. Activation in the spectral region of the electronic absorption of impurities at low irradiation intensities (~10^{-2} – 10^{-3} W/cm^2) may lead to coexistence of the spectral-selective effects having opposite trends [2]. For example, photoactivation of the O_2–Al_2O_3 system in the absorption band of the F^+-centers (an oxygen vacancy trapping one electron) is accompanied by the photoadsorption of oxygen and occupation of the oxygen vacancies. In contrast, activation of the V-centers (Al vacancy trapping one or two holes) leads to the photodesorption of oxygen. The photodesorption of sodium adatoms from Al_2O_3 as a result of their resonance photoactivation was reported in [4].

The photodesorption phenomena can be effectively studied by the method of time-of-flight (TOF) spectroscopy. The TOF analysis of primary products of the laser-induced desorption [5] provides data on the dynamics of energy exchange between the electron and atomic subsystems and the kinetics of subsequent rearrangement of chemical bonds on the irradiated surface.

In this work, we have studied the primary products of oxygen desorption from the Al_2O_3 surface as a result of its electronic excitation in the absorption band of V-centers. The purpose was to elucidate the mechanisms of the excitation energy transfer from electronic to atomic subsystem and the dynamics of bond rupture. We have also analyzed the possibility of oxide degradation during the irradiation at $P/S < 10^8$ W/cm^2, that is, in the early stages (~10^{-5} monolayer) not detected by optical and electron spectroscopy techniques.

EXPERIMENTAL

The experiments were performed using a mass-spectrometric setup described previously [3]. A sample was placed into an ultrahigh vacuum chamber ($p \sim 2 \times 10^{-10}$ Torr) of the TOF spectrometer at a distance of l = 78 mm from the ion source and irradiated with the third harmonic of a pulsed neodymium laser ($\tau \sim$ 15 ns, λ = 354 nm, $P \le$ 65 kW). The emitted particles distributed over the flight distance l with respect to their velocities (i.e., kinetic energies). The TOF spectrometer determined the composition and amount of particles every 10 μs. The automated data acquisition system allowed any four components in the range 2 amu $\le m/e \le$ 100 amu to be separated and provided up to 50 values of their concentrations in the ion source determined with a period of 10 μs. Using these values, a TOF spec-

1063-7850/00/2604-0311$20.00

trum was constructed using a method proposed in [5]. A large aperture of the TOF spectrometer ($D/l = 22/78$) allowed the TOF spectra even from a single pulse to be obtained and normalized with respect to the P/S ratio. The sensitivity with respect to molecular oxygen was ~10^{-6} monolayer for an irradiated surface area of 1 mm^2. Typical results obtained from a disperse γ-Al_2O_3 surface were confirmed by control experiments using smooth α-Al_2O_3 samples (sapphire).

EXPERIMENTAL RESULTS

Figure 1 shows typical TOF spectra obtained from disperse samples. The laser-induced effects were studied in the range of radiant power densities P/S from 5 to 45 MW/cm^2. The lower threshold is determined by sensitivity of the system, and the upper limit, by the onset of charged particle emission. There is a clear evolution in the shape of the TOF spectra both with the P/S ratio (cf. curves *1–3*) and with the total exposure (cf. curves *3* and *4*). For $P/S \le 7$ MW/cm^2, the spectrum exhibits a typical unimodal distribution (curve *1*) described by the Maxwell function with $T_1 = 300$ K. The T_1 value does not vary with increasing P/S, but a second maximum appears at $P/S > 7$ MW/cm^2. The bimodal TOF spectrum can be modeled by merely adding the second distribution with $T_2 = 1000$ K to the first one. As the P/S ratio grows further, the intensity of the "hot" mode increases more rapidly than that of the "cold" mode and eventually the TOF spectrum fails to obey the bimodal distribution. Here, the TOF spectrum was more accurately separated into components using the following method. Taking into account that an instantaneous concentration of particles δN_i in the ion source (provided their Maxwell distribution) can be expressed as $\delta N_i \approx E^{3/2}\exp\left(-\frac{E}{kT}\right)$, the TOF spectrum can be linearized in the coordinates of $\ln(E^{-3/2}\delta N_i)$ versus E with a slope of $-\frac{1}{kT}$. The procedure of separating an experimental TOF spectrum into components was initiated at the high-energy wing. A linear portion of the spectrum plotted in the above coordinates was used to construct the corresponding Maxwell distribution. This component was subtracted from the initial TOF spectrum. Then the procedure was repeated with the difference spectrum, this process being continued unless a sum of the separated Maxwell components reproduced the experimental spectrum to within an error not exceeding the uncertainty of measurements. It should be noted that all real experimental curves could be modeled by a combination of three Maxwell distributions with $T_1 = 300$ K, $T_2 = 1000$ K, and $T_3 = 4300$ K (Fig. 2). As the P/S ratio increases, the relative intensities of the three components may vary, but the values T_1, T_2, and T_3 remain unchanged.

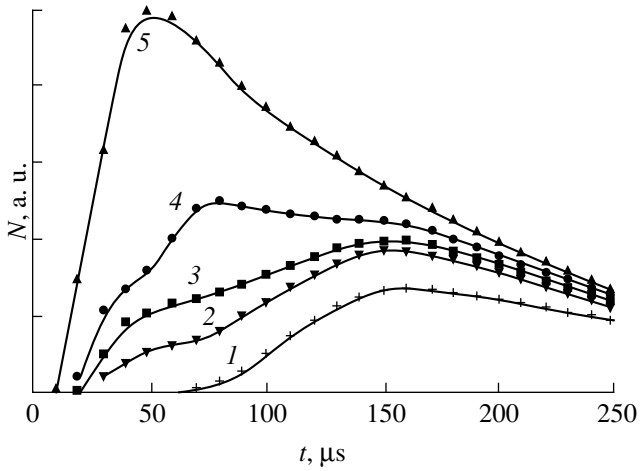

Fig. 1. TOF spectra of molecular oxygen desorbed from Al_2O_3 laser-irradiated at $P/S = 6.5$ (*1*); 10 (*2*); 16 (*3*); 28 (*4*); and 42 MW/cm^2 (*5*).

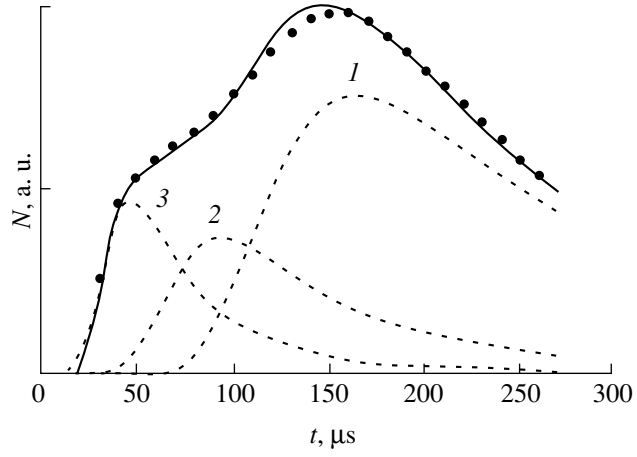

Fig. 2. An experimental TOF spectrum (Fig. 1, curve *3*) modeled by a sum of three Maxwell components with $T_1 = 300$ K (*1*), $T_2 = 1000$ K (*2*), and $T_3 = 4300$ K (*3*).

For a fixed P/S, the shape of the TOF spectrum varies with increasing number of laser pulses focused at the same spot on the sample surface. The effect has opposite trends for the cold and hot particles. The number of cold molecules decreases from pulse to pulse, which can be explained by decreasing concentration of the adsorbed species. In contrast, the number of hot O_2 molecules increases (with the constant T_1, T_2, and T_3 values). The appearance of hot molecules is accompanied by the escape of O and Al atoms from the surface. The TOF spectra of these atoms cannot be described by the Maxwell distribution functions. For this reason, the curves were characterized by determining the most probably kinetic energies E_k corresponding to the peaks, which gave the values 0.38 ± 0.05 eV and 0.37 ± 0.05 eV for the hot O and Al atoms, respectively. The experiments showed that the most probable kinetic

energies remain unchanged within a wide range of P/S values, from the desorption threshold of neutral particles to the limit of charged particle emission. This result allows us to consider the appearance of O and Al atoms as evidence of the onset of degradation of the sample surface. The pattern of variation of the TOF spectrum from pulse to pulse is independent of the interval between pulses in the range from 10^{-2} s to 10 h. This fact indicates that the observed phenomenon is related to the formation of additional defects in the Al_2O_3 structure, with the healing time under the experimental conditions studied exceeding 10 h at $T = 300$ K.

DISCUSSION OF RESULTS

Let us separately consider the regimes of "soft" and "hard" action in more detail. Desorption of the cold O_2 molecules can be quite adequately described using a model proposed for the low excitation level ($P/S \sim 10^{-3}$ W/cm^2) [2]. According to this model, the oxygen molecules adsorbed on the V-type centers escape from surface to the gas phase as a result of localization of a photogenerated hole on the V-center. The desorption event involves a precursor state in which the molecule gives an excess energy to the solid and leaves the solid surface with a kinetic energy corresponding to the surface temperature. The decrease in intensity from pulse to pulse is related to a decrease in the amount of adsorbed oxygen.

The laser-induced desorption of the hot oxygen atoms and molecules from oxides excited in the region of intrinsic absorption was reported previously [3]. According to the model proposed in [3], a hot molecule is desorbed as a result of the discharge of two neighboring surface O^- anions. Since an equilibrium distance from the surface to charged particle is smaller than that to a neutral one, the latter occurs on the repulsion branch of a potential curve of the particle–surface interaction. It is a potential interaction energy that converts into the kinetic energy of a desorbed particle leaving the surface (desorption initiated by electron transitions). The condition necessary for this process is a sufficiently high concentration of the charge carriers of both signs, including holes (to provide for the quadratic concentration effect dominating over the linear effect) and electrons (screening the repulsion of holes localized on the neighboring anions). However, this mechanism, underlying the model of "cold plasma annealing" [6, 7], is realized only for the carrier concentrations exceeding $\sim 10^{20}$ cm^{-3}, not reached under the experimental conditions studied in this work.

However, the hot particles can be observed, provided that the hole coupling may take place, even at moderate laser radiation intensities in the region of extrinsic (impurity) absorption of an oxide studied. Indeed, it was reported [8, 9] that the distribution temperature of O_2 molecules desorbed from single-crystal high-temperature superconductors $YBa_2Cu_3O_{7-x}$ and $Bi_2Sr_2CaCu_2O_8$ decreased down to the temperature of transition into the superconducting state ($T_s \approx 90$–92 K). However, on further cooling the samples, the kinetic temperature of O_2 molecules exhibited a jumplike increase from $T_k \approx T_s$ to ≈ 3000 K for $YBa_2Cu_3O_{7-x}$ and to ≈ 4000 K for $Bi_2Sr_2CaCu_2O_8$. This effect was explained by the appearance of hole pairs capable of discharging the neighboring O^- anions. This discharge is just what leads to the escape of hot molecules from the oxide surface.

In this context, of special interest are the results reported in [10, 11], where it was demonstrated that the absorption of radiation by structural defects may give rise to the formation of coupled excitons even at moderate ($\sim 10^{15}$ cm^{-3}) excitation levels. The maximum energy gain is achieved when a hole pair is localized at a cationic defect and is spaced from electrons by a distance intermediate between the Frenkel and Wannier–Mott exciton radii. In this case, a model describing the formation of the hot O_2 molecules [3, 9] can be extended to the results obtained in this work. The presence of two hot particle modes corresponding to $T_2 = 1000$ K and $T_3 = 4300$ K is related to the fact that the cationic vacancies (and, hence, the V-centers) in Al_2O_3 have two coordinations (tetrahedral and octahedral).

CONCLUSION

The laser irradiation of Al_2O_3 in the V-center absorption band at a radiant power density $P/S < 10^8$ W/cm^2 leads to the desorption of O_2 molecules proceeding by two mechanisms. According to the first mechanism, which accounts for the desorption of cold molecules with a kinetic temperature close to T_s, the escape of O_2 molecule from a V-center is related to localization of a single hole at the same defect. The second mechanism accounts for the appearance of two groups of hot molecules ($T_2 = 1000$ K, $T_3 = 4300$ K) as a result of the discharge and associative desorption of two surface O^- anions localized in the first coordination sphere of a cationic vacancy. The kinetic energy of desorbed molecules is gained from the potential energy of discharged O^- anions occurring on the repulsion branch of the particle–surface interaction potential curve (desorption initiated by electron transitions).

This work was supported by the State Program "Current Directions in the Physics of Condensed Media. Surface Atomic Structures" (project no. 3.3.99) and the Russian Foundation for Basic Research (project no. 99-02-16779).

REFERENCES

1. A. M. Aprelev, P. O. Artamonov, and A. A. Lisachenko, Phys. Low-Dimens. Semicond. Struct. **1**, 79 (1995).

2. A. O. Klimovskiĭ, T. K. Krutitskaja, A. A. Lisachenko, and I. M. Prudnikov, Phys. Low-Dimens. Semicond. Struct. **3**/**4**, 167 (1998).
3. I. F. Moiseenko and A. A. Lisachenko, Mater. Res. Soc. Symp. Proc. (Laser Ablation for Material Synthesis) **191**, 1 (1990).
4. A. M. Bonch-Bruevich, V. V. Khromov, S. G. Przhibelskiĭ, and T. A. Vartanyan, Phys. Low-Dimens. Semicond. Struct. **1**/**2**, 189 (1999).
5. A. A. Lisachenko, Lazer. Fiz. (Leningrad), No. 3, 66 (1992).
6. I. A. van Vechten, J. Phys. **44** (C5), 11 (1983).
7. M. Wautelet, Surf. Sci. **133**, L437 (1983).
8. P. O. Artamonov and A. A. Lisachenko, Pis'ma Zh. Tekh. Fiz. **18**, 53 (1992) [Sov. Tech. Phys. Lett. **18**, 671 (1992)].
9. P. O. Artamonov and A. A. Lisachenko, Sverkhprovod.: Fiz. Khim. Tekh. **6**, 121 (1993).
10. I. Singh and N. Iton, Appl. Phys. **A51**, 427 (1990).
11. K. Hattori, A. Okano, Y. Nakai, *et al.*, Phys. Rev. B **45**, 8424 (1992).

Translated by P. Pozdeev

Technical Physics Letters, Vol. 26, No. 4, 2000, pp. 315–317. Translated from Pis'ma v Zhurnal Tekhnicheskoĭ Fiziki, Vol. 26, No. 8, 2000, pp. 1–7.

High-Power Pumping Wave Influence on the Volume Spin Wave Propagation in a Ferrite Film

Yu. K. Fetisov

Moscow State Institute of Radio Engineering, Electronics, and Automation (Technical University), Moscow, 117454 Russia

Received November 22, 1999

Abstract—The influence of a high-power pumping wave on the propagation of backward volume spin waves in a longitudinally magnetized ferrite film was experimentally studied. Narrowing of the frequency band of propagation and the subsequent complete suppression of the volume spin waves with an increase of the pumping power were observed for the magnetic fields and frequencies allowing three-wave processes of the volume wave splitting. *© 2000 MAIK "Nauka/Interperiodica".*

Excitation of the spin waves (SW) and oscillations in ferrite films is accompanied by nonlinear phenomena such as the formation of envelope solitons, parametric wave amplification, chaos, bistability, etc., that are interesting from the standpoint of physics and can be used in various devices of the solid-state microwave electronics. The knowledge of the peculiarities of the interaction of two or more SWs of different powers propagating simultaneously in a ferrite film is important for understanding these phenomena.

Spin waves of low power do not interact with each other. However, nonlinearity of the magnetic subsystem of ferrite results in a mutual influence of the waves in the case of high intensities. It was demonstrated that a high-power surface SW causes an increase in the damping [1–3] and insignificant changes in the wave numbers [4] of the surface SWs of low power that propagate in the same film. The effect was observed for narrow frequency intervals around the pumping frequency. It was explained by the influence of the parametrically excited magnons formed due to three-wave processes of the pumping wave splitting [5, 6]. Krutsenko *et al.* [7] considered the influence of homogeneous pumping at a frequency not belonging to the range of three-wave processes on the parameters of the volume SW. Parametric amplification of the volume SW by homogeneous pumping in a narrow frequency interval around half of the pumping frequency was demonstrated in [8].

In this work, we report on the first observation of the effective influence of a high-power pumping volume SW on the decay of a weak volume SW propagating in the same ferrite film. This broad-band effect of the threshold type was observed for the frequency range of the three-wave mixing.

The measurements were carried out in a standard configuration of the transmission line [1]. We used a line with a yttrium–iron garnet (YIG) ferrite film grown by the method of liquid phase epitaxy on a nonmagnetic substrate. The film had a thickness of 8.7 μm, the lateral dimensions 2 × 20 mm, the saturation magnetization $4\pi M$ = 1750 G, and the homogeneous ferromagnetic resonance bandwidth 0.6 Oe. Two microstrip transducers, each with a thickness of 50 μm and a length of 2 mm, provided the excitation and detection of SW in the YIG film. The transducers were placed near the surface of the film at a distance of 4 mm from each other. The whole structure was placed between the poles of an electromagnet generating an external homogeneous tangential magnetic field H_e directed along the long axis of the film and perpendicularly to the transducers. This configuration provided excitation of the backward volume spin waves (BVSW) in the YIG film [9]. An R2-78 panoramic detector measured the amplitude–frequency characteristics (AFC) of the transmission line under the linear regime of SW propagation at a signal power of P = –10 dB m. A continuous monochromatic pumping signal with the fixed frequency f_p was fed simultaneously to the input transducer from an oscillator via an amplifier and a T-junction box. The pumping frequency f_p was varied from 2 to 6 GHz and the pumping power P_p was up to +20 dB m. Rectifiers prevented mutual influence of the panoramic detector and the oscillator in the measuring system.

Figure 1a shows a typical AFC of the transmission line [the dependence of the transmission losses in dB, $L = 10\log(P_{\text{out}}/P)$ on the signal frequency f] measured for zero pumping and a magnetic field intensity of H_e = 490 Oe. Within a 300-MHz band ranging from the lower limit frequency f_a to the upper limit frequency f_b at a level of –80 dB, the signal in the YIG film is transmitted by spin waves. For a tangentially magnetized ferrite layer, the theory [9] predicts the existence of exchangeless BVSW in the frequency interval ranging from $f_L = \gamma H$ to $f_U = \gamma\sqrt{H(H + 4\pi M)}$, where

1063-7850/00/2604-0315$20.00 © 2000 MAIK "Nauka/Interperiodica"

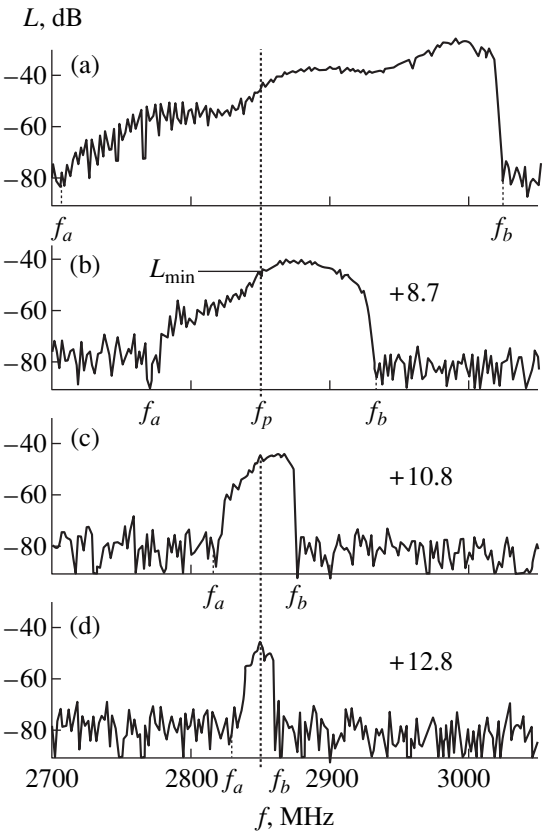

Fig. 1. Amplitude–frequency characteristics for BVSW in the transmission line at a magnetic field intensity of H = 490 Oe and different pumping powers: (a) zero pumping; (b)–(d) the pumping powers in dB m are indicated by figures at the graphs.

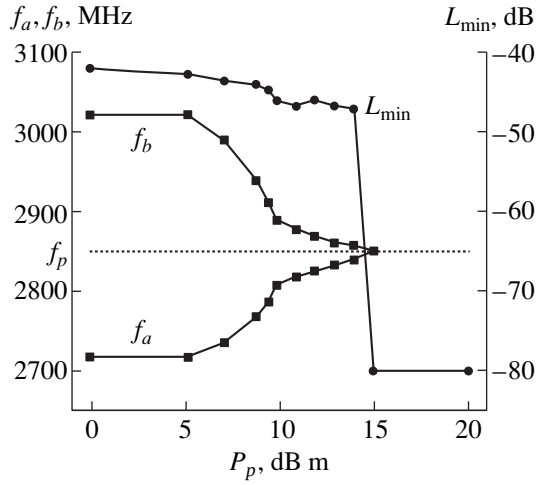

Fig. 2. Experimental dependences of the lower (f_a) and upper (f_b) limiting frequencies of the BVSW band of the transmission line and the level of losses L_p at the pumping frequency f_p on the pumping power P_p.

γ = 2.8 MHz/Oe is the gyromagnetic ratio. Assuming equality of the measured (f_b = 3020 MHz) and the theoretically predicted (f_U) upper limiting frequencies, we obtain the value of the effective field inside the ferrite: H = 513 Oe. A slight difference between the measured (H_e) and the calculated (H) fields is determined entirely by the effects of demagnetization and anisotropy of the YIG film that were not taken into account in the calculations. The measured lower limiting frequency f_a = 2710 MHz was also higher than the calculated frequency f_L = 1436 MHz because the transducer with a width of 50 μm excited only waves with the wave numbers from 0 to ~600 m^{-1} and the frequencies close to the upper limiting frequency f_U of the BVSW.

Figures 1b–1d demonstrate influence of the pumping wave with the frequency f_p belonging to the BVSW frequency band on the shape of the AFC of the transmission line. For clarity, the pumping frequency f_p = 2850 MHz is selected in the middle of the BVSW frequency range. The increase of the pumping power was accompanied by monotonic increase of the lower (f_a) and decrease of the upper (f_b) limiting frequencies resulting finally in complete vanishing of the signal transmission band. The transmission level L_p (see Fig. 1c) at the pumping frequency initially decreased slowly with the increase of the pumping power and then fell abruptly down to the noise level. Figure 2 shows the experimental dependences of the observed limiting frequencies f_a and f_b and the transmission level L_p on the pumping power P_p. It is seen that the narrowing of the BVSW transmission band has a threshold character and starts in the given case at a pumping power of $P_p \approx$ +5 dB m. The complete suppression of the transmitted signal down to the noise level of –80 dB takes place at a pumping power of about +15 dB m.

In the magnetic field with H_e = 490 Oe, the effective influence of the continuous pumping wave on the AFC of the transmission line was observed for any pumping frequency in the BVSW frequency band. The increase of the power resulted in all cases in narrowing of the transmission band, whereby both upper and lower limiting frequencies shifted toward the pumping frequency. Shifting the pumping frequency to the upper or lower limiting frequency of the AFC of the transmission line was accompanied by an increase of the pumping power corresponding to complete suppression of the transmission band.

Similar measurements were carried out for various values of the magnetic field intensity. The decrease of the field down to H_e = 200 Oe and the corresponding shift of the AFC to the frequency range around 1700 MHz led to the increase of the minimum losses of BVSW in the transmission line to the level of –40 dB. However, the effect was still observed and the total suppression of the signal took place at a pumping power of less than –5 dB m. The influence of pumping on the AFC of the transmission line decreased with increasing field intensity. In the frequency range f > 3300 MHz, the pumping with a power of less than +20 dB m virtually does not influence the shape of the AFC of the transmission band at a field intensity of H_e > 580 Oe.

The experimental results provide evidence of a relationship between the pumping influence on the AFC of the transmission line and the processes of splitting of a high-power BVSW of the pumping wave into the volume spin waves. The phase matching conditions for the three-wave mixing are as follows: $f_p = f_1 + f_2$ and $\mathbf{k}_p = \mathbf{k}_1 + \mathbf{k}_2$, where ($f_p$, $\mathbf{k}_p$), (f_1, $\mathbf{k}_1$), and (f_2, $\mathbf{k}_2$) are the frequencies and wave vectors of the pumping wave and the generated volume waves, respectively. Detailed analysis of the dispersion relations for exchangeless BVSW in a ferrite film shows [10] that BVSW of pumping with a small wave number k_p can split into two BVSWs with large wave numbers k_1 and k_2 corresponding to two different modes and propagating in the opposite directions. The frequencies of these waves f_1 and f_2 are nearly equal and are close to $f_p/2$. A condition of the pumping half-frequency falling into the BVSW frequency range implies that such processes are only possible for the magnetic fields weaker than the critical value $H_c = 4\pi M/3$ and the frequencies lower than the critical frequency $f_c = \gamma\sqrt{H_c(H_c + 4\pi M)}$. Substituting the values of the parameters for the YIG film, we determine that $H_c = 583$ Oe and $f_c = 3266$ MHz. The calculated values agree well with the boundaries of the frequency and field intensity ranges where the influence of the pumping on AFC of the transmission line was observed.

Faster decay of a weak BVSW that forms AFC of the transmission line in the presence of a high-power BVSW of pumping can be determined by the incoherent scattering of the weak wave on the parametrically excited volume spin waves. When the pumping power was slightly higher than the threshold level, only the lowest volume modes were excited in a narrow frequency interval far from the pumping frequency f_p (cf. [6]), which resulted in suppression of the peripheral part of AFC in the low-frequency range. The further increase of the pumping power presumably caused the excitation of the highest volume modes, the corresponding broadening of the frequency range, and subsequent stochastization of the excited spin waves, which was the reason of narrowing of the observed AFC around the pumping frequency f_p. High-power pumping suppresses a volume SW with higher efficiency and in a wider frequency range than in the case of surface SW suppression [1–4], which is explained by increase of the length of the film fragment where the incoherent scattering of BVSW takes place (in the case considered, the parametrically excited waves propagated along the longitudinal axis of the film rather than in the transverse direction). A theory describing the evolution of SWs in ferrite films at high power of the signal is necessary for unambiguous interpretation of the mechanism of the pumping wave action on the AFC of BVSW of the transmission line.

Note, finally, that the effect of narrowing of the AFC of the transmission line under the action of a high-power pumping wave can be used for development of the microwave filters with electrically controlled width of the transmission band.

REFERENCES

1. O. A. Chivileva, A. N. Anisimov, A. G. Gurevich, *et al.*, Pis'ma Zh. Tekh. Fiz. **13**, 1497 (1987) [Sov. Tech. Phys. Lett. **13**, 627 (1987)].
2. A. V. Vashkovskiĭ, V. I. Zubkov, É. G. Lokk, and S. A. Nikitov, Fiz. Tverd. Tela (Leningrad) **30**, 827 (1988) [Sov. Phys. Solid State **30**, 475 (1988)].
3. A. N. Anisimov, O. A. Chivileva, and A. G. Gurevich, Fiz. Tverd. Tela (Leningrad) **32**, 1622 (1990) [Sov. Phys. Solid State **32**, 946 (1990)].
4. G. T. Kazakov, A. V. Kozhevnikov, and Yu. A. Filimonov, Zh. Éksp. Teor. Fiz. **115**, 318 (1999) [JETP **88**, 174 (1999)].
5. A. M. Mednikov, Fiz. Tverd. Tela **23**, 242 (1981) [Sov. Phys. Solid State **23**, 136 (1981)].
6. A. A. Temiryazev, Fiz. Tverd. Tela (Leningrad) **29**, 313 (1987) [Sov. Phys. Solid State **29**, 179 (1987)].
7. I. V. Krutsenko, G. A. Melkov, and S. A. Ukhanov, Fiz. Tverd. Tela (Leningrad) **26**, 3434 (1984) [Sov. Phys. Solid State **26**, 2062 (1984)].
8. P. A. Kolodin, C. E. Patton, B. A. Kalinikos, *et al.*, Phys. Rev. Lett. **80**, 1976 (1998).
9. R. W. Damon and J. R. Eshbach, J. Phys. Chem. Solids **19**, 308 (1961).
10. V. L. Preobrazhenskiĭ, V. P. Rybakov, and Yu. K. Fetisov, Radiotekh. Élektron. (Moscow) **33**, 1218 (1988).

Translated by A. Chikishev

Technical Physics Letters, Vol. 26, No. 4, 2000, pp. 318–319. Translated from Pis'ma v Zhurnal Tekhnicheskoĭ Fiziki, Vol. 26, No. 8, 2000, pp. 8–11.

Quantization of Natural Systems

A. G. Chirkov and I. V. Kazinets

St. Petersburg State Technical University, St. Petersburg, Russia

Received November 26, 1999

Abstract—New rules for the quantization of classical systems are proposed which generalize the traditional rules and reduce to these rules, provided that transition to the Cartesian coordinates is possible. An equation is suggested that offers generalization of the Schrödinger equation to arbitrary natural systems. Using the minimum coupling (strong equivalence) principle, this equation can be extended to arbitrary spaces with curvature.

The term "quantization" appeared in the physical literature in the 1920s. From the very beginning, this term had a twofold meaning: (i) discretization of a manifold of values of some quantity and (ii) construction, proceeding from a classical mechanical system with a *c*-numerical Hamiltonian $H(p, q, t)$, of the Hamiltonian operator $\hat{H}(\hat{p}, \hat{q}, t)$, where $\hat{p}$ and $\hat{q}$ are the operators corresponding to the classical canonical variables. Below, the term quantization is used in the second meaning.

The traditional approach to quantization, known as the Weyl–Heisenberg scheme, is applicable only to classical systems with a flat phase space and Cartesian coordinates [1]. In the general case, the quantization problem is neither trivial nor single-valued, since there are many ways of selecting the form of operator $\hat{p}$ and positioning the operators $\hat{p}$ and $\hat{q}$ in $\hat{H}(\hat{p}, \hat{q}, t)$.

Let us consider a natural mechanical system representing a triad (M, T, V), where M is a smooth manifold (space of positions), T is a Riemannian metric on M (positively definite quadratic form–kinetic energy), and V is a smooth function (potential of a force field) [2]. The motion of this system is described by smooth transformations q: $R^1 \longrightarrow M$ represents extremals of the action functional with the Lagrangian $L = T - V$. In the local coordinates, the Lagrangian has the following form:

$$L = \frac{1}{2} g_{ik} \dot{q}^i \dot{q}^k - V(q), \tag{1}$$

where the repeated indexes imply summation from 1 to n.

The Hamiltonian corresponding to Lagrangian (1) is

$$H = \frac{1}{2} g^{ik} \pi_i \pi_k + V(q), \tag{2}$$

where $\pi_i = g_{ik}\dot{q}^k$ is the generalized momentum. The local coordinates q^i, π_i are canonical coordinates on the tangential vibration T^*M of the smooth manifold M. In the case of nontrivial values $g_{ik} \neq \delta_{ik}$, the traditional quantization scheme becomes essentially non-single-valued. However, there is a means of rendering this procedure quite determinate.

Indeed, the traditional scheme of solving the quantization problems in curvilinear coordinates is as follows. Initially, the classical system is quantized in Cartesian coordinates, whereby the meaning of kinetic energy $T = \frac{1}{2m}(p_x^2 + p_y^2 + p_z^2)$ in the Schrödinger representation is assigned to the operator $\hat{T} = -\hbar^2\Delta/2m$ (where Δ is the Laplace–Beltrami operator defined on a tangential vibration of the smooth manifold M); the variables are then changed to the curvilinear coordinates q. The resulting wavefunction $\psi(q) = \psi(x(q))$ (where x denotes the set of Cartesian coordinates) is not the probability amplitude and does not describe any physical state, since the real probability amplitude must obey the following relationship on the passage to the curvilinear coordinates:

$$l = \int_{R^n} |\psi(x)|^2 dx = \int_M |\psi(x(q))|^2 g^{1/2} dq = \int_M |\tilde{\psi}(q)|^2 dq, \tag{3}$$

where $dx = dx^1 dx^2 \ldots dx^n$, $dq = dq^1 dq^2 \ldots dq^n$, and $q = \det|g_{ik}|$ [3]. Relationship (3) leads to the following relationship between the probability amplitude and the wavefunction $\psi(x(q))$:

$$\tilde{\psi}(q) = g^{1/4} \psi(x(q)). \tag{4}$$

It is now evident that an equation must be derived directly in terms of the probability amplitude $\tilde{\psi}(q)$.

This equation has the following form:

$$\left[\left(g^{-\frac{1}{4}}\frac{\partial}{\partial q^i}g^{1/4}\right)g^{ik}\left(g^{1/4}\frac{\partial}{\partial q^k}g^{-1/4}\right)\right]\tilde{\psi}(q) + \frac{2m}{\hbar^2}[E - V(q)]\tilde{\psi}(q) = 0$$

or

$$\tilde{\Delta}\tilde{\psi}(q) + \frac{2m}{\hbar^2}[E - V(q)]\tilde{\psi}(q) = 0, \quad (5)$$

where $\tilde{\Delta} = g^{1/4}\Delta g^{-1/4}$.

The symmetry (self-conjugacy) of operator $\tilde{\Delta}$ with respect to the scalar product $(\tilde{\varphi}, \tilde{\psi}) = \int\overline{\tilde{\varphi}(q)}\tilde{\psi}(q)dq$ (the bar denotes complex conjugation) is evident from the following chain of equations: $(\tilde{\Delta}\tilde{\varphi}, \tilde{\psi}) = (\Delta\varphi, \psi) = (\varphi, \Delta\psi) = (\tilde{\varphi}, \tilde{\Delta}\tilde{\psi})$.

Let us introduce the projective operators of generalized momentum,

$$\hat{\pi}_i = -i\hbar g^{-1/4}\frac{\partial}{\partial q^i}g^{1/4}, \quad (6)$$

satisfying the following commutation relationships:

$$[\hat{\pi}_e q^k] = -i\hbar\delta_e^k, \quad [\hat{\pi}_i, \hat{\pi}_k] = 0, \quad [q^i, q^k] = 0. \quad (7)$$

The conjugate operator $\hat{\pi}_i$ can be written as

$$\hat{\pi}_i^* = -i\hbar g^{1/4}\frac{\partial}{\partial q^i}g^{-1/4}, \quad (8)$$

and the kinetic energy operator acquires the form

$$\hat{T} = -\frac{\hbar^2}{2m}\hat{\pi}_i g^{ik}\hat{\pi}_k^*; \quad (9)$$

the commutation relationships (7) are algebraically identical to the conventional Heisenberg commutation relationships. However, the operators $\hat{\pi}_i$, q^k define a representation which is not unitarily equivalent to the Schrödinger representation. The uniqueness theorems of Rellich–Diqsmier and von Neumann–Stone [4] do not apply to this case because operators $\hat{\pi}_i$ and not symmetric (non-self-conjugate).

The operator of kinetic energy, being the operator of a physical quantity, is self-conjugate. In contrast, the generalized momentum in the general case is not a physical quantity and, hence, is not necessarily represented by a self-conjugate operator.

The generalized momentum operator corresponding to a radial coordinate (radial momentum operator) has the following form:

$$\hat{\pi}_r = \frac{\partial}{\partial r} + \frac{n-1}{2r},$$

where n is the dimension of the manifold M defined on the domain $D(\hat{\pi}_r) = \{\tilde{\psi} \in L^2((0, \infty), dr);\ \tilde{\psi}' + ((n - 1)/2r)\tilde{\psi} \in L^2((0, \infty), dr\}$. This result coincides with relationship [5, (7.8.2)], where the form of the radial momentum operator was postulated.

Equation (5) offers a possibility of further generalization. Indeed, from the standpoint of the manifold theory, even a flat space is not as simple, being (in contrast to the usual differentiable manifold) an affinely connected manifold and, hence, having a much more developed structure. This affine connection is not manifested in Cartesian coordinates, in which the Christoffel symbols are zero. However, should the physical laws be formulated in a flat space in terms of curvilinear coordinates, the connection becomes observable. Most of the laws written in this form contain the Christoffel symbols (rather than the Riemann tensor) and the corresponding equations have the form independent of whether the manifold is flat or curved. Thus, it would be natural to postulate that the form of the Schrödinger equation (5) for curved manifolds (on which no global Cartesian coordinate system is defined) is the same as that for curvilinear coordinates on a flat manifold. This postulate is analogous to the principle of minimum coupling in the general theory of relativity [6].

In concluding, it should be noted that, using the methods developed in [7, 8], it is possible to generalize equation (5) so as to render it applicable to a manifold with nontrivial topology.

REFERENCES

1. F. A. Berezin, Izv. Akad. Nauk SSSR, Ser. Mat. **38**, 1116 (1974).
2. V. V. Kozlov, *Symmetry, Topology and Resonances in Hamiltonian Mechanics* (Izhevsk, 1995).
3. W. Feller, *An Introduction to Probability Theory and Its Applications* (Wiley, New York, 1965).
4. N. Hart, *Geometric Quantization in Action* (North-Holland, Dordrecht, 1983).
5. R. D. Richtmyer, *Principles of Advanced Mathematical Physics* (Springer, New York, 1978), Vol. 1, 2.
6. B. Schutz, *Geometric Methods of Mathematical Physics* (Cambridge University Press, Cambridge, 1980).
7. Yu. P. Goncharov and J. V. Yarevskaya, Mod. Phys. Lett. A **9**, 3175 (1994).
8. Yu. P. Goncharov, Phys. Lett. B **398**, 32 (1997).

Translated by P. Pozdeev

Technical Physics Letters, Vol. 26, No. 4, 2000, pp. 320–322. Translated from Pis'ma v Zhurnal Tekhnicheskoĭ Fiziki, Vol. 26, No. 8, 2000, pp. 12–17.

Effect of Deformation on the Permeability of Porous Titanium–Nickel Alloys

V. É. Gyunter, V. N. Khodorenko, A. N. Monogenov, and Yu. F. Yasenchuk

Institute of Medical Materials and Shape-Memory Implants, Tomsk, Russia

Received November 2, 1999

Abstract—The values of permeability ratio were determined for several porous titanium–nickel alloys with various average pore size. It was established that the flow rate of various fluids through the porous alloys under the reversible alternating strain conditions decreases on stretching and increases on compression of the samples. A 10% change in the strain level leads to a 15% variation in the fluid flow rate. © *2000 MAIK "Nauka/Interperiodica".*

Biocompatible porous metal materials based on TiNi alloys are widely used in medicine as implants [1–4]. Possessing high elastic properties, these alloys mechanically behave much like tissues in the human organism and are capable of functioning under real living organism conditions. These conditions involve reversible straining action of tissues, with alternating sign and considerable amplitude, upon the implanted material. Under the action of deformation, the porous space in TiNi alloys exhibits variations leading to changes in the conditions of tissue fluid circulation.

The purpose of this work was to determine the permeability ratio of porous TiNi alloys with respect to various model fluids and to study the effect of deformation on these properties.

The experiments were performed on the samples of porous titanium–nickel alloys obtained by self-propagating hydride reduction synthesis (SHS) in the form of cylinders with a length of 40 mm and various diameters (24, 18, and 16 mm). For comparison, we have studied a sample of porous thighbone with a length of 30 mm and a diameter of 21 mm. All the samples were characterized by the average pore size determined using the secant method. For the TiNi alloy samples with various diameters indicated above, these values were d_1 = 275 μm, d_2 = 420 μm, and d_3 = 615 μm, respectively. The average pore size in the natural bone was d_0 = 500 μm. The porosities of all the metal samples were the same (P = 69%), irrespective of the average pore size, and the thighbone porosity was 80%.

The volume flow rate of the filtered fluids and the corresponding permeability ratios were determined by the Darcy method [5]. The filtration experiments were performed using model fluids with various densities and viscosities: water, ethyl alcohol, and glycerol. During the measurement, the porous samples were connected to a reservoir in which the fluid level was maintained on a constant level during the whole experiment. The flow rate Q was determined upon completely impregnating the sample with one of the fluids.

It was found that the flow rate in all samples increased with increasing average pore size (Fig. 1a) and decreasing fluid viscosity (Fig. 1b). Based on the experimental plots of flow rate versus average pore size, all the porous materials studied were characterized by the permeability ratios K for various fluids calculated by the Darcy formula [5]:

$$K = \frac{Q\mu L}{\rho g \Delta H S P}, \qquad (1)$$

where Q is the flow rate; ΔH is the fluid column height; g is the acceleration of gravity; S and L are the sample cross section and length, respectively; ρ and μ are the fluid density and dynamic viscosity, respectively; and P is the sample porosity. The results of these calculations are presented in the table.

The results of our experiments show that the permeability ratio increases with the average pore size and the penetrant viscosity. Note that the growth of K with the

Permeability factors (K, m^2) of TiNi samples with different average pore size with respect to various model fluids

Sample	Average pore size d, μm	Water	Ethyl alcohol	Glycerol
Finely-porous (d_1)	275	0.27×10^{-9}	0.66×10^{-9}	1.6×10^{-9}
Medium-porous (d_2)	420	2.1×10^{-9}	3.5×10^{-9}	12×10^{-9}
Thighbone (d_0)	500	1.7×10^{-9}	2.9×10^{-9}	18×10^{-9}
Coarsely-porous (d_3)	615	4.9×10^{-9}	7.9×10^{-9}	62×10^{-9}

1063-7850/00/2604-0320$20.00

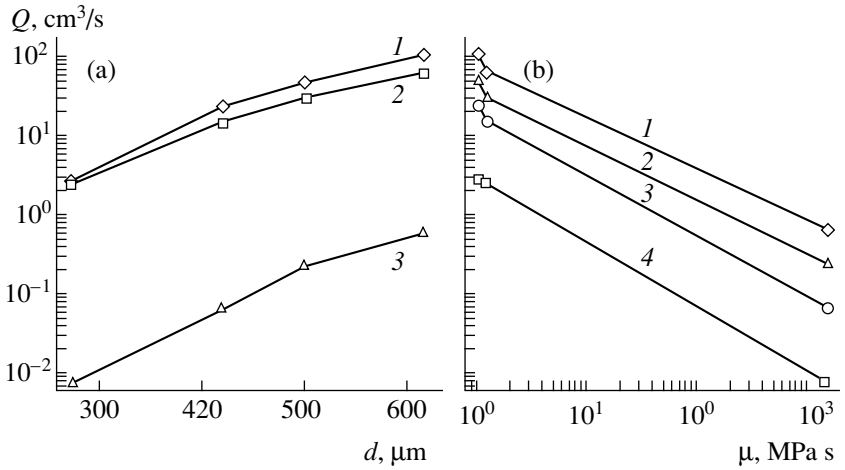

Fig. 1. The plots of flow rate Q in porous titanium–nickel alloys and natural bone: (a) versus average pore size d for (*1*) water, (*2*) ethyl alcohol, and (*3*) glycerol; (b) versus fluid viscosity μ for an average pore size of (*1*) 615, (*2*) 500 (thighbone), (*3*) 420, and (*4*) 275 μm.

pore size is related only to the increasing volume flow rate, as seen from formula (1), where all terms except Q remain unchanged at a constant porosity. The porosity was the same for all metal samples, while their structural properties varied with the average pore size. It is important to note that formula (1) does not explicitly contain the average pore size. The volume flow rate varies depending on the structural properties, as determined by the internal pressure losses in the porous medium (amounting to 0.93–0.97% of the total losses [6]. In particular, the flow in a sample with fine pores is characterized by increasing losses related to the flow transformation from continuous to multistream, with the number of streams equal to the number of pores on the filtration cross-section area, and to the interaction and mixing of streams at the pore exit or in merging pores. Thus, the finely porous samples are characterized by a higher level of internal losses; lower volume flow rate; and, hence, lower permeability ratio than the samples with coarse pores.

For a laminar flow of a filtered fluid, the permeability ratio must be a constant, which is characteristic of the filter and does not depend on the properties of fluids [7]. In real systems, however, the viscosity of a fluid affects the permeability ratio, with the effect increasing with the average pore size (see table). This behavior is explained by the fact that fluids filtered in porous materials may flow both in the laminar mode and in the transient (laminar-turbulent) or turbulent modes [6]. In addition, a large specific area and considerable surface roughness of the filtration medium may also significantly affect the flow character, increasing the contribution of the turbulent flow mode. Although the flow rate decreases with increasing viscosity, the permeability coefficient in formula (1) grows, which implies that the dynamic viscosity affects the permeability ratio to a much greater extent than does the structural factor.

Taking into account a contribution due to deformation of the filter material, we obtain a modified Darcy formula [5] for calculating the flow rate:

$$Q = \frac{K\rho g\Delta HSP}{\mu L(1 \pm \varepsilon)^2}, \qquad (2)$$

where $+\varepsilon$ is the fractional deformation in tension and $-\varepsilon$ is that in compression. The sample volume before and after deformation is assumed to be the same.

An analysis of the experimental results showed that the flow rate of the fluids markedly decreased upon stretching of the porous materials studied and increased upon their compression. It was established that a 10% change in the sample deformation level led to a 15% variation in the flow rate (Fig. 2). Dependence of the penetrant flow rate on the filter deformation was more pronounced in the samples with greater pores.

Thus, the flow rate of a fluid through porous TiNi alloy samples, obtained by SHS synthesis and studied under the reversible alternating strain conditions,

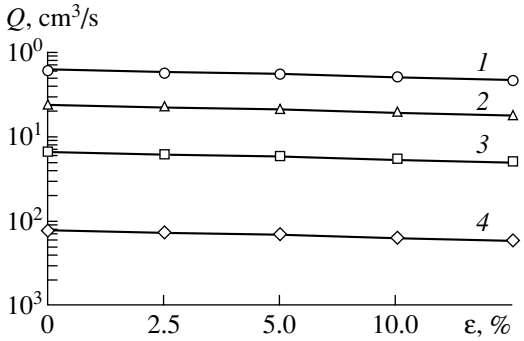

Fig. 2. The plots of glycerol flow rate Q versus strain ε in natural bones and porous titanium–nickel alloys with different average pore size: of (*1*) 615, (*2*) 500 (thighbone), (*3*) 420, and (*4*) 275 μm.

depends on the average pore size in the material and on the fluid viscosity. The reversible alternating strain produces pulsations in the penetrant flow as a result of pressure oscillations in the sample pores.

REFERENCES

1. V. É. Gyunter, G. Ts. Dambaev, P. G. Sysolyatin, *et al.*, *Medicinal Materials and Shape-Memory Implants* (Tomsk. Gos. Univ., Tomsk, 1998).
2. *Proceedings of the International Conference "Superelastic Medicinal Materials and Shape-Memory Implants," Tomsk, 1998* (Tomsk. Gos. Univ., Tomsk, 1998).
3. V. É. Gyunter, P. G. Sysolyatin, F. T. Temerkhanov, *et al.*, *Superelastic Medicinal Materials and Shape-Memory Implants in Maxillofacial Surgery, Traumatology, Orthopedia, Neurosurgery* (Tomsk. Gos. Univ., Tomsk, 1995).
4. G. Ts. Dambaev, V. É. Gyunter, A. A. Radionchenko, *et al.*, *Superelastic Porous Shape-Memory Implants in Surgery* (Tomsk. Gos. Univ., Tomsk, 1996).
5. V. M. Entov, Soros. Obrazov. Zh., No. 2, 122 (1998).
6. P. A. Vityaz', V. M. Kaptsevich, and V. K. Sheleg, *Porous Powder Materials and Related Articles* (Vysshaya Shkola, Minsk, 1987).
7. S. V. Belov, P. A. Vityaz', and V. K. Sheleg, *Porous Permeable Materials* (Metallurgiya, Moscow, 1987).

Translated by P. Pozdeev

Technical Physics Letters, Vol. 26, No. 4, 2000, pp. 323–325. Translated from Pis'ma v Zhurnal Tekhnicheskoĭ Fiziki, Vol. 26, No. 8, 2000, pp. 18–23.

Effect of Grain Boundary on the Character of Pulse-Train-Induced Cleavage Fracture in Copper Crystal

K. P. Zol'nikov, T. Yu. Uvarov, V. A. Skripnyak, A. G. Lipnitskiĭ, D. Yu. Saraev, and S. G. Psakh'e

Institute of Strength Physics and Materials Science, Siberian Division, Russian Academy of Sciences, Tomsk, 634055 Russia

Received December 3, 1999

Abstract—The process of pulse-train-induced cleavage fracture in a copper crystal with grain boundary was studied by methods of computer simulation. It is demonstrated that trains of isolated compression pulses induced in the material favor the tendency to fracture propagation along the grain boundary. © *2000 MAIK "Nauka/Interperiodica".*

Investigation of the phenomenon of cleavage fracture in a material under the action of high-energy pulses is currently an important task, since deeper insight into this problem would allow the behavior of various materials under extremal conditions to be predicted [1–3]. The laws of cleavage fracture have been widely studied by methods of computer simulation [4–6]. The results of modeling showed that a high-energy pulsed action upon a crystal lattice may lead to the formation of a train (packet) of isolated compression pulses (ICPs). In particular, it was established that pulsed loading (high-rate mechanical action, rapid electron-beam local heating of the free surface, etc.) of a crystalline material may give rise to ICPs with the properties analogous to those of solitons [7–9]. Recently, we have demonstrated [10] that the ICP amplitude on the free surface may increase by a factor of 1.5–2, depending on the crystallographic direction. Upon reflection from such a surface, the energy is partly dissipated in the near-surface region.

The purpose of this work was to elucidate the effect of a grain boundary occurring near the free surface on the character of cleavage fracture in a crystal lattice loaded by a train containing several ICPs of large amplitude.

We have simulated the pulsed loading of a copper crystal using a molecular dynamics method [7, 8, 11] in which the interatomic interactions are described by the method of embedded atom [12–15]. The model crystals contained more than 12000 atoms, representing two grains with the ideal FCC structure rotated relative to one another by an angle of 38.21° about the [111] axis (a special boundary of the Σ7 type). The grain boundary was oriented parallel to the free surface and spaced from this surface by 24 interplanar distances. The boundary conditions corresponded to a hard surface on the side of loading and to a free surface on the opposite side. Directions perpendicular to the axis of loading were characterized by periodic boundary conditions. The external action was modeled by imparting a definite set of initial velocities to atoms in a certain region of the crystal such that the atoms and the ICPs formed would travel in the direction perpendicular to the grain boundary and the free surface.

The simulation results showed that the ICPs emerging at the free (rear) surface may lead to the cleavage fracture in the material on a nanometer scale, the character of this fracture being determined by the material structure, the presence of grain boundaries, and the number of ICPs formed upon the pulsed loading. For example, the passage of a train comprising two ICPs with a pulse amplitude of 3300 m/s through the grain boundary described above leads to the formation of a cleavage fracture zone along the boundary, but this action is insufficient for complete separation of the two crystalline regions. At the same time, a train of four ICPs of the same amplitude interacting with the grain boundary leads to fracture of the sample along this boundary. The kinetics of fracture in this case is illustrated by Fig. 1. As seen from this figure, the second grain is cleaved from the sample. According to the results of calculations, the detached part is markedly (by a factor of approximately five) greater than the fragments cleaved from the ideal crystal under the same load.

A comparative analysis of changes in the structure of crystalline regions shows a considerable difference in the patterns formed under the action of trains containing two and four ICPs. In the former case, a part of the second grain is cleaved from the rear surface and the

1063-7850/00/2604-0323$20.00 © 2000 MAIK "Nauka/Interperiodica"

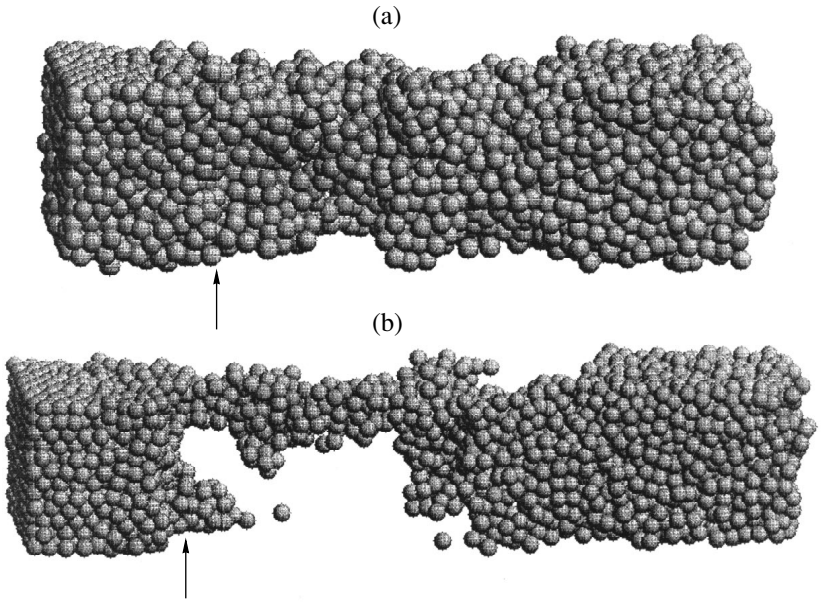

Fig. 1. Dynamics of cleavage fracture in a copper crystal (a fragment of sample). Arrows indicate the grain boundary position.

material is stretched along the grain boundary (Fig. 2), while in the later case the material exhibits fracture along the boundary. It should be noted that crystal structure of the separated grain also exhibits characteristic changes. The part of the grain adjacent to the rear surface retains the old structure, while material near the grain boundary is stretched (Fig. 2). This behavior of the modeled crystal reflects the character of interaction between the ICP train and the grain boundary. Calculations showed that, as the ICPs forming a train pass through the boundary, their energies decrease. Moreover, every next ICP loses a greater fraction of the energy than the preceding one, the energy being spent for heating and stretching of the grain-boundary region.

The results of modeling show that atoms in the part cleaved from the crystal exhibit a considerable scatter in velocities, which is much more pronounced than that in the sample without grain boundary loaded to the same extent. Deviation of the atomic velocities from the average value (500 m/s) increases with time, which indicates that the separated part has a tendency to split into smaller fragments.

Based on the results of calculations performed in this work, we may conclude that polycrystalline copper loaded with a train of isolated compression pulses (ICPs) has a tendency to fracture along the grain boundaries. As the number of ICPs in the train increases, the cleavage fracture takes place along the grain boundaries spaced by greater distance from the free surface. The separated parts tend to decay into smaller fragments with time because of increasing scatter in atomic velocities.

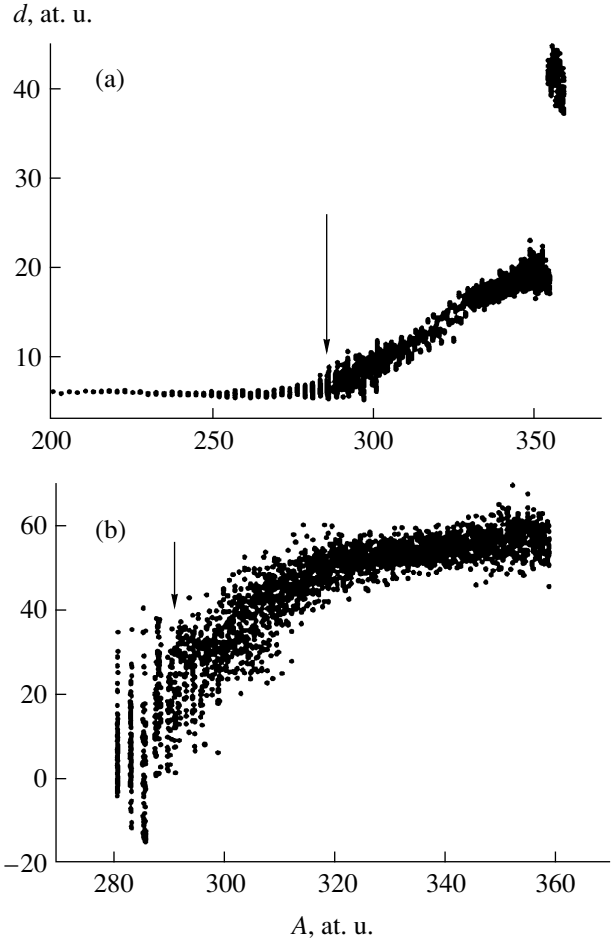

Fig. 2. The plots of atomic displacement d vs. coordinates A of atoms in a copper crystal loaded with a train of (a) two and (b) four isolated compression pulses.

REFERENCES

1. Ya. B. Zel'dovich and Yu. P. Raĭzer, *Physics of Shock Waves and High-Temperature Hydrodynamic Phenomena* (Nauka, Moscow, 1966; Academic Press, New York, 1966).
2. V. S. Nikiforovskiĭ and E. I. Shemyakin, *Dynamic Fracture of Solids* (Nauka, Novosibirsk, 1979).
3. A. V. Bushman, G. I. Kanel', A. L. Ni, and V. E. Fortov, *Thermophysics and Dynamics of Intensive Pulsed Actions* (Chernogolovka, 1988).
4. L. Seaman, D. R. Curran, and W. J. Murr, Trans. ASME, J. Appl. Mech. **52**, 593 (1985).
5. D. R. Curran, in *Shock Waves in Condensed Matter*, Ed. by S. C. Schmidt and N. C. Holms (Elsevier, New York, 1988), pp. 321–326.
6. K. P. Zol'nikov, T. Yu. Uvarov, A. G. Lipnitskiĭ, *et al.*, Pis'ma Zh. Tekh. Fiz. **25**, 22 (1995) [Tech. Phys. Lett. **25**, 936 (1999)].
7. S. G. Psakh'e, K. P. Zol'nikov, and S. Yu. Korostelev, Pis'ma Zh. Tekh. Fiz. **21**, 1 (1995) [Tech. Phys. Lett. **21**, 489 (1995)].
8. S. G. Psakh'e, K. P. Zol'nikov, and D. Yu. Saraev, Fiz. Goreniya Vzryva **33**, 43 (1997).
9. K. P. Zol'nikov, R. I. Kadyrov, I. I. Naumov, *et al.*, Pis'ma Zh. Tekh. Fiz. **25**, 12 (1999) [Tech. Phys. Lett. **25**, 637 (1999)].
10. S. G. Psakh'e, K. P. Zol'nikov, R. I. Kadyrov, *et al.*, Fiz. Goreniya Vzryva **35**, 106 (1999).
11. S. G. Psakh'e, K. P. Zol'nikov, and D. Yu. Saraev, Pis'ma Zh. Tekh. Fiz. **24**, 42 (1998) [Tech. Phys. Lett. **24**, 99 (1998)].
12. S. M. Foiles, M. I. Baskes, and M. S. Daw, Phys. Rev. B **33**, 7983 (1986).
13. A. V. Berch, A. G. Lipnitskiĭ, and E. V. Chulkov, Poverkhnost', No. 6, 23 (1994).
14. S. V. Eremeev, A. G. Lipnitskiĭ, A. I. Potekaev, and E. V. Chulkov, Phys. Low-Dimens. Struct., No. 3/4, 127 (1997).
15. G. G. Rusina, A. V. Berch, I. Yu. Sklyadneva, *et al.*, Fiz. Tverd. Tela (St. Petersburg) **38**, 1120 (1996) [Phys. Solid State **38**, 619 (1996)].

Translated by P. Pozdeev

Technical Physics Letters, Vol. 26, No. 4, 2000, pp. 326–327. Translated from Pis'ma v Zhurnal Tekhnicheskoĭ Fiziki, Vol. 26, No. 8, 2000, pp. 24–27.

Silicon Single Crystals Ion-Doped with Ytterbium

D. É. Nazyrov*, S. A. Goncharov, and A. V. Suvorov****

** Tashkent State University, Tashkent, Uzbekistan*

*** Ioffe Physicotechnical Institute, Russian Academy of Sciences, St. Petersburg, Russia*

Received October 30, 1999

Abstract—The postimplantation distribution of defects and dopant atoms in silicon samples ion-implanted with the rare-earth element ytterbium was studied for the first time. The radiation damage profile coincides with the profile of implanted ytterbium. *© 2000 MAIK "Nauka/Interperiodica".*

Ion implantation is the main method of doping used in the planar semiconductor technology, which combines incorporation of the dopant atoms into substrate with their diffusional spreading. Therefore, investigations of the process of defect formation during ion implantation, the resulting implant profiles, and the redistribution of dopants in the course of annealing are always of importance.

Below, we report on the first investigation of the distribution of postimplantation radiation defects in silicon samples ion-implanted with the rare-earth element ytterbium. We have also studied the profile of implanted ytterbium and its redistribution in the course of thermal annealing. The selection of ytterbium as the implant is explained by increasing fundamental and practical interest in doping silicon with rare-earth elements, which may serve as getters for fast-diffusing impurities and defects and increase the thermal and radiation stability of silicon-based structures [1, 2].

The radiation damage distribution in the ion-doped layer of silicon was determined by the UV reflectance technique. The depth–concentration profiles of implanted ytterbium were studied by the method of residual activity measurements upon the neutron activation. In both cases, the sequential layers were removed by anodic dissolution and their thicknesses were determined by ellipsometry.

Data of the UV reflectance measurements, in combination with the results of calculations using the model of direct collisions and the experimental implant depth–concentration profile allow the radiation defects generated in the course of the ion bombardment to be identified.

In this work, single-crystal silicon wafers (KEF-15) were implanted with Yb^+ ions at an energy of E = 70 keV and an ion beam current density of j = 10 μA/cm^2 to a dose of $Q = 10^{16}$ cm^{-2}.

The pattern of disorder (radiation defect distribution) and the depth–concentration profile of ^{173}Yb in silicon are presented in the figure. As seen, the position of maximum in the experimental implant profile coincides with that calculated by the Lindhard–Scharff–Schiott theory (calculated projected ion range $R_p \simeq$ 200 Å). A correlation between the distribution of defects and the implant depth–concentration profile is also evident. The maximum in the radiation damage distribution is somewhat closer to the surface than the peak of the implant profile, which is analogous to the case of phosphorus [3].

At a depth of the order of $2R_p$, the implant depth–concentration profile deviates from the Gauss distribution. At this depth, the curve of the radiation damage varies in a nonmonotonic manner.

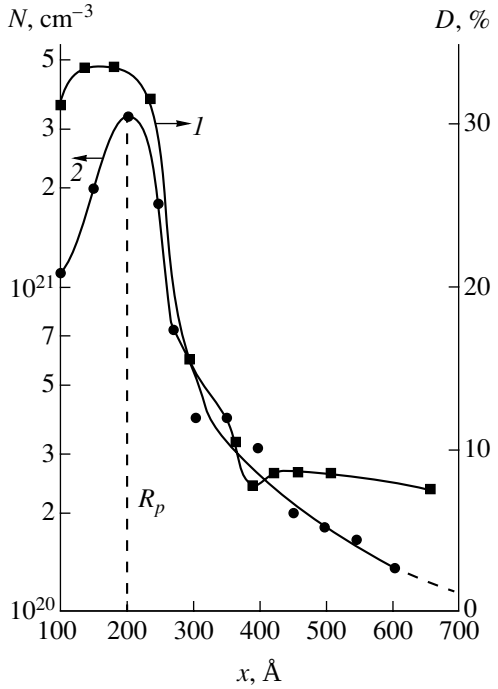

Depth profiles of (*1*) radiation defect density and (*2*) dopant concentration in a silicon single crystal implanted with $^{173}Yb^+$ ions.

1063-7850/00/2604-0326$20.00 © 2000 MAIK "Nauka/Interperiodica"

Based on the data available in the literature concerning the radiation defect identification, we may suggest that the surface layer of silicon ion-implanted with ytterbium comprises five regions. Region I is a near-surface layer with a thickness of 50–100 Å, which is characterized by a high degree of disorder. Unfortunately, the dominating type of defects in this region is unidentified. Region II, which extends from a depth of 100 to about 200 Å, exhibits a maximum disorder related to the ytterbium atoms incorporated into interstitial positions. Region III extends from 150 to 300 Å and is a layer corresponding to the calculated ion range $R_p \pm \Delta R_p$. Here, the density of defects exhibits a rapid drop and the UV reflectance spectra reveal no implanted atoms at the lattice sites. Region IV (300–450 Å) corresponds to the channeled impurity atoms (a similar region was revealed by the method of backscattering upon the channeling implantation of arsenic). Region V represents deeper layers with a small density residual defects formed by recoil atoms of silicon displaced as a result of the ion implantation.

During a high-temperature annealing (1200, 1220, and 1280°C for 2, 10, and 18 h) of the single-crystal silicon samples ion-doped with ytterbium to a dose of $Q = 10^{14}$–10^{16} cm^{-2}, the dopant exhibits out-diffusion from the implanted layer. As a result, all the dopant was found to segregate at the silicon surface and adsorb in the layer of SiO_2 formed as a result of the thermal treatment. No neutron-activated dopant atoms were revealed in silicon samples with this layer etched off by hydrofluoric acid.

These results will be refined by experiments employing a wide range of implantation doses and various (including low) annealing temperatures, which are currently in progress.

REFERENCES

1. D. É. Nazyrov, G. S. Kulikov, and A. R. Regel', *Silicon Doped with Rare-Earth Elements. A Preprint of the Ioffe Physicotechnical Institute* (Ioffe Physicotechnical Institute, Russian Academy of Sciences, Leningrad, 1977).
2. R. Sh. Malkovich and D. É. Nazyrov, Pis'ma Zh. Tekh. Fiz. **15**, 38 (1989) [Sov. Tech. Phys. Lett. **15**, 136 (1989)].
3. S. A. Goncharov and V. I. Sokolov, in *Proceedings of the All-Union Conference on Radiation Defects in Metals, Alma-Ata, 1983*, p. 9.

Translated by P. Pozdeev

Technical Physics Letters, Vol. 26, No. 4, 2000, pp. 328–329. Translated from Pis'ma v Zhurnal Tekhnicheskoĭ Fiziki, Vol. 26, No. 8, 2000, pp. 28–31.

Effect of Heat Treatment on the Properties of Erbium-Doped Silicon

S. I. Vlasov, D. É. Nazyrov, A. A. Iminov, and S. S. Khudaĭberdiev

Tashkent State University, Tashkent, Uzbekistan

Received October 30, 1999

Abstract—The effect of thermal treatment on the electrical properties of *n*-Si doped with the rare-earth element erbium during growth was studied for the first time. Annealing of the erbium-doped samples in air at 900–1200°C for 1–2 h, followed by quenching or slow cooling, leads to inhibition of the high-temperature defects. © *2000 MAIK "Nauka/Interperiodica".*

An important current task in the semiconductor materials science consists in increasing the thermal and radiation stability of silicon-based structures. In connection with this, there is increasing interest in doping silicon with rare-earth elements, which may improve the stability of silicon with respect to external factors [1–4]. In this context, it was of interest to study the properties of silicon doped with the rare-earth element erbium and their variation as a result of high-temperature processing.

Below, we report on the results of investigations of the interaction of erbium with the thermal treatment induced defects in *n*-Si.

The experiments were performed on the Czochralski-grown samples of *n*-Si with a resistivity of ~20 and 50 Ω cm doped with erbium during growth from melt. The erbium concentration, determined by the neutron-activation analysis, was 10^{15}–10^{17} cm^{-3}. The control samples were made of undoped silicon crystals grown under similar conditions and possessing close resistivities. All samples (representing $5 \times 10 \times 15$-mm plates) were ground with microparticle powders; cleaned by sequentially boiling in toluene, acetone, and an HCl–HNO_3 (3 : 1) solution mixture; etched with an SR-4 etching solution; and rinsed in deionized water. Then a Schottky barrier was created on each sample by depositing a gold film in vacuum onto substrates heated to <373 K.

The electrical properties of the samples were studied by measuring the isothermal relaxation of capacitance [5] and the photo emf distribution [6]. Deep levels situated in the lower part of the forbidden band of *n*-Si were probed by the optical recharge method. The degree of sample homogeneity with respect to resistivity was assessed by the surface photo emf distribution determined by scanning the sample surface with a focused intensity-modulated laser beam ($\lambda = 0.63$ μm; $P = 10$ mW; modulation frequency $f = 350$ Hz).

A comparison of the high-frequency plots of $(S/C_b)^2 \sim f(u)$ for the control (see figure, curve *1*) and erbium-doped (curve *2*) *n*-Si showed that the latter samples exhibit a significant scatter of the ionized impurity concentrations. The isothermal relaxation of capacitance measured for all samples in the temperature interval from 77 to 300 K showed no evidence of recharge ($N_d < 5 \times 10^{11}$ cm^{-3}). The thermal treatment of erbium-doped samples for 1–2 h in the temperature interval from 1273 to 1473 K, followed by quenching in oil or by slow cooling, led to the compensation of charged centers. As a result, the capacitance of Si⟨Er⟩ was independent of the applied voltage (i.e., $C_b \approx C_h$ [5, 7]) at temperatures up to ~80 K for the samples with an erbium concentration of ~10^{15} cm^{-3} and up to ~100 K for the samples doped to ~10^{17} cm^{-3}. The degree of compensation was higher in the rapidly cooled (quenched) samples than in the slowly cooled ones. The thermal treatment at 1173 K led to a decrease in the

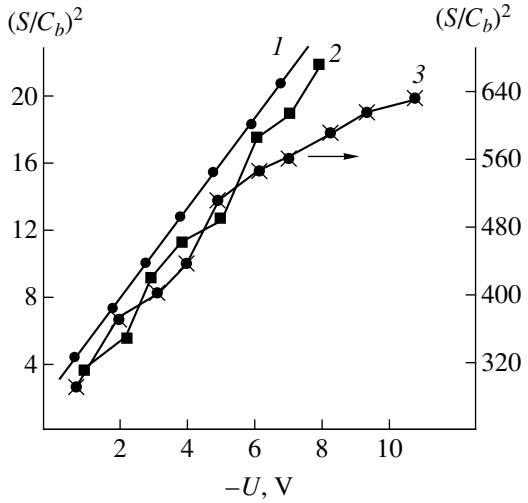

Typical high-frequency plots of $(S/C_b)^2 \sim f(u)$ for the (*1*) control (undoped) and (*2*) erbium-doped *n*-Si samples and (*3*) *n*-Si⟨Er⟩ samples upon heat-treatment.

1063-7850/00/2604-0328$20.00 © 2000 MAIK "Nauka/Interperiodica"

concentration of ionized centers (from 3×10^{14} to 2.6×10^{14} cm^{-3}). However, this was not accompanied by the formation of deep centers in the forbidden band ($N_d < 5 \times 10^{11}$ cm^{-3}). Therefore, we may suggest that erbium, like other rare-earth elements [3, 8, 9], forms shallow acceptor levels in the upper part of the forbidden band, which confirms the general acceptor nature of this dopant [3, 10, 11].

In the control (erbium-free) samples, the thermal treatment led to the formation of the following deep levels: E_c – (0.17–0.22) eV; E_c – 0.4 eV; E_c – 0.54 eV; E_v + 0.2 eV; and E_v + 4 eV. The parameters of these levels coincided with those reported in [12, 13] and their concentrations did not exceed 5×10^{13} cm^{-3}.

The recharge of deep centers in erbium-compensated *n*-Si samples could not be detected, although a low-temperature annealing (373 K; 15 min) removed the compensation produced by the high-temperature treatment at 1273–1473 K for 1 h. The low-temperature annealing resulted in the appearance of ionized centers with a concentration of $\sim 2 \times 10^{14}$ and $\sim 4 \times 10^{14}$ cm^{-3} in the samples slowly cooled and rapidly quenched upon heating, respectively.

The subsequent low-temperature treatment at 473 K, or even at 337 K, led to intensive recovery of the initial concentration of ionized centers.

Investigation of the photo emf distribution in erbium-doped *n*-Si revealed significant inhomogeneity of the surface resistivity of these samples, which is probably related to a nonuniform distribution of erbium atoms and aggregates. The depth–concentration profiles of the ionized centers in heat-treated Si⟨Er⟩ samples were inhomogeneous as well (see figure, curve *3*).

Thus, the doping of silicon with erbium leads to the inhibition of high-temperature defects. The higher the erbium concentration in silicon, the greater the degree of compensation and the inhibition of thermal defects. The inhibition of defects is probably related to the gettering effect of erbium, a rare-earth element [14], leading to the formation of erbium-defect complexes of the acceptor type.

REFERENCES

1. J. Mandelkorn, L. Schwartz, J. Broder, *et al.*, J. Appl. Phys. **35**, 2258 (1964).
2. N. T. Bagraev, L. S. Vlasenko, V. M. Volle, *et al.*, Zh. Tekh. Fiz. **54**, 917 (1984) [Sov. Phys. Tech. Phys. **29**, 547 (1984)].
3. D. É. Nazyrov, A. R. Regel', and G. S. Kulikov, *A Preprint of the Ioffe Physicotechnical Institute, USSR Acad. Sci.*, No. 1122 (Leningrad, 1987), pp. 1–56.
4. R. Sh. Malkovich and D. É. Nazyrov, Pis'ma Zh. Tekh. Fiz. **15**, 38 (1988) [Sov. Tech. Phys. Lett. **15**, 136 (1988)].
5. L. S. Berman and A. A. Lebedev, *Capacitance Spectroscopy of Deep Centers in Semiconductors* (Nauka, Leningrad, 1981).
6. L. P. Pavlov, *Methods for the Measurement of Parameters of Semiconductor Materials* (Vysshaya Shkola, Moscow, 1987).
7. L. S. Berman and S. I. Vlasov, Fiz. Tekh. Poluprovodn. (Leningrad) **12**, 559 (1978) [Sov. Phys. Semicond. **12**, 323 (1978)].
8. M. K. Bakhadyrkhanov and F. M. Talipov, Ukr. Fiz. Zh. (Russ. Ed.), No. 6, 5 (1992).
9. V. V. Petrov, V. S. Prosolovich, Yu. A. Karpov, and V. L. Kharchenko, Fiz. Tekh. Poluprovodn. (Leningrad) **20**, 1339 (1986) [Sov. Phys. Semicond. **20**, 844 (1986)].
10. D. É. Nazyrov, G. S. Kulikov, and R. Sh. Malkovich, Fiz. Tekh. Poluprovodn. (Leningrad) **25**, 1653 (1991) [Sov. Phys. Semicond. **25**, 997 (1991)].
11. S. Z. Zaĭnabidinov, D. É. Nazyrov, A. Zh. Akbarov, *et al.*, Pis'ma Zh. Tekh. Fiz. **24**, 68 (1998) [Tech. Phys. Lett. **24**, 71 (1998)].
12. K. P. Abdurakhmanov, T. Sherimbetov, B. A. Kotov, *et al.*, Fiz. Tekh. Poluprovodn. (Leningrad) **20**, 1339 (1986); Dep. VINITI No. P4155.
13. K. P. Abdurakhmanov, M. D. Khodzhaev, T. A. Umarov, and A. T. Teshabaev, Izv. Akad. Nauk UzSSR **3**, 64 (1986).
14. R. Sh. Malkovich and D. É. Nazyrov, Pis'ma Zh. Tekh. Fiz. **15**, 38 (1989) [Sov. Tech. Phys. Lett. **15**, 136 (1989)].

Translated by P. Pozdeev

Technical Physics Letters, Vol. 26, No. 4, 2000, pp. 330–331. Translated from Pis'ma v Zhurnal Tekhnicheskoĭ Fiziki, Vol. 26, No. 8, 2000, pp. 32–36.

Anomalous Resistivity of Sodium–Lithium–Niobium–Tantalum Ceramics

I. P. Raevskiĭ*, M. N. Palatnikov*, V. A. Sandler*, and M. A. Malitskaya**

** Institute of Physics, Rostov State University, Rostov-on-Don, Russia*

*** Institute of the Chemistry and Technology of Rare Elements and Mineral Raw Materials, Kola Scientific Center, Russian Academy of Sciences, Apatity, Russia*

Received October 22, 1999

Abstract—The electric resistance R of the samples of a $Na_{0.88}Li_{0.12}Nb_{0.5}Ta_{0.5}O_3$ ferroelectric ceramic composition with the electron conductivity increased by thermal reduction in vacuum exhibit anomalous temperature variation of the posistor type in the temperature region of 350–400°C, where the nonreduced samples exhibit transition to the state with superionic conductivity. The $R(T)$ anomaly was observed during the electrical measurements both in air and in vacuum. The effect depends on the degree of material reduction and the measurement frequency, reaching 4–5 orders of magnitude for the dc measurements in samples with maximum conductivity. It is suggested that the $R(T)$ anomaly is localized in the near-electrode layer and is related to a mutual influence of the electron and ion transport processes. © *2000 MAIK "Nauka/Interperiodica".*

Thermally sensitive resistors of the posistor type, with the electric resistance R sharply increasing within certain temperature interval, are widely used in various devises such as temperature sensors, self-controlled heating elements, current and voltage limiters, etc. [1, 2]. Most frequently employed are the posistors based on a $BaTiO_3$ ferroelectric ceramic semiconductor compositions, in which the region of positive temperature coefficient of resistance (PTCR) is observed near the ferroelectric Curie temperature.

The posistor effect in ferroelectric ceramics is due to the barrier grain-boundary layers, the resistance of which is strongly dependent on the permittivity [1, 2]. A significant disadvantage of the ferroelectric posistors is their inability to operate in a medium with low partial oxygen pressure, where the barrier layers exhibit degradation [2, 3]. Therefore, it is important to search for new physical systems with PTCR, which would serve a base for the development of posistors free of this disadvantage. Below we report on the discovery of an anomalous resistance behavior of the posistor type in $Na_{1-x}Li_xNb_{1-y}Ta_yO_3$ (NLNT) solid solution semiconductor ceramic compositions. The posistor effect was observed in the NLNT samples measured both in air and in vacuum.

The solid solution semiconductor ceramic compositions $Na_{1-x}Li_xNb_{1-y}Ta_yO_3$ with $x = 0.12$ and $y = 0.50$ (NLNT 12/50) were obtained by solid-state synthesis, followed by annealing without compression. The X-ray diffraction measurements showed that all samples had a single-phase structure of the perovskite type. The samples for the electrical measurements had a shape of disks with a diameter of 10 mm and a thickness of 1 mm. After polishing, the samples were provided with platinum or silver electrodes either formed by metal paste fusion or deposited by magnetron sputtering. The resistance measurements were performed in the dc or ac modes on the samples continuously heated or cooled at a rate of 2–5 K/min.

Upon the thermal reduction in vacuum at a residual pressure of 10^{-3} Torr and a temperature of 650–750°C, the electric resistance of NLNT 12/50 samples decreased by several orders of magnitude and the ceramics acquired semiconductor properties. The reduced samples exhibited *n*-type conductivity and had a color varying from dark-blue to black. These observations indicated that the semiconductor properties of NLNT ceramics upon vacuum reduction (similarly to the other oxides with perovskite structures) are related to a high concentration of oxygen vacancies involved in donor centers [4].

The plots of dc resistance R versus temperature for the NLNT 12/50 samples upon vacuum reduction measured on heating both in vacuum and in air exhibit a PTCR region in the temperature interval from 350 to 400°C. This region was also observed on cooling, with a temperature hysteresis reaching 15–20 K (figure, curves *1*, *2*). The measurements in air involved partial oxidation of the samples, which resulted in a gradual increase of the sample resistance from one measurement cycle to another, but the difference between R values observed upon heating and subsequent cooling was always markedly lower than the jump of R in the PTCR region. This observation, and the fact that PTCR region is observed during the measurements in vacuum (where no oxidation takes place) is evidence that the PTCR manifestation in vacuum-reduced NLNT ceramics is not caused by the sample oxidation.

1063-7850/00/2604-0330$20.00 © 2000 MAIK "Nauka/Interperiodica"

The NLNT 12/50 ferroelectric ceramic composition reduced in vacuum exhibits no phase transitions at temperatures close to the PTCR region [5]. Therefore, the nature of the posistor effect in this system is apparently different from that in other semiconductor oxide ceramics with perovskite structures [1, 2, 6]. At the same time, the nonreduced NLNT 12/50 samples exhibit a transition to the state with superionic conductivity at 400–450°C, which is accompanied by a jumplike increase in conductivity by 1–2 orders of magnitude [7]. Figure (curve *3*) shows the temperature variation of the bulk resistance of a nonreduced NLNT 12/50 sample determined from the results of dispersion analysis of the complex admittance [7], which allowed the near-electrode layer resistance to be excluded. The lower branch of this curve corresponds to the state with superionic conductivity, and the upper branch represents the state with mixed electron and ion conductivity (the relative contribution of the latter component increasing with the temperature). As seen from this curve, the PTCR region in the $R(T)$ curve of the reduced NLNT ceramics approximately coincides with the region of temperature hysteresis for the transition to the state with superionic conductivity.

It should be noted that, according to the theory of superionic semiconductors, there are certain values of the ion–electron interaction parameters for which a sharp change in the ion concentration may lead to a significant variation in the concentration of electrons [8]. In the general case, this variation is related to the formation of vacancy defects and partial disturbance of the periodic structure of the crystal lattice.

The $R(T)$ anomaly observed in reduced NLNT 12/50 ceramics decreases with increasing frequency of the measuring electric field, the effect being already strongly pronounced when the frequency is increased above 50–100 Hz. The jump in the sample resistance observed at 1000 Hz drops by a factor of 30–100 as compared to that observed at 50 Hz. These observations indicate that the PTCR manifestations are most probably related to the near-electrode layers. A possible reason is that the ion–electron interaction is most pronounced in the electric double layer formed near the electrodes [7, 8].

Thus, we have established that the samples of $Na_{0.88}Li_{0.12}Nb_{0.5}Ta_{0.5}O_3$ ceramic composition with high electron conductivity exhibit anomalous temperature variation of the posistor type in the temperature region of 350–400°C, where the nonreduced samples exhibit transition to the state with superionic conductivity. The anomaly is reproduced both in air and in vacuum, which opens way to the development of posistors based on the $Na_{0.88}Li_{0.12}Nb_{0.5}Ta_{0.5}O_3$ ceramics, which would be capable of operating in the media with low partial oxygen pressure.

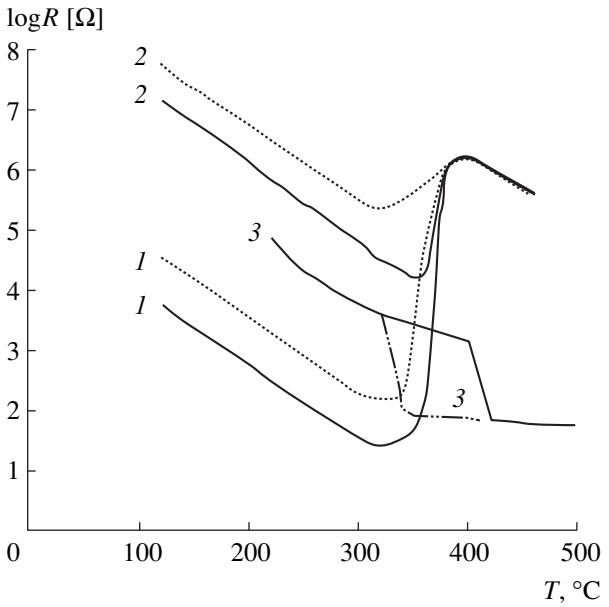

Temperature variation of the resistance R measured in air in the dc mode for two samples of vacuum-reduced $Na_{0.88}Li_{0.12}Nb_{0.5}Ta_{0.5}O_3$ ceramics with different initial (room-temperature) resistances (curves *1* and *2*). Curve *3* shows the temperature variation of the bulk resistance of a nonreduced sample of the same ceramics determined from the results of dispersion analysis of the complex admittance measured in the frequency range from 10 Hz to 10 MHz. Solid lines correspond to heating, and dashed lines–to cooling of the samples.

The work was partly supported by the Russian Foundation for Basic Research, projects nos. 99-02-17575 and 97-03-33601.

REFERENCES

1. I. T. Sheftel', *Thermoresistors* (Nauka, Moscow, 1973).
2. *Barium Titanate Based Semiconductors* [Translated from Japanese] (Énergoizdat, Moscow, 1982).
3. Kh. S. Valeev and V. B. Kvaskov, *Nonlinear Metal Oxide Semiconductors* (Énergoatomizdat, Moscow, 1983).
4. I. P. Raevskiĭ, S. M. Maksimov, A. V. Fisenko, *et al.*, J. Phys.: Condens. Matter **10**, 6705 (1998).
5. M. N. Palatnikov, V. A. Sandler, Yu. A. Serebyarkov, *et al.*, Neorg. Mater. **33**, 1135 (1997).
6. I. P. Raevskiĭ, A. N. Pavlov, and O. I. Prokopalo, Izv. Akad. Nauk SSSR, Ser. Fiz. **51**, 2262 (1987).
7. M. N. Palatnikov, V. A. Sandler, Yu. A. Serebryakov, *et al.*, Neorg. Mater. **28**, 1995 (1998).
8. Yu. A. Gurevich and Yu. I. Kharkats, Itogi Nauki Tekhn., Ser. Khim. Tverd. Tela (VINITI, Moscow) **4**, 128 (1987).

Translated by P. Pozdeev

Technical Physics Letters, Vol. 26, No. 4, 2000, pp. 332–333. Translated from Pis'ma v Zhurnal Tekhnicheskoĭ Fiziki, Vol. 26, No. 8, 2000, pp. 37–40.

Growth of Hollow Annular Zinc Oxide Structures

A. Kh. Abduev, A. K. Akhmedov, V. G. Baryshnikov, and Sh. O. Shakhshaev

Institute of Physics, Dagestan Scientific Center, Russian Academy of Sciences, Makhachkala, Dagestan, Russia

Received May 25, 1999

Abstract—The conditions and mechanisms of the growth of hollow crystals, dendrite structures, and whiskers of zinc oxide during the annealing of pressed zinc oxide–carbon mixtures were studied. The growth of hollow structures is due to the interaction of reagents in pressed tablets, which is accompanied by the formation of a gas-impermeable external ZnO shell and the transport of Zn vapor and CO_2 along the growing tube. Orientation of the hollow crystals is determined by the direction of Zn vapor transport. The process was modeled by the Zn vapor emission from a Knudsen effusion cell. *© 2000 MAIK "Nauka/Interperiodica".*

The well-known models of whisker growth [1, 2] were used in a number of works to describe the growth of whiskers, hollow dendrites, and annular crystals of zinc oxide under various conditions [3–8]. A common assumption in all the models employed was that the reagents are supplied to the growth surface from outside.

In this work, we have studied the formation of hollow crystals and dendrite structures during the annealing of pressed tablets of ZnO containing various amounts of carbon. The tablets were prepared by cold pressing (P = 0.15 GPa) of thoroughly mixed ZnO and carbon powders. The crystal structures were grown by uniformly heating the tablets in an open furnace up to 1700 K. The results of observations showed that hollow crystals and dendrite structures were nucleated at a temperature of about 1450 K. Also visually observed was the emission of ZnO vapor from the growing hollow structure at a velocity of 0.1 mm/s. The type of growing structures depends on the carbon content in the mixture, which is illustrated in Fig. 1.

1. The sample mixtures with a carbon content of about 3% exhibit the growth of straight hollow annular crystals with a diameter of 0.1–1.0 mm and a length of up to a few dozen centimeters (Fig. 1a). The experiments showed that the length of a growing hollow crystal is limited only by the initial tablet volume. Figure 1b shows a micrograph of the end of a hollow crystal. Overgrowth of the channel is usually caused by a change in the reagent flow regime caused by switching off the furnace or by the source exhaustion. The X-ray diffraction data indicated that the tube walls are formed by crystals oriented in the (0001) direction. The growth orientation may change upon alteration of the direction of vapor efflux (for example, on reaching the annealing chamber wall).

2. Increasing the carbon content to 5% leads to the growth of hollow dendrites of complicated shape, with an external diameter of up to 10 mm (Fig. 1c). A micrograph of the dendrite cross section (Fig. 2) reveals that the walls are composed of randomly oriented filament crystals (whiskers). The whiskers have a cross-section

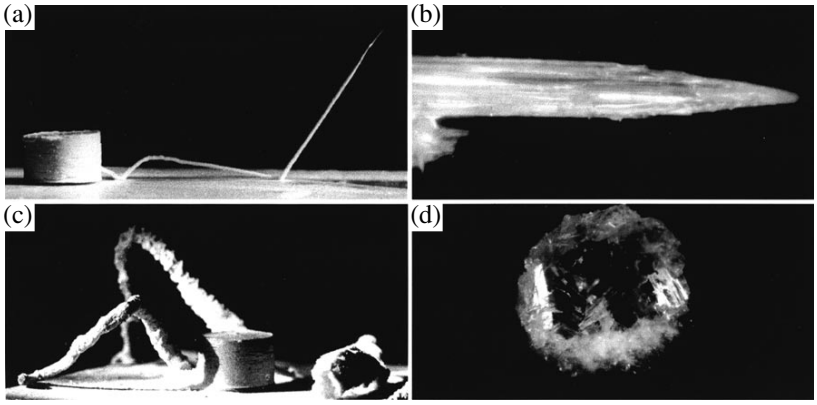

Fig. 1. Micrographs showing (a) a hollow annular ZnO crystal, (b) the end part of this crystal, (c) a dendrite structure and (d) a cross-section of this dendrite.

1063-7850/00/2604-0332$20.00 © 2000 MAIK "Nauka/Interperiodica"

diameter of 10 μm and a length of up to 1000 μm. The crystals exhibit faceting characteristic of the hexagonal system and are oriented in the (0001) direction.

3. The results of annealing of a pressed tablet significantly depend on the content of carbon in ZnO. A feature in common for all the compositions studied was the formation of a compact shell on the tablet surface, which hindered the escape of Zn and CO_2 vapors through the tablet walls.

The partial loss of material from tablets results in the formation of a porous ceramic structure, with the degree of porosity decreasing with increasing carbon content in the initial mixture. In excess of carbon, the annealing results in the formation of a compact polycrystalline shell of zinc oxide with a wall thickness of about 2 mm.

The formation of hollow structures is related to an excess pressure of CO_2 and Zn vapor (the products of reaction between ZnO and carbon). Zn emerging at the surface of the tablet is oxidized to form a compact shell. The further increase in pressure inside the tablet leads to local breakage of the shell and gives rise to the hollow structure formation.

In order to simulate the process of hollow structure growth from tablets, we have studied the process of zinc vapor emission from a Knudsen effusion cell heated to the zinc boiling temperature. The emission of zinc vapors was accompanied by their burning in a torch with the formation of a hollow annular structure (Fig. 2). The walls of the hollow structures formed at a comparatively low ambient temperature were composed of finely dispersed zinc oxide particles oriented predominantly in the (0001) direction, rather than of whiskers.

Measurements of the temperature inside the tablet showed any no significant difference from the furnace temperature, which is explained by close values of the enthalpies of zinc oxide and carbon oxide formation (H = –350.8 and –3393.5 kJ/mol, respectively). Therefore, virtually all the energy gained in the CO_2 formation upon burning of the Zn vapors is liberated at the end of the growing tube.

Interpretation of the above growth process requires no recourse to some diffusion model, since all the material is supplied directly to the growth surface from the gas phase in the tube. The degrees of supersaturation achieved on this surface markedly exceed the levels adopted in the vapor–liquid–crystal (VLC) growth model. As for the diffusion model, it should be noted that our experimental conditions excluded any possibility for Zn or ZnO vapors to appear on the side surface, since the zinc vapors emitted from the tube end are oxidized and either deposited at the tube edge or carried away with a convective flow.

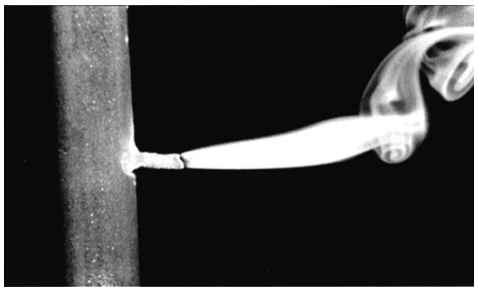

Fig. 2. A micrograph of a hollow annular ZnO formed during the emission of zinc vapors from a Knudsen effusion cell.

The transition from the growth of hollow crystals to dendrites is observed upon increasing the content of carbon in the initial mixture and, hence, is related to increasing efflux of zinc vapor from the tablet. The displacement of oxygen by the zinc vapors leads to increase in the tube diameter. High degrees of supersaturation result in the appearance of a large number of new crystallization centers and give rise to the intensive growth of randomly oriented whiskers.

Thus, we have performed direct observations of the process of direct supply of a reagent (zinc vapors) via a hollow crystal channel to the growth surface. Park and Renolds [4] suggested that the heating of zinc in air leads to the formation of an oxide shell, breakage of this film on reaching the boiling temperature of zinc, the emission of zinc vapors, and the growth of hollow annular crystals. Our direct observations and simple estimates showed that breakage of the oxide shell is accompanied by the ejection of numerous fine droplets of zinc rather than by the formation of zinc vapors only. These droplets exhibit repeated surface oxidation, which leads to the growth of ZnO tubes.

REFERENCES

1. E. I. Givargizov, *The Growth of Filament and Platelike Crystals from Vapor Phase* (Nauka, Moscow, 1977).
2. G. V. Berezhkova, *Filament Crystals* (Nauka, Moscow, 1969).
3. M. Ishii and H. Hashimoto, Jpn. J. Appl. Phys. **8**, 1107 (1969).
4. Y. S. Park and D. C. Renolds, Appl. Phys. **38**, 756 (1967).
5. I. Kubo, Jpn. J. Appl. Phys. **4**, 225 (1965).
6. R. B. Sharma, J. Appl. Phys. **41**, 1866 (1970).
7. S. D. Sharma and Subhash C. Kashyap, J. Appl. Phys. **42**, 5302 (1971).
8. H. Iwanaga and N. Shibata, J. Cryst. Growth **24-25**, 357 (1974).

Translated by P. Pozdeev

Technical Physics Letters, Vol. 26, No. 4, 2000, pp. 334–336. Translated from Pis'ma v Zhurnal Tekhnicheskoĭ Fiziki, Vol. 26, No. 8, 2000, pp. 41–46.

Long-Wavelength Infrared Cascade Laser with Coherent Transport of Electrons

E. I. Golant and A. B. Pashkovskiĭ

Istok State Research and Production Enterprise, Fryazino, Moscow oblast, Russia

Received November 26, 1999

Abstract—Possible ways to overcome difficulties encountered in the creation of cascade lasers with collisionless tunneling of electrons are discussed. A structure of an IR laser using a single three-barrier structure and capable of working at a frequency of 4.5 THz is proposed. *© 2000 MAIK "Nauka/Interperiodica".*

The recent progress in the developing a laser operating in the far IR spectral range (5–12 μm) is based on the new type of lasers implementing electron transitions between the dimensional quantization levels of the semiconductor nanostructures with AlInAs barriers and GaInAs wells—the so-called quantum cascade (QC) lasers [1–3]. These lasers can be applied for military purposes, environmental monitoring, and medical diagnostics. However, Scamacio *et al.* [3] demonstrated that development of the QC lasers for the long-wavelength part of the spectrum encounters principal difficulties, in particular, a substantial increase in the start-up current density. However, previously [4], we have demonstrated the basic possibility of fabricating a quantum cascade laser using a coherent (collisionless) electron transport at the frequencies about 30 THz ($\lambda \approx 10$ μm). This laser differs from the above QC lasers by the physical principle (tunneling mechanism), by the structure involving a substantially thinner (in the units of atomic layers) potential barrier of the main quantum structure, and, in addition, by substantially higher quantum efficiency (up to 66% per cell) [5].

This work is aimed at the analysis of the problems making it difficult to decrease the frequency of the coherent QC lasers and to increase the frequency of the coherent resonance tunneling flight diodes (RTFD) and the methods of their solving. In particular, we propose a structure of the coherent quantum laser with a lasing frequency of 4.5 THz. Thus, we discuss a basic possibility of spanning the frequency range from a few gigahertz to tens of terahertz with the use of the active semiconductor devices based on nanostructures with coherent transport of electrons.

The first frequency limitation for both coherent lasers and coherent RTFDs with a two-barrier injector results from the requirement of the coherence of tunneling. This limitation is related to the electron lifetime on the resonance level $\tau \approx \hbar/\Gamma$, where Γ is the width of the resonance level. The lifetime must be shorter than the characteristic relaxation time of electrons with respect to momentum τ_p (with an allowance for all mechanisms of scattering). The electron lifetime at the upper resonance level, which is always broader than the lower one in two- or three-barrier structures, plays the main role in the regime of small signal (the estimates in [4, 6, 7] were done under this approximation), whereas the lifetime at the lower level is the most important parameter for the regime of strong signal.

The influence of the alternating component of the space charge is the second important limitation for application of the two-barrier resonance tunneling structures (TBRTS) in both QC lasers and RTFDs [8]. This limitation does not allow the output frequency of RTFDs to be increased substantially with the use of resonance transitions in a quantum injector with very narrow quasilevels.

The third limitation, which is especially important for the lasers in which the electromagnetic wave propagates along the boundaries of the heterojunction, is related to the conductivity losses that increase drastically with decreasing frequency (as ω^{-2} under the relaxation time approximation).

It was demonstrated earlier [4] that in a structurally perfect GaAs with the concentration of electrons $n = 10^{17}$ cm^{-3}, mobility $\mu \approx 9.6 \times 10^3$ cm^2/(V s), relaxation time $\tau_p \approx 4 \times 10^{-13}$ s, and the characteristic size of the active area (quantum well) $a = 100$ Å at $T = 77$ K and a frequency of 30 THz, the generation of the signal is possible if the active conductivity of the structure σ_a meets the condition: $-\sigma_a \geq 10$ S/cm. At the same time, the passage to a frequency of 10 THz ($\lambda = 30$ μm, recalling that the area of losses is proportional to the wavelength) at $n = 10^{17}$ cm^{-3} implies that $\sigma_a \geq 270$ S/cm, which is several times higher than the permissible (with respect to the alternating space charge) value $0.7\omega\varepsilon \approx 50$ S/cm [8]. On the other hand, simple estimates show that the possibility of reducing losses by means of lowering the electron concentration encounters the limitation on the lifetime at the resonance levels.

1063-7850/00/2604-0334$20.00 © 2000 MAIK "Nauka/Interperiodica"

There are at least two ways to bypass these difficulties. The first (and, possibly, the most promising) is related to the use of materials with narrower bandgaps, lower effective mass, and higher motility and, hence, with substantially longer relaxation time with respect to momentum. In particular, Brown *et al.* [9] obtained maximum lasing frequencies for InAs-based RTFD. For a two-barrier laser structure with $n = 10^{17}$ cm^{-3} and $a = 100$ Å at $T = 77$ K, the calculations yield the following condition of lasing at a frequency of $\nu = 10$ THz: $\sigma_a \geq 7$ S/cm.

As mentioned above, the strong signal regime poses a stricter (than in [4, 6, 7]) requirement to the coherence of electrons at the narrow lower level of TBRTS. Calculations for this practically important regime show that using the narrow-bandgap InAs is insufficient to solve the problem of substantial reduction (to less than 10 THz) in the frequency of TBRTS-based coherent lasers. This problem can be solved in another way—by using resonance transitions between the split levels of the three-barrier InAs-based structures (Fig. 1).

Figure 2 shows the results of calculations of the integral active conductivity according to the model [10] for an asymmetric three-barrier structure with the concentration of electrons $n = 10^{16}$ cm^{-3} at a temperature of $T = 77$ K with an allowance for the Fermi distribution of electrons at the input of the structure. The widths of both quantum wells are taken equal $a = l = 150$ Å, the thicknesses of heterobarriers are 11, 5.5, and 16.5 Å, and their height is 2 eV (the position of the first resonance level in a two-barrier structure with 11-Å barriers is $\varepsilon = 60.3$ meV). Note that the properties of superthin heterobarriers are insufficiently studied and the model with barriers of the same height that we use is a rather rough approximation when the width of the barriers is about several (or even one) atomic layers. However, two-barrier quantum structures with the barrier thicknesses of several atomic layers (their exact height is certainly unknown) have been already fabricated [9]. Note that a superthin and high middle barrier is basically equivalent to a low and sufficiently wide (about ten atomic layers) barrier of the same power, which can be easily produced experimentally. The bottom step of the conduction band at the first and the second barriers ($U = 65$ meV) is chosen so as to provide that the first resonance level is lower and the second one is higher than the bottom of the conduction band at the input of the three-barrier quantum structure (TBQS). The bottom step of the conduction band at the third barrier $U_3 = 45$ meV is selected to provide the maximum integral high-frequency conductivity of the TBQS. (The width of the lower resonance level Γ is close to that of the upper level and is about 0.6 meV. The corresponding lifetime at the level is almost 5 times shorter than the characteristic electron relaxation time with respect to momentum.)

It is seen that the conductivity attains the maximum value $\sigma_a = -7.3$ S/cm at the frequency $\nu = 4.5$ THz. On the one hand, this value is several times higher than the lasing threshold (for the given structure, concentration, and frequency, the condition $\sigma_a \geq 2$ S/cm must be met). On the other hand, the conductivity is several times lower than the value $0.7\omega\varepsilon \approx 20$ S/cm, which means that in the given regime the alternating component of the space charge can be neglected. Thus, it is demonstrated that the lasing frequency of a coherent quantum laser on one three-barrier structure operated in the strong signal regime can be lowered to 4.5 THz. The analysis is performed within the framework of the adopted physical mechanism of the QS laser operation. It is natural that the sequential cascading of the active three-barrier nanostructures [1–3] can substantially increase the quantum efficiency and the output power of the laser.

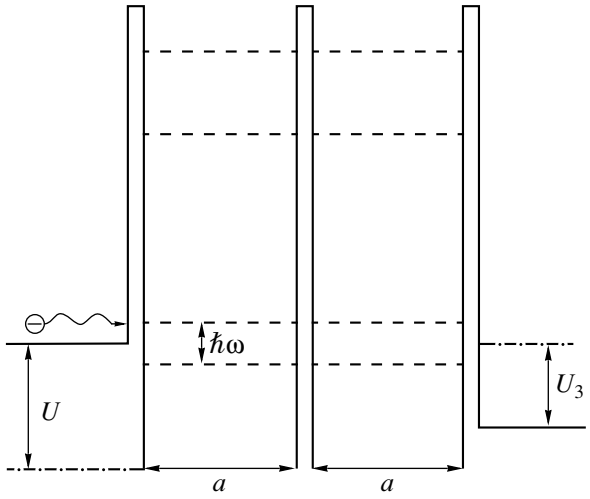

Fig. 1. A schematic band diagram of the three-barrier structure under consideration.

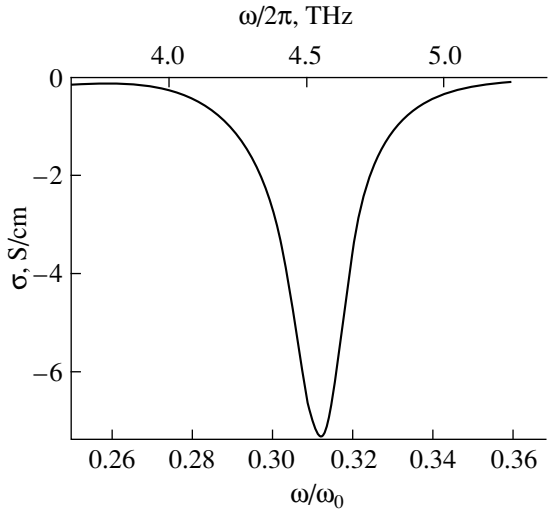

Fig. 2. The dependence of the active conductivity on the normalized frequency ω/ω_0 for the three-barrier structure under consideration ($\omega_0 = \varepsilon/\hbar$, $\varepsilon = 60.3$ meV).

This work was supported in part by the Russian Foundation for Basic Research (project no. 97-02-16652) and the Scientific Council on the Program "Physics of Solid State Nanostructures" (project no. 97-1094).

REFERENCES

1. J. Faist, A. Tredicicci, F. Capasso, *et al.*, IEEE J. Quant. Electron. **34**, 336 (1998).
2. C. Sirtori, J. Faist, F. Capasso, *et al.*, Appl. Phys. Lett. **69**, 2810 (1996).
3. G. Scamarcio, C. Gmachi, F. Capasso, *et al.*, Semicond. Sci. Technol. **13**, 1333 (1998).
4. E. I. Golant, A. B. Pashkovskiĭ, and A. S. Tager, Pis'ma Zh. Tekh. Fiz. **20**, 74 (1994) [Tech. Phys. Lett. **20**, 886 (1994)].
5. E. I. Golant and A. B. Pashkovskiĭ, Zh. Éksp. Teor. Fiz. **112**, 237 (1997) [JETP **85**, 130 (1997)].
6. É. A. Gel'vich, E. I. Golant, A. B. Pashkovskiĭ, and V. P. Sazonov, Pis'ma Zh. Tekh. Fiz. **25**, 7 (1999) [Tech. Phys. Lett. **25**, 382 (1999)].
7. É. A. Gel'vich, E. I. Golant, A. B. Pashkovskiĭ, and V. P. Sazonov, Pis'ma Zh. Tekh. Fiz. **26** (2000) (in press).
8. A. B. Pashkovskiĭ, Pis'ma Zh. Éksp. Teor. Fiz. **64**, 829 (1996) [JETP Lett. **64**, 884 (1996)].
9. E. R. Brown, J. R. Soderstrom, C. D. Parker, *et al.*, Appl. Phys. Lett. **58**, 2291 (1991).
10. E. I. Golant and A. B. Pashkovskiĭ, Pis'ma Zh. Éksp. Teor. Fiz. **67**, 372 (1998) [JETP **67**, 394 (1998)].

Translated by A. Chikishev

Technical Physics Letters, Vol. 26, No. 4, 2000, pp. 337–340. Translated from Pis'ma v Zhurnal Tekhnicheskoĭ Fiziki, Vol. 26, No. 8, 2000, pp. 47–55.

Thermoelectron Clouds and Charge on Dust Particles

S. I. Yakovlenko

Institute of General Physics, Russian Academy of Sciences, Moscow, Russia

Received July 12, 1999

Abstract—The properties of equilibrium thermoelectron clouds surrounding dust particles with large surface charge density were studied based on a rigorous solution of the Poisson–Boltzmann equation in a planar case. According to this theory, an equilibrium charge of a particle is markedly lower than the values obtained in the experiment. It is suggested that the thermoemissive dust plasma studied in experiments is supercooled with respect to the degree of ionization. © *2000 MAIK "Nauka/Interperiodica".*

Introduction. In recent years, considerable attention was drawn to the properties of dust plasma formed as a result of the thermoelectron emission from dust particles [1–5]. An important problem is related to determining the equilibrium distribution of electron clouds in these systems. At a large surface charge density on a dust particle, the system can be described using a planar model, for which the Poisson–Boltzmann equation can be rigorously solved and the equilibrium charge distribution in the thermoelectron cloud can be determined.

Poisson–Boltzmann equation. Let the electron gas over a flat solid surface be formed as a result of the thermoelectron emission from this solid at a temperature T. In order to describe the distribution of potential ϕ, electric field strength $\mathbf{F} = -\nabla\phi$, and charge density eN_e, we have to solve the Poisson equation with a charge density defined by the Boltzmann distribution $N_e = N_{e1}\exp(e\phi)$. Here N_{e1} is the electron density at the point of zero potential; the sign of the exponent takes into account the negative charge of electron. In the general case, the Poisson–Boltzmann equation has the following form:

$$\Delta\phi = 4\pi e^2 N_{e1}\exp(e\phi).$$

Let the lengths be measured in units of $d = 8\pi e^2/T$ and select zero potential at the point where $(8\pi e^2/T)^3 N_{e1} = 1$. We will also use dimensionless potential φ, field strength $\mathbf{E}$, and electron density n_e defined by the relationships $\varphi = \phi e/T$, $\mathbf{E} = \mathbf{F}ed/T = \mathbf{F}T^2/8\pi e$, and $n_e = (8\pi e^2/T)^3 N_e$. Then the Poisson–Boltzmann equation in the planar case, where all quantities depend on a single dimensionless coordinate x (measured along the corresponding axis perpendicular to the charged plane) acquires the following form:

$$d^2\varphi/dx^2 = (1/2)\exp(\varphi), \quad E = -d\varphi/dx,$$
$$n_e = \exp(\varphi).$$

Boundary conditions and classification of solutions. In solving problems of this kind for a planar or spherically-symmetric geometry, the boundary conditions are usually selected so as to provide for the zero values of both potential and field strength at some point [4–6].

However, in the general case, the first boundary condition should be selected in the form of a positive charge density σ on the wall. This condition determines the field strength at the wall $F_0 = F(x = 0)$, $E_0 = E(x = 0)$, which corresponds to the field strength in a planar capacitor: $F_0 = 4\pi\sigma$ or $\sigma d^2/e = 2E_0$. Below we will solve the problem in this very formulation.

The second boundary condition for the case of compensated charge of the plane (see below) will be determined at some point a_0, where the field strength is zero because the charge of the plane is fully compensated by the charge of electrons: $E(a_0) = 0$.

The order of the Poisson–Boltzmann equation can be reduced by considering the field strength as a function of the potential $EdE/d\varphi = (1/2)\exp(\varphi)$. The first integration yields a relationship between the field strength and the potential: $E = (\exp(\varphi) + E_1^2 - 1)^{1/2}$. Here, E_1 is the electric field strength at a point $x = a_1$, where the potential is zero $\varphi(a_1) = 0$ and the dimensionless electron density is unity.

The final equation

$$-d\varphi/dx = (\exp(\varphi) + E_1^2 - 1)^{1/2}$$

has solutions of three types, which correspond to different physical problems. These cases are as follows.

For $E_1 > 1$, the field strength never takes the zero value. This situation corresponds to the case when the charge of the plane is not compensated by the charge of electrons.

For $E_1 = 1$, the field strength is zero at $\varphi = -\infty$. This corresponds to an electron cloud created by a single plane, with the zero field strength at an infinite distance from the plane ($a_0 \longrightarrow \infty$).

1063-7850/00/2604-0337$20.00 © 2000 MAIK "Nauka/Interperiodica"

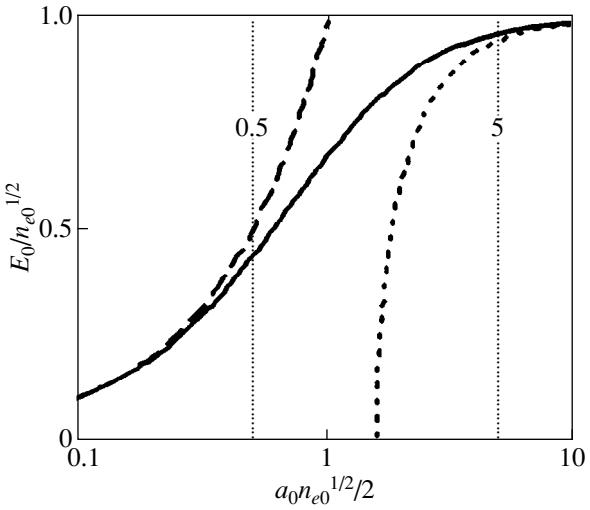

Fig. 1. The plot of reduced field strength on the wall $\varepsilon = E_0/n_{e0}^{1/2}$ vs. reduced distance between walls $\alpha = a_0 n_{e0}^{1/2}$ (solid line) in comparison with the results of calculation using approximate expressions for large distances $\varepsilon = (1 - (\pi/2\alpha)^2)^{1/2}$, ($\alpha \longrightarrow \infty$) (dotted line) and small distances $\varepsilon = \alpha$, ($\alpha \longrightarrow 0$) (dashed line), when electrons are "squeezed out" on the walls.

For $E_1 < 1$, the field strength is zero at a finite potential $\varphi_1 = 2\ln(1 - E_1^2)$. This corresponds, for example, to an electron cloud created between two identical charged planes, with the zero field strength at a point a_0 corresponding to half the distance between the planes.

Single charged plane. Integrating equation $-d\varphi/dx = \exp(\varphi/2)$, we obtain

$$\varphi(x) = 2\ln[2E_0/(xE_0 + 2)],$$

$$E(x) = 2E_0/(xE_0 + 2), \quad n_e(x) = [2E_0/(xE_0 + 2)]^2.$$

The potential becomes zero, while the field strength and the electron density acquire the unit values, at a point $a_1 = 2(1 - 1/E_0)$, which may occur both to the left and to the right of the charged plane.

The value $2/E_0$ represents the characteristic width of the region of decay in the electron density and field strength. At a large charge density on the wall, the layer of electrons compensating this charge becomes narrow and the region of major variation of the parameters of electron cloud can be considered within the framework of a planar model even for a dust particle of complicated shape.

Let us express the field strength E_0 at the surface in terms of thermionic characteristics. The thermoelectron current density is determined by the Richardson–Dushman formula: $j = A\exp(-b/T)$ with $A = 4\pi m_e e/h^3 = 120$ A/cm^2. Here b is the electron work function of the wall and $h = 2\pi\hbar$ is the Planck constant. Assuming that the thermoelectron emission flux is equal to the reverse thermal current, $j = e(T/2\pi m_e)^{1/2} N_{e0}$, we may determine the electron density at the boundary:

$$N_{e0} = N(b)\vartheta^{3/2}\exp(-1/\vartheta),$$

$$N(b) = 2(m_e b/2\pi h^2)^{3/2} = 6.04 \times 10^{21}\ \text{cm}^{-3}\ (b/\text{eV})^{3/2},$$

where $\vartheta = T/b$. Then the dimensionless near-surface electron density is given by the formulas

$$n_{e0} = C(b)\vartheta^{-3/2}\exp(-1/\vartheta),$$

$$C(b) = 2(m_e/2\pi\hbar^2)^{3/2}(8\pi e^2)^3/b^{3/2}$$

$$= 2.9 \times 10^5\ (\text{eV}/b)^{3/2}.$$

The relationship $n_{e0} = E_0^2$ yields the boundary field strength $E_0 = n_{e0}^{1/2}$. Substituting this value into the above formulas, we readily obtain the surface charge density and express all other characteristics, including $\varphi(x)$, $E(x)$, and $n_e(x)$, as functions of the coordinate x.

Two charged planes. Integrating equation $-d\varphi/dx = [\exp(\varphi/2) - k^2]^{1/2}$, where $k \equiv (1 - E_1^2)^{1/2}$, we obtain

$$\varphi(x) = \ln(E^2 + k^2),$$

$$E(x) = k\tan[(a_0 - x)k/2],$$

$$n_e(x) = (E^2 + k^2).$$

The field strength turns zero at a point with the coordinate $a_0 = (2/k)\arctan(E_0/k)$. The quantity k should be selected such that the values of E_0 and a_0 would correspond to the preset charge density on the plane and to the halfspacing between planes (see below). The electron density does not turn zero within the region under consideration ($0 \le x \le a_0$). In the case of $k = 1$, the solution corresponds to a large charge density on the wall ($E_0 \gg 1$), whereby both potential and the field strength acquire zero values nearly at the same point with $a_0 = \pi$ (see [4, 5]).

In the case of two planes, relationships between the surface field strength E_0 and the thermionic characteristics differ from those obtained above for a single charged plane. Using the formula $n_{e0} = E_0^2 + k^2$ and substituting $k = (n_{e0} - E_0^2)^{1/2}$ into the expression for a_0, we obtain

$$\alpha = (1 - \varepsilon^2)^{-1/2}\arctan[\varepsilon/(1 - \varepsilon^2)^{1/2}],$$

$$\alpha = a_0 n_{e0}^{1/2}/2, \quad \varepsilon = E_0/n_{e0}^{1/2}.$$

These expressions defined E_0 as a function inverse to the relationship $\alpha(\varepsilon)$ presented in Fig. 1.

For a large spacing between plane ($\alpha \gg 1$), whereby $\varepsilon(\alpha) \longrightarrow 1$, the boundary field strength is described by

the same expression as that obtained for a single charged plane: $E_0 = n_{e0}^{1/2}$. At a small distance between planes, that is, for $\alpha \ll 1$ and $\varepsilon(\alpha) \longrightarrow 0$, the boundary field strength (and the charge density on the wall) tends to zero ($E_0 \longrightarrow 0$ for $a_0 \longrightarrow 0$), which appears as if electrons were "squeezed out" on the walls.

The boundary value $a_0 = a_{bd}$, separating the two domains featuring different behavior of E_0 as function of a_0, equals the effective width of a near-wall electron layer created by a single pane: $a_{bd} = 2/E_0 = 2n_{e0}^{-1/2}$.

Uncompensated charge. For the electron distribution near a charged plane with uncompensated charge, a solution to the Poisson–Boltzmann equation yields the following formulas:

$$E(x) = \kappa\frac{e^{x\kappa}(E_0+\kappa)+(E_0-\kappa)}{e^{x\kappa}(E_0+\kappa)-(E_0-\kappa)},$$

$$n_e = \frac{4e^{\kappa x}(E_0^2-\kappa^2)\kappa^2}{(e^{\kappa x}(E_0+\kappa)-(E_0-\kappa))^2}, \quad \varphi(x) = \ln(n_e/\kappa^2),$$

$$a_1 = \kappa\ln\left(\frac{E_0+\kappa}{E_0-\kappa}\right), \quad E_0 = \sqrt{n_{e0}+\kappa^2}.$$

Here, the quantity $\kappa = E(\infty)$ corresponds to the uncompensated charge density on the plane, which has to be determined from additional considerations. Generally speaking, the presence of uncompensated charge implies that the system is rather nonequilibrium: only the electron layer near the plane occurs in thermodynamic equilibrium. Another part of electrons, corresponding to the uncompensated charge, is thermodynamically nonequilibrium. There is a deviation from the ionization equilibrium.

Surface charge of a dust particle. Let us evaluate the characteristic parameters of a thermoemissive plasma for the CrO_2 dust based on the experimental data reported in [2, 3]. The average size and the number density of particles are about $r_0 \approx 0.4$ μm and $N_p \sim 5 \times 10^7$ cm^{-3}, respectively. The average particle charge varies within $Z_p \approx 500$–1000, as determined from the plasma quasineutrality relationship using the values of electron density N_e measured by probing methods. At a temperature of $T = 1700$ K, the system featured some order in the arrangement of dust particles.

For the above parameters, the boundary value of the dimensionless field strength and the ratio of the particle radius to the characteristic width of the electron layer are given by the formulas

$$E_0 \approx (1/2)(Z_p/4\pi r_0^2)(8\pi e^2/T) \approx 7.6\text{–}15;$$

$$(r_0/E_0)(T/8\pi e^2) \approx 0.2\text{–}0.1,$$

which show that we may use the planar model.

Proceeding from the equilibrium conditions considered above, we obtain the following expressions for the charge on the particle surface and a width (dimensional) of the electron layer:

$$Z_p = 2n_{e0}^{1/2}(8\pi e^2/T)^{-2}(4\pi r_0^2),$$

$$a_{bd} = (2/n_{e0}^{1/2})(8\pi e^2/T).$$

Note that the values reported for the electron work function of CrO_2 are somewhat different: $b_1 = 2.75$ eV [1] and $b_2 = 2.1$ eV [2]. Although the latter value seems to be a more adequate characteristic of this material, below we present the results calculated for both values of the electron work function. At $T = 1700$ K, we obtain $Z_p(b_1) \approx 13$, $Z_p(b_2) \approx 115$, and $a_{bd}(b_1) \approx 7r_0$, $a_{bd}(b_2) \approx 0.7r_0$. It should be noted that these Z_p values are markedly lower compared to the experimental data (see above) obtained at the same temperature.

Analysis of the plots of Z_p and a_{bd} versus temperature (Fig. 2) shows that, under thermodynamic equilibrium conditions, the particle charge $Z_p \approx 500$ is attained only for $T = 2000$ K, where the characteristic width is $a_{bd}(b_2) \approx 0.17r_0$. The distance between particles is sufficiently large ($N_p^{-1/3} \approx 70r_0$), which allows the effect of electron "squeezing" mentioned above to be ignored.

The temperature ($T = 2000$ K) at which the surface charge in thermodynamic equilibrium corresponds to that really existing on the plane is markedly higher compared to the experimental value ($T = 1700$ K), which can be explained by the uncertainty of the electron work function determined for the "corrugated" surface of small dust particles. In order to provide for the agreement with the experiment, we should take $b = 1.7$ eV (Fig. 2). In addition, the surface area of a "corrugated" particle can markedly exceed the value $4\pi r_0^2$.

However, there is probably another important circumstance. Indeed, if the values measured in [2, 3] are reliable, we have to suggest that the system features deviation from thermodynamic equilibrium. This implies that a nonequilibrium charge is formed on a particle, which accounts for the nonequilibrium electron density.

Determination of the uncompensated particle charge from balance equations. The uncompensated charge of a dust particle was calculated [4, 7] based on the balance of thermoelectron emission and triple recombination processes. For $b = 2.75$ eV, this approach yields $Z_p \approx 230$ at $T = 1700$ K. Putting the other experimental value $b = 2.1$ eV into the final formulas [4, 7], we obtain $Z_p \approx 410$, while the above estimate $b = 1.7$ eV leads to $Z_p \approx 520$.

Nefedov *et al.* [3] evaluated the charge of a dust particle by equating the emitted (j^-) and absorbed (j^+) elec-

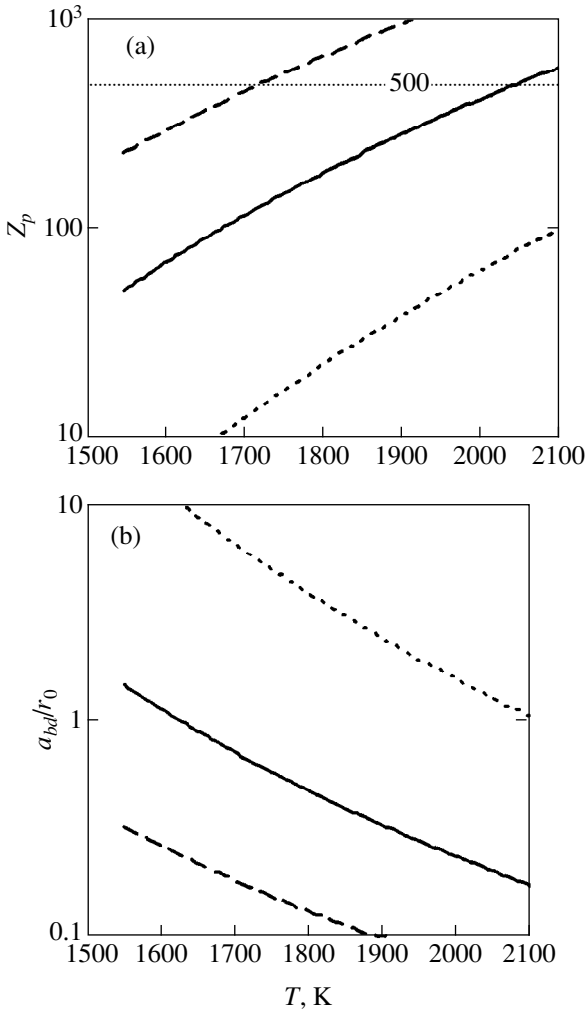

Fig. 2. The plots of (a) particle charge and (b) the ratio of electron layer width to particle radius versus temperature for various values of the electron work function b = 2.1 eV (solid line); 2.75 eV (dotted line); 1.7 eV (dashed line).

tron fluxes, assuming these to obey a relationship for the thermodynamic equilibrium:

$$j^-/j^+ = 1 = (N(T)/N_{e1})\exp(-b/T)\exp(-Z_p e^2/r_0 T),$$

where $N_{e1} = 7 \times 10^{10}$ cm^{-3} is the experimental value of the free electron number density (assumed to occur at the zero potential) and $N(T)$ is the electron density on the wall determined as described above. These relationships yield

$$Z_p = (r_0 T/e^2)[\ln(N(T)/N_e) - b/T].$$

On substituting the values from [3] (T = 1700 K, N_{e1} = 7×10^{10} cm^{-3}, b = 2.1 eV, $r_0 \approx 0.4$ μm), we obtained from this formula Z_p = 324. This estimate markedly differs from the value Z_p = 520 obtained in [3] using the same formulas and parameters. Putting in the last expression $N_e = Z_p N_p$ and numerically solving the resulting equation, we obtain Z_p = 377.

There is an important circumstance that must born in mind in considering the particle charge estimate obtained in [3]. Under thermodynamic equilibrium conditions, the potential on the particle surface cannot be taken equal to that on the surface of an isolated charged sphere (as was done in [3] to derive the above expressions). Indeed, we cannot ignore the fact that a large surface charge in thermodynamic equilibrium must be surrounded by a high-density layer of electrons. As seen from the above considerations, the charged electron layer significantly affects a potential difference between the charged surface and the points of zero potential. In estimating the uncompensated charge, we cannot use a relationship between the j^- and j^+ fluxes corresponding to thermodynamic equilibrium. The charge recombination kinetics must be considered within the framework of a certain model (as it was done in [4, 7]).

Conclusion. Thus, we suggest that the electron shells under the experimental conditions studied in [2, 3] occur in a nonequilibrium state. This conclusion is confirmed by the following facts. It was demonstrated [8] that the electron shells of dust particles in thermodynamic equilibrium may only attract under the action of polarization forces. This attraction is not changed by repulsion at small distances between particles. The thermoelectron plasma of attracting particles can only exist for a short time. In order to provide for the repulsion at small distances, the electron shells must be nonequilibrium. The reasons for which the thermoelectron plasma formed under the experimental conditions [2, 3] is nonequilibrium are still unclear.

REFERENCES

1. V. E. Fortov and I. T. Yakubov, *Nonideal Plasma* (Énergoatomizdat, Moscow, 1994).
2. V. E. Fortov, A. P. Nefedov, K. F. Petrov, *et al.*, Zh. Éksp. Teor. Fiz. **111**, 467 (1997) [JETP **84**, 256 (1997)].
3. A. P. Nefedov, O. F. Petrov, Ya. K. Khodataev, and S. A. Khrapak, Zh. Éksp. Teor. Fiz. **115**, 837 (1999) [JETP **88**, 460 (1999)].
4. A. N. Tkachev and S. I. Yakovlenko, *Electron Shells of Charged Microparticles: A Preprint of the Institute of General Physics, Russian Academy of Sciences*, No. 8 (1997).
5. A. N. Tkachev and S. I. Yakovlenko, Zh. Tekh. Fiz. **79**, 53 (1999) [Tech. Phys. **44**, 48 (1999)].
6. E. G. Gibson, Phys. Rev. **9**, 2389 (1966).
7. A. N. Tkachev and S. I. Yakovlenko, Pis'ma Zh. Tekh. Fiz. **25**, 25 (1999) [Tech. Phys. Lett. **25**, 10 (1999)].
8. S. I. Yakovlenko, Pis'ma Zh. Tekh. Fiz. **25**, 83 (1999) [Tech. Phys. Lett. **25**, 670 (1999)].

Translated by P. Pozdeev

Technical Physics Letters, Vol. 26, No. 4, 2000, pp. 341–344. Translated from Pis'ma v Zhurnal Tekhnicheskoĭ Fiziki, Vol. 26, No. 8, 2000, pp. 56–64.

Sound Excitation by the Laser-induced Breakdown in a Liquid with Microinhomogeneities

M. L. Lyamshev

Research Center of Wave Phenomena, Institute of General Physics, Russian Academy of Sciences, Moscow, 117942 Russia

Received December 7, 1999

Abstract—The excitation of sound in a heterogeneous liquid by the breakdown induced by a laser pulse is studied theoretically. The heterogeneity stems from the presence of microparticles with various sizes. The microparticles form clusters representing multifractals. The size distribution of the microparticles is described by a power function, reflecting the scale invariance of fractals. Dependence of the acoustic signal amplitude on the fractal dimension of clusters, the probability density function of the microparticle size distribution, and the laser pulse energy is discussed. *© 2000 MAIK "Nauka/Interperiodica".*

Laser-induced breakdown is essentially a threshold phenomenon. The breakdown intensity threshold is determined by small-scale heterogeneity inherent in real liquids, including those occurring in nature. The heterogeneity usually stems from the presence of microparticles with various sizes; for example, the size may range from 10^{-2} to 100 μm. Absorbed by a microparticle, laser radiation heats it to a temperature sufficient for the primary ionization and the formation of dense plasma. The plasma absorbs the radiation efficiently. The concomitant heating leads to the creation of a plasma cavity, which expands to generate a shock wave in the liquid. After the laser pulse has ceased and energy is no longer supplied to plasma, the cavity gives rise to a bubble performing several pulsations. If the concentration of microparticles is large (as in a contaminated or naturally occurring liquid), the number of cavities (bubbles) increases with the radiation intensity so that a cloud of shining bubbles appears [1].

The first acoustic sign of the laser-induced breakdown is the appearance of a random-amplitude component of the optoacoustic signal. This implies that both the physical pattern outlined above and the probabilistic nature of the processes must be taken into account. As for the latter, there are at least three factors of importance: (1) the possibility that microparticles may form clusters or aggregates called multifractals; (2) the random distribution of the size of microparticles (cavities); and (3) the thermal properties of microparticles, including dependence of the threshold laser intensity on the microparticle size. Consideration (1) is suggested by observations: the cloud of bubbles formed upon the breakdown has an irregular shape, which is now called a fractal. Fractal clusters are known to arise during the electric breakdown in dielectrics [2]. Lightning discharge in the atmosphere is a vivid manifestation of the phenomenon.

Let a liquid with microparticles be exposed to a focused laser pulse. The heating of the microparticles results in the formation of plasma cavities and then bubbles. The expansion and collapse of the bubbles generate an acoustic signal. The signal amplitude can be estimated on the basis of the theory of underwater explosions and pulsed electric discharges in water [1, 3, 4].

Denoting the pressure in a cavity by p_1, we may express this quantity as

$$p_1 \approx \rho u^2 = \rho \frac{R_0^2}{\tau^2}, \qquad (1)$$

where ρ is the density of the liquid, R_0 is the characteristic radius of the cavity at the end of the laser energy release, τ is the duration of the laser pulse, and $u = R_0/\tau$ is the characteristic expansion speed of the cavity. The total energy of the laser pulse will be denoted by E, and its portion released in the cavity, by E'.

The energy balance equation for the cavity yields

$$R_0 \approx \left[\frac{3(\gamma - 1)}{4\pi\rho}\tau^2 E'\right]^{1/5}. \qquad (2)$$

For the laser-induced breakdown of water vapor, one should insert $\gamma = 1.26$.

If the breakdown threshold is exceeded to a modest extent, so that only isolated plasma cavities are created in the liquid, we can assume that E' is proportional to the cross-section area of a heated microparticle, namely, to πx^2:

$$E' = E\frac{x^2}{a^2}, \qquad (3)$$

where x is the radius of the microparticle, or, more precisely, the radius of the microparticle absorption cross section, and a is the radius of the region where the

1063-7850/00/2604-0341$20.00

formed laser radiation intensity is equal to or above the threshold.

The amplitude of the peak pressure in the shock wave can be evaluated in terms of the Kirkwood–Bethe approximation. Let r denote the distance from the cavity. At a sufficiently large distance ($r \gg R_0$), we have an acoustic wave with

$$p = \frac{p_1 R_0}{2r} g \exp\left(-\frac{t}{\theta}\right), \tag{4}$$

where $\theta = 1 + (2/g)$, $g = M^{3/2}\{[2\ln(r/R_0)]^{1/2}\}^{-1}$, and $M = u/c = R_0/c\tau$, with c being the speed of sound in the liquid. The factor g allows for the nonlinear attenuation of the shock wave, and M is the Mach number which characterizes the expansion speed of the cavity.

Assume that microparticles are equal in size and thermal properties and that they are distributed uniformly (over the exposed region in which the laser radiation is focused). Also suppose that the signals separately generated by each of the cavities are added in phase. Then the total pressure amplitude is

$$p(r) = \frac{\rho^{2/5}}{2r}\left(\frac{3(\gamma-1)}{4\pi}\right)^{3/5}\tau^{-8/5}\left(\frac{x}{a}\right)^{6/5} E^{3/5} g n a^3 \exp\left(-\frac{t}{\theta}\right), \tag{5}$$

or, in short,

$$p(r) \sim E^{3/5}. \tag{6}$$

Contrary to the assumptions used to derive equations (5) and (6), the microparticles in a real liquid may be distributed randomly, forming clusters or multifractals.

Let us estimate the effect of a fractal distribution of the microparticles (cavities) in the breakdown region on the amplitude of the optoacoustic signal.

Fractals are usually characterized in terms of the correlation functions and their frequency dependences (spectra). The functions and the spectra obey the power law, owing to the scale invariance of fractals. According to [5], a typical correlation function of a multifractal is

$$f(\mathbf{R}) \sim \langle \rho(0)\rho(\mathbf{R})\rangle \sim R^{D-d}. \tag{7}$$

Here, D is the fractal dimension of the cluster and d is the dimension of the embedding space (in our case, $d = 3$).

The mean-square optoacoustic signal fluctuation is

$$\langle |p(r)|^2\rangle = \frac{R_0^2}{4r^2} g^2 \exp\left(-\frac{2t}{\theta}\right)\iint_{VV}\langle p_1(\bar{r}')p_1^*(\bar{r}'')\rangle dV(\bar{r}')dV(\bar{r}'') = p_1^2\frac{4\pi^2}{3r^2} n^2 a^3 R_0^2 g^2 \exp\left(-\frac{2t}{\theta}\right)\int_0^a f(R)R^2 dR, \tag{8}$$

where $\langle p(\bar{r}')p^*(\bar{r}'')\rangle = n^2 f(R)$ and $R = |\bar{r}' - \bar{r}''|$. Formula (8) was derived under assumptions that the averaging is performed over the statistical ensemble of acoustic signals (pulses) and that the processes are statistically homogeneous.

Consider the normalized correlation function

$$f(R) = \left(\frac{R}{l}\right)^{D-3}\exp\left(-\frac{R}{l}\right). \tag{9}$$

The integration gives

$$\langle p^2(r)\rangle = p_1^2\frac{4}{3r^2}\pi^2 a^3 l^3 R_0^2 g^2 n^2 \exp\left(-\frac{2t}{\theta}\right)\Gamma(D) \sim nR^6\Gamma(D), \tag{10}$$

where $\Gamma(D)$ is the gamma function.

Note that the mean-square fluctuation of the optoacoustic signal is independent of the laser pulse energy if $n = \text{const}$ and $\Gamma(D) = \text{const}$. This fact is hardly surprising, because the microparticles have the same radius, the characteristic radii and expansion speeds of the cavities rise with laser pulse energy in the same manner, and the fractal dimension D is determined solely by spatial distribution of the cavities.

Now, let us assess the effect of the microparticle size distribution. Recall that the particle sizes in a real liquid may differ by three to four orders of magnitude. Let us replace R_0 in (10) by the mean value $\langle R_0\rangle$ evaluated from a probability density function (pdf) for the size distribution of the microparticles (cavities). We consider a pdf of the type

$$w(x) = x^{-D_1}, \tag{11}$$

where D_1 is the fractal dimension [6].

A power function in equation (11) reflects the scale invariance of the size distribution of microparticles (cavities). A random process with pdf (11) is known as the Levy flight.[1]

Expression (11) is supported by numerous experiments. For example, this function describes the size distribution of pores in porous materials, with D_1

[1] A different pdf for the cavity size distribution was used in [7]. Borrowed from geophysics, that pdf was a power function called the Mengor sponge. Our present choice is based on experimental results (see below).

($D_1 > 1$) depending on the processing technology [8]. Evidence for the applicability of pdf (11) to plasma cavities in a liquid under laser-induced breakdown was reported in [9].

If $D_1 > 1$, then a mean $\langle x \rangle$ exists that is given by the formula

$$\langle x_{x_0} \rangle = \frac{x_0 D_1}{D_1 - 1}, \quad (12)$$

where x_0 is the radius of the smallest microparticle [6, p. 157].

Formulas (12), (2), and (3) yield a mean characteristic radius of the plasma cavity:

$$\langle R_0 \rangle = \left[\frac{3(\gamma - 1)}{4\pi\rho} \tau^2 \frac{x_0^2}{a^2} \frac{D_1^2}{(D_1 - 1)^2} E \right]^{1/5}. \quad (13)$$

Inserting (1) and (13) into (10) gives an expression for the rms pressure fluctuations in the acoustic field generated in the liquid:

$$[\langle |p(r)|^2 \rangle]^{1/2} \sim n \left(\frac{D_1}{D_1 - 1} \right)^{6/5} \Gamma(D)^{1/2} E^{3/5}. \quad (14)$$

Thus, the rms acoustic signal fluctuation retains the form of equation (6), being proportional to $E^{3/5}$, if n = const, D = const, and D_1 = const.

The above results basically follow from the assumptions that all microparticles have the same thermal properties and that the cluster fractal dimension and the particle size pdf are independent of the laser pulse energy.

In real liquids, microparticles may differ in thermal properties as well as in size. Hence the discrepancy between the rms pressure fluctuation–laser pulse energy dependences reported by various researchers dealing with the sound excitation in liquids under the laser induced breakdown conditions [9]. There is certain analogy with the laser-induced breakdown of gases contaminated with microparticles [10]. The point is that the threshold intensity may be a function of the microparticle size, the form of this function depending on the microparticle thermal properties, laser pulse duration, and radiation wavelength. In particular, the threshold intensity may be inversely proportional to the microparticle radius or its square, or may be independent of the radius. In the above paragraphs, we concentrated on the latter case so as to get a clear picture of how the fractal properties of contaminating microparticles influence the rms optoacoustic signal fluctuations in a real liquid during the laser-induced breakdown.

We have assumed that, in the breakdown region, the concentrations of microparticles and plasma cavities are the same and are independent of the laser pulse energy (n = const). If there are microparticles for which the threshold intensity is size-dependent, then the cavity concentration n is variable. The concentration will increase with the laser pulse energy until it becomes equal to the concentration of microparticles. In the general case,

$$[\langle |p(r)|^2 \rangle]^{1/2} \sim n(E) \left(\frac{D_1(E)}{D_1(E) - 1} \right)^{6/5} \Gamma[D(E)] E^{3/5}. \quad (15)$$

It can easily be shown that $n \sim E$ or $n \sim E^2$ if the exposed region contains microparticles for which the threshold intensity is inversely proportional to the particle radius or its square, respectively.

Typically, the fractal cluster dimension falls within $1 < D < 3$. The fractal dimension D_1, or the exponent of the plasma cavity (pore) size distribution function, is always greater than unity ($D_1 > 1$). Experiment and theory suggest that both D and D_1 may depend on the laser-pulse energy (see, e.g., [9, 11]). As a generalization of the above, we may write

$$[\langle |p(r)|^2 \rangle]^{1/2} \sim E^{\eta}, \quad (16)$$

where η acquires the values greater than unity.

The conclusions drawn from this study are as follows. The acoustic signal amplitude may vary rather slowly with the laser pulse energy in the initial and final stages, where the rise in the energy causes no increase in the number of cavities. In the initial stage, the function is determined by the expansion law of an isolated cavity. The same picture can be seen in the final stage, where the number of cavities is large but virtually constant. The cavities form a fractal cluster; the size distribution of the cavities has a fractal shape as well. The mean cavity radius increases with the laser pulse energy according to the law for an isolated cavity.

Experiments indicate that there may be an intermediate region where the acoustic signal amplitude increases in an essentially nonlinear manner with the laser energy (see, e.g., [9]). From the above reasoning it is clear that this process should be described in terms of a particular statistical model of development of the fractal cavity structure in the breakdown region, taking into account the energy dependences of the number of cavities (bubbles) and the fractal dimensions of the cluster and the cavities during their formation.

This study was supported by the Russian Foundation for Basic Research, project no. 99-02-16334.

REFERENCES

1. L. M. Lyamshev, Usp. Fiz. Nauk **135**, 637 (1981) [Sov. Phys. Usp. **24**, 977 (1981)].
2. S. Satiati, in *Fractals in Physics*, Ed. by L. Peietronero and E. Tosatti (North-Holland, Amsterdam, 1986; Mir, Moscow, 1988), pp. 239–243.
3. R. H. Cole, *Underwater Explosions* (Princeton University Press, Princeton, 1948; Inostrannaya Literatura, Moscow, 1955).
4. K. A. Naugol'nykh and N. A. Roĭ, *Electric Discharges in Water* (Nauka, Moscow, 1971).

5. E. Feder, *Fractals* (Plenum Press, New York, 1988; Mir, Moscow, 1991).
6. M. Schroeder, *Fractals, Chaos, Power Laws: Minutes from an Infinite Paradise* (Freeman, New York, 1991).
7. M. L. Lyamshev, Akust. Zh. **44**, 851 (1998) [Acoust. Phys. **44**, 743 (1998)].
8. D. Shefer and K. Kefer, in *Fractals in Physics*, Ed. by L. Peietronero and E. Tosatti (North-Holland, Amsterdam, 1986; Mir, Moscow, 1988), p. 62.
9. S. Egerev, L. M. Lyamshev, and Ya. Simanovskii, *Laser Ultrasound Source for NDE Applications: Calibration in a Liquid. Nondestructive Characterization of Materials VIII*, Ed. by R. Green (Plenum Press, New York, 1998), pp. 47–52.
10. F. V. Bunkin and V. V. Savranskiĭ, Zh. Éksp. Teor. Fiz. **65**, 2185 (1973) [Sov. Phys. JETP **38**, 1091 (1973)].
11. G. Wisman and L. Peietronero, in *Fractals in Physics*, Ed. by L. Peietronero and E. Tosatti (North-Holland, Amsterdam, 1986; Mir, Moscow, 1988), pp. 21–220.

Translated by A. A. Sharshakov

Technical Physics Letters, Vol. 26, No. 4, 2000, pp. 345–347. Translated from Pis'ma v Zhurnal Tekhnicheskoĭ Fiziki, Vol. 26, No. 8, 2000, pp. 65–71.

The Mechanism of Sliding Friction Wear in Polycrystalline Solids

B. M. Ginzburg

Institute of Machine Science, Russian Academy of Sciences, St. Petersburg, Russia

Received November 24, 1999

Abstract—A new micromechanical model describing the sliding friction wear of polycrystalline solids is proposed. The model is consistent with a hypothesis suggested previously, according to which the transition from intensive to moderate wear (for the nonconforming bodies in sliding friction contact) is related to attaining a definite, sufficiently small shear strain rate at the friction surface, depending on the absolute value of the normal force applied to the friction contact. In addition, the model explains some well-known empirical relationships between the wear intensity and friction coefficient for steel on steel in a wide range of loads and pressures in the friction contact. *© 2000 MAIK "Nauka/Interperiodica".*

As demonstrated in the previous work [1], tribological methods can be employed as a means of detecting changes in the mechanisms of surface fracture in solids during friction. This possibility is offered, in particular, by the method of rapid evaluation of the intensity of wear in a wide range of contact pressures (from a few to hundreds MPa) and loads [1, 2] based on the friction of nonconforming cylindrical counterbodies with initial line contact.

According to this technique, a sample (representing an immobile cylinder made of a comparatively soft steel) exhibits wear and the line of contact between the sample and a counterbody transforms into a groove with a finite width a. As a result, the contact (groove) surface gradually increases and the contact pressure P accordingly decreases. On reaching a certain, sufficiently small, critical contact pressure P_c, the character of the volume wear kinetics of the sample changes, which is indicative of a certain modification of the wear mechanism, resulting in the transition from intensive to moderate wear.

However, it was established that the P_c value depends on the normal force F_n applied to the friction joint via the immobile sample, which is maintained constant during the whole tribological experiment. Then it was suggested that the change in the mechanism of wear takes place at a certain rate of the surface deformation (shear straining), which is proportional to the rate of variation of the groove width da/dt. This assumption led to the following relationship between two arbitrary P_c values and the corresponding normal forces F_n:

$$f_1 P_{c1}^2/F_{n1} = f_2 P_{c2}^2/F_{n2}, \quad (1)$$

where f_1 and f_2 are the friction coefficients. If the f_1 and f_2 values very but slightly with the load, the above relationship simplifies to

$$P_{c1}/P_{c2} = (F_{n1}/F_{n2})^{1/2}. \quad (2)$$

Relationship (2) was confirmed in experiment [1], thus validating selection of the quantity da/dt as a measure of the surface strain rate and showing evidence for the above hypothesis that a phenomenological difference in the critical pressures P_c corresponding to various normal loads F_n reflects a difference in the rates of surface shear straining.

In development of the above hypothesis, this paper suggests a model explaining a change in the mechanism of wear on a microscopic level depending on the absolute value of the normal force applied to the friction joint. This model explains the known empirical relationships between wear intensity and friction coefficients of steel in a wide range of normal loads applied to the friction surface.

As is known, an increase in the normal load results in that the counterbodies exhibit a mutual approach at the expense of increasing normal deformation within the contact spot [3]. Since the counterbodies in friction contact are not ideally smooth and exhibit certain surface roughness, each microscopic asperity on the sample surface (Fig. 1A) colliding with the oncoming surface features of the (more hard) counterbody is subject to shear deformation. The smaller the spacing between counterbodies in the contact, the greater the resulting shear strain. Since the straining takes pace within the same time interval, the shear strain rate also increases with decreasing spacing and increasing normal load.

A similar situation takes place for a microscopic asperity that was compressed upon the initial loading of counterbodies (Fig. 1B). The greater the extent of compression, the higher the shear strain rate.

1063-7850/00/2604-0345$20.00 © 2000 MAIK "Nauka/Interperiodica"

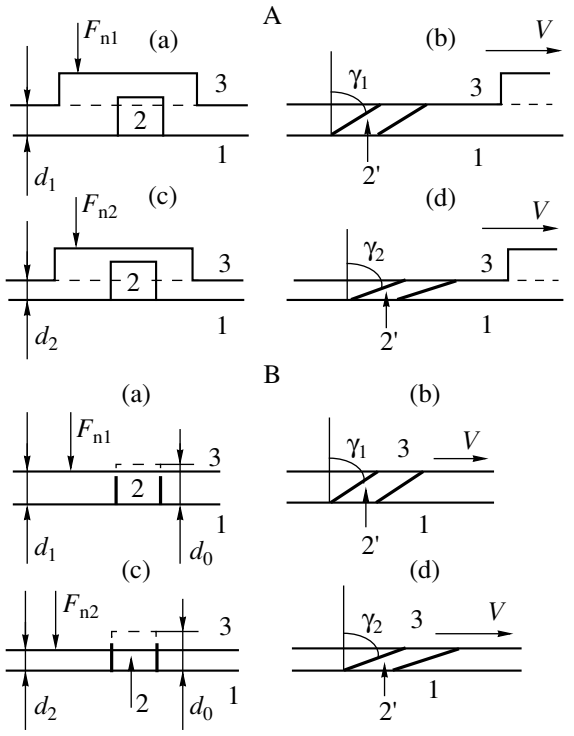

Fig. 1. Schematic diagrams illustrating the shear straining of microscopic asperities (representing square parallelepipeds) on a sample surface site (A) not in close contact with the counterbody and (B) pressed against the counterbody: (1) immobile sample; (2) asperity; (3) mobile counterbody; (a, c) initial state; (b, d) shear-strained state; (a, b) lower normal load F_{n1} leading to greater distance d_1 and lower shear strain γ_1; (c, d) greater normal load F_{n2} leading to smaller distance d_2 and higher shear strain γ_2.

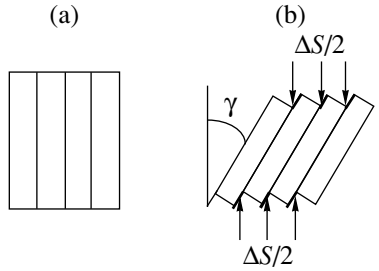

Fig. 2. Schematic diagrams illustrating the shear straining of crystallites: (a) nondeformed state; (b) deformed state characterized by additional free surface ΔS appearing upon deformation.

Note that the shear straining of each individual crystallite or crystal grain increases the surface area and, hence, the free surface energy (Fig. 2). This increase in the free surface energy may become sufficiently large to be comparable with the free surface energy of a crystallization nucleus at a temperature developed on the friction surface. This would result in local melting (fusion) of the crystallites followed by the local crystallization of a nondeformed material within the same microscopic volumes. The phenomenon of local melting and recrystallization at room temperature (typical experimental temperature) was observed in oriented polyethylene (melting at 100–115°C under normal conditions) where the shear straining of crystallites took place in the course of reorientation [4].

The hypothesis of local fusion was repeatedly formulated for the behavior of microscopic asperities in metals during friction [3, pp. 15–22]. Direct IR pyrometric measurements performed at high sliding velocities in the contact sites of airplane brake shoes indicated that the local temperature reached the melting point of one of the counterbodies [3, pp. 153–159], while being several hundred degrees lower in the sites where no direct friction contact took place.

However, the key point in our hypothesis is that the fusion of microscopic asperities may be caused both by a local increase in the temperature due to dissipation of the energy of the friction surface deformation and by a decrease in the local melting point of crystallites forming the surface asperities. The degree of this decrease may depend on the level of shear strain and on the size of initial crystal grains: the greater the grain size, the higher the shear strain necessary to induce the local fusion [4]. In the limiting case, a sufficiently large shear straining may render the grain two-dimensional. Thus, the ultimately low melting temperature of the microscopic surface asperities corresponds to the melting point of a two-dimensional ordered monolayer with a given lattice structure. According to rough estimates [5], this temperature amounts to two-thirds of that for the bulk crystal; for example, the melting temperature in steel junctions may decrease to 1100–1200 K.

The above estimate agrees with the results of the electron diffraction measurements on lead and tin islands obtained by deposition onto a carbon substrate [6]: it was established that reduction in the particle size to ~3 nm was accompanied by a decrease in the melting temperature to ~2/3 of the equilibrium value for a given metal.

The melting temperature of a spherical crystal can be also evaluated using the Thomson formula [6, 7]:

$$T_R = T_0(1 - 2\sigma v/qR), \tag{3a}$$

where T_R is the melting temperature of the crystal with the radius R, T_0 is the equilibrium melting temperature, σ is the surface energy at the phase boundary (interfacial energy), v is the volume per atom in the crystal lattice, and q is the latent heat of crystallization per atom. Upon substituting the corresponding values ($v = 10^{-29}$ m^3; $q \approx 10^{-19}$ J), we obtain

$$T_R = T_0(1 - 2\sigma \times 10^{-10}/R). \tag{3b}$$

A specific free surface energy of iron exposed to a gas phase is typically about $\sigma \approx 2$ J/m^2 [8], while the value

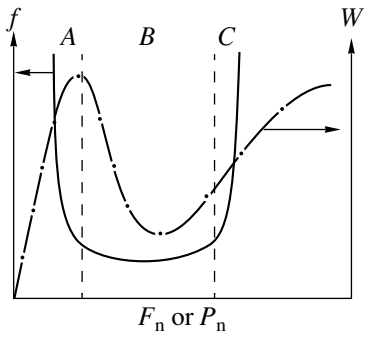

Fig. 3. Schematic diagrams illustrating the most general relationship between the sliding friction coefficient f and normal load F_n or contact pressure P_n and an empirical curve of the wear intensity W (weight loss per unit contact area and unit friction path length) for a soft steel in dry friction joint with a hard steel [9]. Region A corresponds to small loads leading to brittle fracture caused by fatigue processes; region B represents the case of moderate loads and small friction coefficients featuring local fusion of microscopic asperities; region C refers to high loads corresponding to the brittle fracture due to high rate of shear straining of the microscopic surface asperities.

for an iron surface in contact with the melt is much lower. Since no direct experimental data for iron are available, we will adopt (by analogy with other substances) that the latter σ value is about one-tenth of the former. Then

$$T_R = T_0(1 - 0.4 \times 10^{-10}/R), \qquad (3c)$$

where R is the crystal radius expressed in meters. In particular, for $R \approx 10^{-10}$ m (i.e., of the order of a monolayer thickness), we obtain approximately the same estimate as above: $T_R \approx 0.6T_0$.

It should be emphasized that the friction process features a competition between effects due to the absolute value of the shear strain and that due to the rate of shear straining. The fusion of some microscopic asperities may account for the favorable friction conditions in the range of moderate normal loads and pressures, thus leading to lower wear. Higher loads may lead to an increase in the deformation rate by the mechanism considered above, which would result in brittle fracture. At small loads, the absolute value of the shear strain is insufficient to provide for the melting of a large part of the microscopic asperities and the fracture exhibits a brittle character as well.

The proposed model agrees with the most general nonmonotonic empirical relationship between friction coefficient and load [3, p. 141], as well as with an empirical relationship known for the wear intensity of soft steel in a friction joint with hard steel [9] (Fig. 3).

Study of the worn friction surfaces by microscopic and other methods *post factum* not always unambiguously reveals the features characteristic of brittle or plastic fracture. However, in our opinion, this circumstance by no means contradicts to the above hypothesis and is apparently related to the fact that, upon fracture taking place within certain region of a friction contact, both the modified region and the wear product particles are subject to significant changes in the course of continued friction.

The proposed mechanism of sliding friction and wear on a rough surface in the contact of crystalline solids does not imply rejecting the other known mechanisms and may well coexist with them.

The author is grateful to S.A. Kukushkin and A.V. Osipov for fruitful discussions of some aspects of this work.

REFERENCES

1. B. M. Ginzburg *et al.*, Pis'ma Zh. Tekh. Fiz. **21**, 41 (1995) [Tech. Phys. Lett. **21**, 18 (1995)].
2. Yu. P. Kozyrev *et al.*, Wear **171**, 71 (1995).
3. *Contact Interaction of Solids and Calculation of Friction Forces and Wear. A Collection of Papers*, Ed. by A. Yu. Ishlinskiĭ and N. B. Demkin (Nauka, Moscow, 1971).
4. B. M. Ginzburg, N. Sultanov, and D. Rashidov, J. Macromol. Sci., Phys. **9**, 609 (1974).
5. S. L. Palatnik, M. Ya. Fuks, and V. M. Kosevich, *Mechanism of Formation and Substructure of Condensed Films* (Nauka, Moscow, 1972).
6. V. P. Skripov and V. P. Koverda, *Spontaneous Crystallization of Supercooled Liquids* (Nauka, Moscow, 1984).
7. S. A. Kukushkin and A. V. Osipov, Usp. Fiz. Nauk **168**, 1083 (1998) [Phys. Usp. **41**, 983 (1998)].
8. *Physical Values. A Handbook*, Ed. by I. S. Grigor'ev and E. Z. Meĭlikhova (Énergoatomizdat, Moscow, 1991), p. 335.
9. F. P. Bowden and D. Tabor, *The Friction and Lubrication of Solids* (Clarendon Press, Oxford, 1950).

Translated by P. Pozdeev

Technical Physics Letters, Vol. 26, No. 4, 2000, pp. 348–351. Translated from Pis'ma v Zhurnal Tekhnicheskoĭ Fiziki, Vol. 26, No. 8, 2000, pp. 72–82.

Planar Two-Dimensional Bragg Resonators with Corrugated Surfaces: Theory and Experiment

N. Yu. Peskov, N. S. Ginzburg, G. G. Denisov, A. S. Sergeev, A. V. Arzhannikov, P. V. Kalinin, S. L. Sinitskiĭ, and V. D. Stepanov

Institute of Applied Physics, Russian Academy of Sciences, Nizhni Novgorod, 603600 Russia
Institute of Nuclear Physics, Siberian Division, Russian Academy of Sciences, Novosibirsk, Russia

Received December 1, 1999

Abstract—The electrodynamic properties of a planar two-dimensional Bragg resonator with two-dimensional distributed feedback were studied. A high selectivity of the resonator with respect to the longitudinal and the transverse mode indices is demonstrated, the mode spectrum being significantly dependent on the surface relief pattern of the resonator plates. The theoretical results are confirmed by measurements under "cold" conditions.

Planar resonators with two-dimensional distributed feedback (two-dimensional Bragg resonators) were suggested in [1–3]. They were designed to ensure spatial coherence of the radiation from high-power free-electron masers powered by wide ribbon-shaped relativistic electron beams. Performance of the new feedback mechanism in free-electron lasers was demonstrated in experiments jointly conducted by the Institute of Nuclear Physics (INP) and the Institute of Applied Physics [4–6]. The experiments were carried out with the ELMI system (INP), using a high-current ribbon beam of microsecond pulse length. This paper presents a theoretical and experimental investigation into the electromagnetic characteristics of two-dimensional Bragg resonators.

A two-dimensional Bragg resonator can be designed as a pair of metal plates with a double periodic relief pattern whose translation vectors are noncollinear (Fig. 1a). The corrugated pattern produces the mutual coupling and scattering of four partial waves propagating in two orthogonal directions:

$$\mathbf{E} = \mathrm{Re}[(\mathcal{A}_+\mathbf{E}_{a+}\exp(-ih_{a+}z) + \mathcal{A}_-\mathbf{E}_{a-}\exp(ih_{a-}z) + \mathcal{B}_+\mathbf{E}_{b+}\exp(-ih_{b+}x) + \mathcal{B}_-\mathbf{E}_{b-}\exp(ih_{b-}x))e^{i\omega t}], \quad (1)$$

where h_j are the propagation constants and $\mathbf{E}_j$ describe the transverse (along the y-axis) field distribution ($j = a, b$). Generally, the waves may differ in both h_j and $\mathbf{E}_j$. If a synchronous wave $\mathcal{A}_+$ propagates in the direction of translatory electron motion and is amplified by the electron stream, then the transverse waves $\mathcal{B}_\pm$ ensure the synchronization of radiation in different parts of the beam.

Technologically, the simplest relief pattern is an orthogonal grid of rectangular grooves (Fig. 1b). This corrugation is described by a product of two periodic functions

$$a(x, z) = a_1 f(x - z) f(x + z), \quad (2)$$

where

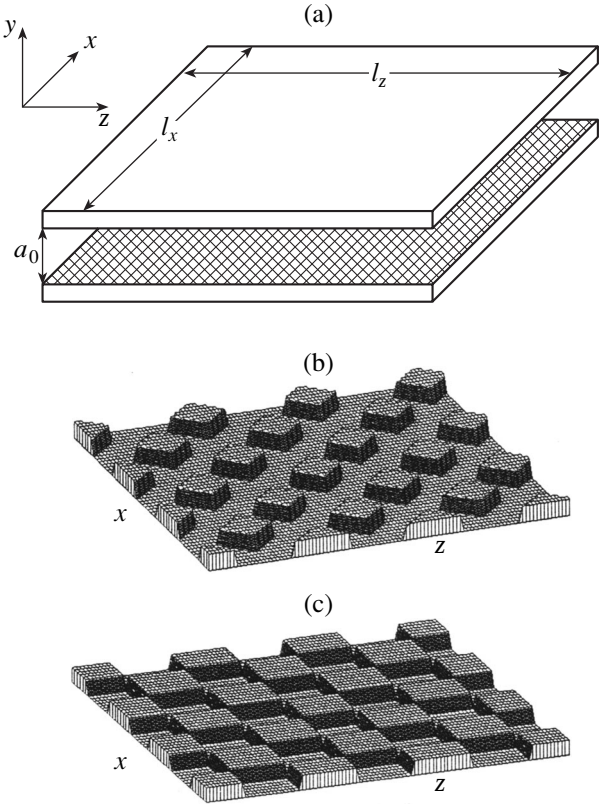

Fig. 1. Schematic diagrams of (a) a planar Bragg resonator, (b) the relief pattern of orthogonal groves under study, and (c) a "chessboard" pattern where resonances are suppressed.

1063-7850/00/2604-0348$20.00

$$f(\xi) = \begin{cases} 0 & 0 < \xi < d/2 \\ 1 & d/2 < \xi < d \end{cases},$$

$f(\xi + d) = f(\xi)$, d is the pitch of the grooves, and a_1 is their depth. Let a_1 be small (low corrugation depth approximation). Expanding (2) into a Fourier series and restricting the expansion to the first-order terms, we obtain

$$a(x, z) = \frac{a_1}{\pi}\Big(\cos(\bar{h}x - \bar{h}z) + \cos(\bar{h}x + \bar{h}z) + \frac{2}{\pi}\cos(2\bar{h}x) + \frac{2}{\pi}\cos(2\bar{h}z)\Big), \quad (3)$$

where $\bar{h} = \sqrt{2}\,\pi/d$. The pattern has two feedback loops. The first two terms in the right-hand part of (3) represent the cross scattering of the four waves ($\mathcal{A}_+ \longleftrightarrow \mathcal{B}_\pm \longleftrightarrow \mathcal{A}_-$). Their longitudinal wavenumbers are the same, $h_{a\pm} = h_{b\pm} = h$, if the pattern parameters (namely, the corrugation period d and the plate spacing a_0) are adjusted so as to satisfy the Bragg resonance condition

$$h \approx \bar{h}. \quad (4)$$

The other two harmonics in equation (3) represent the forward "one-dimensional" scattering of the forward and the backward wave (i.e., $\mathcal{A}_+ \longleftrightarrow \mathcal{A}_-$ and $\mathcal{B}_+ \longleftrightarrow \mathcal{B}_-$, cf. [7–9]), subject to the resonance condition

$$h_{a+} + h_{a-} \approx 2\bar{h}, \quad h_{b+} + h_{b-} \approx 2\bar{h}. \quad (5)$$

Clearly, condition (5) follows from condition (4), but not vice versa.

Another pattern was theoretically studied in [2, 3], where "ideal" two-dimensional Bragg resonators with a sine-shaped corrugation profile

$$a(x, z) = a_1(\cos(\bar{h}x - \bar{h}z) + \cos(\bar{h}x + \bar{h}z)) \quad (6)$$

were considered and their spectrum of modes was found. It was demonstrated that this design offers mode selection in terms of the longitudinal and transverse mode indices and that it ensures single-mode single-frequency operation with a ribbon-shaped electron beam of a sophisticated configuration. At the same time, the experiments reported in [4–6] referred to the two-dimensional Bragg resonators corrugated according to pattern (2). This alternative requires special treatment due to an additional resonance condition (5), which is valid for this system simultaneously with condition (4).

The scattering of waves (1) subject to conditions (4) and (5) is described by the coupled wave equations (cf. [7, 10])

$$\frac{\partial \mathcal{A}_\pm}{\partial z} \mp i\delta\mathcal{A}_\pm \pm i\alpha_1(\mathcal{B}_+ + \mathcal{B}_-) \pm \alpha_2\mathcal{A}_\mp = 0,$$
$$\frac{\partial \mathcal{B}_\pm}{\partial x} \mp i\delta\mathcal{B}_\pm \pm i\alpha_1(\mathcal{A}_+ + \mathcal{A}_-) \pm \alpha_2\mathcal{B}_\mp = 0, \quad (7)$$

where α_1 and α_2 are the wave coupling factors [7] and

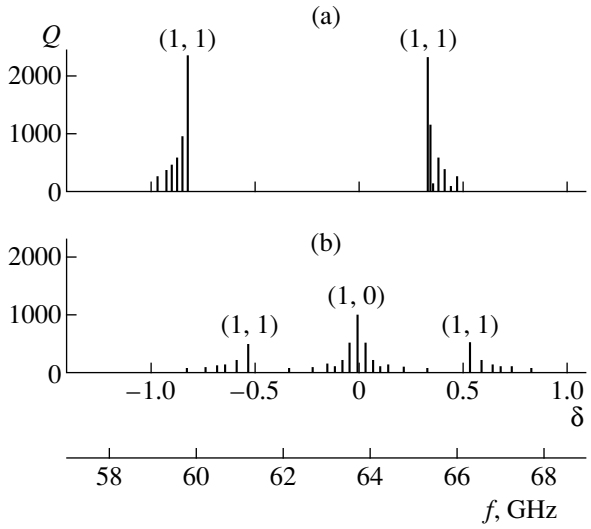

Fig. 2. Computed spectrum of resonator modes for $l_x = l_z = 25$ cm, $d = 0.33$ cm, $\alpha_1 = 0.25$ cm^{-1}, and (a) $\alpha_2 = 0.3$ cm^{-1} or (b) $\alpha_2 = 0$.

$\delta = h - \bar{h}$. The coupling factors refer to the resonance scattering under conditions (4) and (5), respectively. For TEM waves,

$$\alpha_1 = \frac{a_1\bar{h}}{2\pi a_0}, \quad \alpha_2 = \frac{2a_1\bar{h}}{\pi^2 a_0}. \quad (8)$$

The spectrum of resonator modes was found from equations (7) with the boundary conditions dictated by the absence of input power and by the perfect partial wave matching at the resonator boundaries:

$$\mathcal{A}_+(x, 0) = 0, \quad \mathcal{A}_-(x, l_z) = 0,$$
$$\mathcal{B}_+(0, z) = 0, \quad \mathcal{B}_-(l_x, z) = 0. \quad (9)$$

If the wave coupling is strong, so that $\alpha_{1,2}l_{x,z} \gg 1$, then the resonator has several families of high-Q modes (Fig. 2a), with ($Q_{m,n} \approx \bar{h}/2\mathrm{Im}\,\delta_{m,n}$) and frequencies ($\omega_{m,n} \approx c\bar{h} + c\mathrm{Re}\,\delta_{m,n}$) determined by the relationship

$$\delta_{n,n} = \alpha_2 + \frac{\pi^2 n^2}{2l_z^2(\alpha_2 \mp \alpha_1)} + i\frac{\pi^2 n^2}{l_z^3(\alpha_2 \mp \alpha_1)^2}, \quad (10a)$$

$$\delta_{m,n} = -2\alpha_1 - \alpha_2 - \frac{\pi^2}{4(\alpha_1 + \alpha_2)}\left(\frac{n^2}{l_z^2} + \frac{m^2}{l_x^2}\right) + i\frac{\pi^2}{2(\alpha_1 + \alpha_2)^2}\left(\frac{n^2}{l_z^3} + \frac{m^2}{l_x^3}\right), \quad (10b)$$

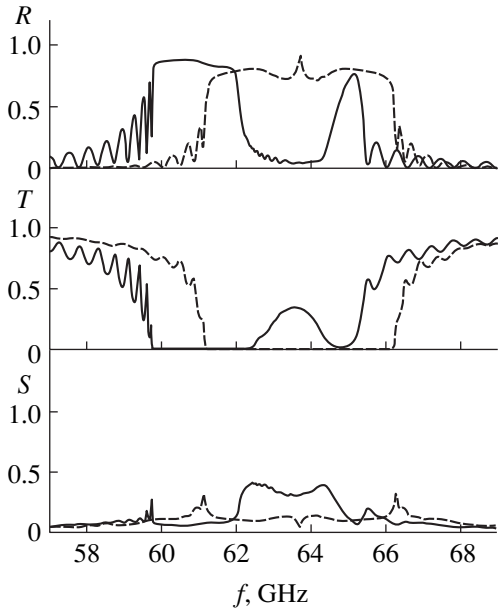

Fig. 3. Simulated frequency dependences of the reflection (R), transmission (T), and transverse scattering (S) coefficients for a plane wave incident on a planar Bragg resonator with $l_x = l_z = 25$ cm, $d = 0.33$ cm, $\alpha_1 = 0.25$ cm^{-1}, and $\alpha_2 = 0.3$ cm^{-1} (solid curves) or $\alpha_2 = 0$ (dashed curves).

and

$$\delta_{m,n} = 2\alpha_1 - \alpha_2 + \frac{\pi^2}{4(\alpha_1 - \alpha_2)}\left(\frac{n^2}{l_z^2} + \frac{m^2}{l_x^2}\right) + i\frac{\pi^2}{2(\alpha_1 - \alpha_2)^2}\left(\frac{n^2}{l_z^3} + \frac{m^2}{l_x^3}\right), \quad (10c)$$

where n and m are the longitudinal and the transverse mode indices, respectively.[1] Admittedly, the forward scattering of the forward and backward waves makes the spectrum asymmetric and shifts it toward lower frequencies (Fig. 2a) as compared to the case of an ideal resonator, for which $\alpha_2 = 0$ (Fig. 2b). With the corrugation pattern (2), the Q-factor is maximum for the modes with $n = m = 1$ and $\delta \approx \alpha_2$ or $\delta \approx -2\alpha_1 - \alpha_2$ (see Fig. 2a). For these modes, the Q value exceeds that of the fundamental mode in an ideal resonator (6), a_1 being the same. Note that pattern (2) still ensures rather high selectivity with respect to both longitudinal and transverse mode indices.

In addition to solving equation (7), the eigenmode frequencies were evaluated through simulating the external excitation of resonator modes. The results were used for interpretation of the electromagnetic data measured under "cold" conditions. Let a plane wave come to the boundary situated at $z = 0$. Then the boundary condition for the $\mathcal{A}_+$ wave is

$$\mathcal{A}_+(x, 0) = 1, \quad (11)$$

the boundary conditions for the other waves being similar to (9).

Figure 3 shows the frequency dependences of the reflection (R), transmission (T), and transverse scattering (S) coefficients, defined as

$$R = \frac{1}{l_x}\int_0^{l_x} |\mathcal{A}_-(x, 0)|^2 dx, \quad T = \frac{1}{l_x}\int_0^{l_x} |\mathcal{A}_+(x, l_z)|^2 dx, \quad S = \frac{1}{l_z}\int_0^{l_z} |\mathcal{B}_-(0, z)|^2 dz. \quad (12)$$

The simulation was carried out with the same parameter values as those of the mock-up employed for the measurements. Comparing Fig. 3 with Fig. 2 indicates that the minima of R and the maxima of T or S occur at the resonance frequencies of resonator eigenmodes. However, Fig. 3 is computed for an incident wave beam that is symmetric about the resonator axis. Being antisymmetric in the x-direction, the eigenmodes with $\delta \approx \alpha_2$ cannot be excited by such a beam, so that T is almost zero and R is larger than 0.8 in this band. The missing eigenmodes were obtained with an antisymmetric distribution of the incident wave field. At frequencies far from the Bragg resonance ($|h - \bar{h}| \gg \alpha_{1,2}$), T tends to 1, whereas R and S become negligible.

The measurements were carried out on a mock-up resonator described in [11]. It was designed as a pair of 25×25-cm plates spaced by 0.5 cm. The two-period orthogonal relief pattern was made according to (2) for $d = 0.32$ cm and $a_1 = 0.04$ cm.

We used a panoramic source operating in the range 55–80 GHz. Resonator oscillations were excited by a wide wave beam having a plane phase front. The beam was formed by a planar quasi-optical transmission line. The line included a parabolic mirror, situated between two metallic plates, and was illuminated by a 0.7×0.5-cm waveguide horn placed in the line focus. The line was fed with an $H_{1,0}$ wave from a rectangular waveguide. The output beam was a TEM wave of a planar waveguide with a 40×0.5-cm aperture. Similar transmission lines received the transmitted radiation and that transversely scattered from the resonator.

The measurements revealed two bands of effective Bragg scattering, centered at 60 and 75 GHz. In the 60-GHz band, all of the four partial TEM waves undergo scattering. The measured values of R, T, and S are shown in Fig. 4. They agree well with the simulated data (cf. Fig. 3). In particular, the curves exhibit asymmetry, and the eigenmodes are distributed asymmetrically about the Bragg frequency. The Q-factor of a (1, 1) mode measured at a frequency of 59.5 GHz was

[1] For the sake of simplicity, equation (10a) is written for the case of symmetric modes ($m = n$) and square resonators ($l_x = l_z$). Nevertheless, Fig. 2a also depicts the modes with $m \neq n$.

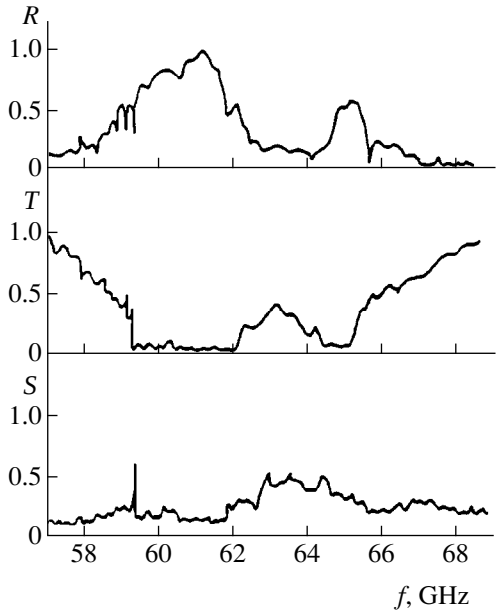

Fig. 4. Experimental results for the range 57–69 GHz (see legend to Fig. 3).

≈1500. The coupling coefficient α determined from the Bragg resonance bandwidth was somewhat larger than the computed value obtained from asymptotic formulas for shallow sine-shaped grooves. Thus, the shape of the grooves must be taken into account when computing α. A small discrepancy between theory and experiment in terms of the position of the Bragg band center and the resonator eigenfrequencies can be attributed to manufacturing defects and phase mismatch of the relief patterns.

The 75-GHz band corresponds to TEM $\longleftrightarrow$ TE_2 scattering under resonance conditions (5). Its position and width, the latter governed by α_2, were found to agree with the theory. No transversely directed radiation was detected in this band, since only the forward ($\mathcal{A}_+$) and backward ($\mathcal{A}_-$) waves are coupled there.

To sum up, our experiment confirmed the serviceability of planar Bragg resonators with corrugated surfaces and enabled us to develop a technique for measuring their characteristics under "cold" conditions. We determined position of the scattering bands and measured the frequencies and Q-factors of the resonator eigenmodes. The results agree well with the simulation data.

It is pertinent to note that a more developed technology can provide patterns where the partial wave scattering under resonance conditions (4) are realized, while extra resonances (5) are suppressed [12]. The absence of "parasitic" resonances would enhance the selectivity in the *y*-direction. An example is shown in Fig. 1c.

REFERENCES

1. A. V. Arzhannikov, V. S. Nikolaev, S. L. Sinitsky, *et al.*, in *Proceedings of the 14th FEL Conference, Kobe, Japan, 1992*, p. 214.
2. N. S. Ginzburg, N. Yu. Peskov, and A. S. Sergeev, Pis'ma Zh. Tekh. Fiz. **18**, 23 (1992) [Sov. Tech. Phys. Lett. **18**, 285 (1992)].
3. N. S. Ginzburg, N. Yu. Peskov, A. S. Sergeev, *et al.*, Nucl. Instrum. Meth. Phys. Res. A **358**, 189 (1995).
4. N. V. Agarin, A. V. Arzhannikov, V. B. Bobylev, *et al.*, in *Abstracts of the 4th Asian Symposium on FEL, Taejon, Korea, 1999*, p. 8D2.
5. N. V. Agarin, A. V. Arzhannikov, V. B. Bobylev, *et al.*, in *Proceedings of the IV International Workshop "Strong Microwaves in Plasmas," Nizhni Novgorod, Russia, 1999*, p. S24.
6. N. V. Agarin, A. V. Arzhannikov, V. B. Bobylev, *et al.*, in *Abstracts of the 21st International FEL Conference, Hamburg, Germany, 1999*, p. Mo-O-04.
7. N. F. Kovalev, I. M. Orlova, and M. I. Petelin, Izv. Vyssh. Uchebn. Zaved., Radiofiz. **11**, 783 (1968).
8. V. L. Bratman, G. G. Denisov, N. S. Ginzburg, and M. I. Petelin, IEEE J. Quant. Electron. **19**, 282 (1983).
9. G. G. Denisov and M. G. Reznikov, Izv. Vyssh. Uchebn. Zaved., Radiofiz. **25**, 562 (1982).
10. N. S. Ginzburg, N. Yu. Peskov, and A. S. Sergeev, Radiotekh. Élektron. (Moscow) **40**, 401 (1995).
11. N. Yu. Peskov, A. V. Arzhannikov, N. S. Ginzburg, *et al.*, in *Proceedings of the IV International Workshop "Strong Microwaves in Plasmas," Nizhni Novgorod, Russia, 1999*, p. S30.
12. An Yen Huan, A. V. Arzhannikov, E. V. Diankova, *et al.*, in *Abstracts of the 4th Asian Symposium on FEL, Taejon, Korea, 1999*, p. P35.

Translated by A. A. Sharshakov

Technical Physics Letters, Vol. 26, No. 4, 2000, pp. 352–353. Translated from Pis'ma v Zhurnal Tekhnicheskoĭ Fiziki, Vol. 26, No. 8, 2000, pp. 83–87.

Intermodulation Measurements in YBaCuO Films

E. A. Vopilkin, S. A. Pavlov, A. N. Panin, and A. E. Parafin

Institute of Microstructure Physics, Russian Academy of Sciences, Nizhni Novgorod, 603600 Russia

Received May 11, 1999; in final form, September 23, 1999

Abstract—A technique for measuring the intermodulation signal arising in a nonlinear high-temperature superconductor film is suggested. Using a one-port resonator, the technique significantly increases sensitivity of the measuring system as compared to that of a two-port-resonator design. Specifically, it lowers the minimum measurable power at a given magnetic field strength on the film surface. Measurements of the intermodulation signal power as a function of the input power for YBaCuO films differing in surface resistance and thickness are reported. Based on the measured data, the intermodulation characteristic magnetic field is computed. The quantity characterizes nonlinear film properties of the regardless of the measuring system employed. *© 2000 MAIK "Nauka/Interperiodica".*

Epitaxial films of high-temperature superconductors (HTSC) deposited onto low-loss substrates can serve a base for the fabrication of microwave devices, such as resonators or filters. Low surface resistance R_s of the films results in good performance of the products. However, their use at high power densities may be limited by nonlinear effects [1–5].

Nonlinearity of the HTSC films is manifested by dependence of the effective surface resistance R_{eff} on the radiation power and by features of the frequency conversion. Note that the latter features may show up at much lower powers. If two signals with the frequencies f_1 and f_2 are used in a microwave device, then the nonlinearity gives rise the so-called intermodulation signals occurring at the combination frequencies $f_{comb1} = 2f_1 - f_2$ and $f_{comb2} = 2f_2 - f_1$ in the operating band.

The parameters of a film are determined by its intrinsic and extrinsic properties. The former are the physical properties of the material, whereas the latter are related to defects concomitant with the film processing technology. Importantly, large values of the critical temperature and current and small values of R_s cannot assure that the nonlinearity is weak [1]. That is why nonlinearity characterization by special methods is essential for manufacturing.

In this study, YBaCuO films were grown on LaAlO substrates by laser evaporation. A 248-nm excimer laser produced 27-ns pulses with an energy flux density of about 10 J/cm^2 per pulse. The process went at a target–substrate distance of ≈6 cm, a growth temperature of ≈700°C, and an oxygen pressure equal to about 20 Pa (during the deposition) or air pressure (during cooling to room temperature).

The values of film parameters are given in the table. The film thickness d was measured with a DRON-4 diffractometer as described in [9]. The values of R_{eff} were measured by a parallel-plate-resonator technique [7]. The critical pinning current density j_c was determined from the remanent magnetization of the films [6].

Figure 1 shows the block diagram of the setup used to measure the intermodulation signal power P_{comb} as function of the input power P_{in}. We used a one-port LaAlO resonator placed in a copper case. The dielectric had a diameter of 8 mm, a height of 3.2 mm, a dielectric constant of about 22, and a loss tangent less than 10^{-4}. The measurements were performed for an azimuthally symmetric mode (H_{011}) with a frequency of ≈11.8 GHz. The unloaded Q-factor of the resonator was ≈10^4. Loop coupling was employed, and the fine adjustment of the coupling factor was effected with a rod at the center of the upper case lid. A stroboscopic frequency converter (FSC) received signals from the resonator (at f_1, f_2, and f_{comb1}) and a heterodyne signal (the 20th harmonic of the G1 oscillator signal). The output of FSC was connected to a spectrum analyzer (SA) via an intermediate-frequency amplifier (IFA).

For the resonator, the maximum input power of signal 1 (from S1) was about 80 mW, the magnetic field on the film surface being 160 A/m, whereas the input power of signal 2 (from S2) was fixed at 10 mW. A difference between the frequencies of the two signals was 40 kHz. The phase noise of the signal sources was –90 dB/Hz for a detuning of 40 kHz. SA offered a dynamic range of 80 dB. The measurements were performed at a bandwidth of 1 kHz. The absence of unwanted sources oper-

Table

No.	t, μm	R_{eff}, mΩ	H_{im}, kA/m	j_c, MA/cm^2
1	0.17	10	3.6	0.61
37	0.14	1.6	5.6	0.97
34	0.10	1.2	9.6	1.3
14	0.13	0.7	11	1.1

1063-7850/00/2604-0352$20.00 © 2000 MAIK "Nauka/Interperiodica"

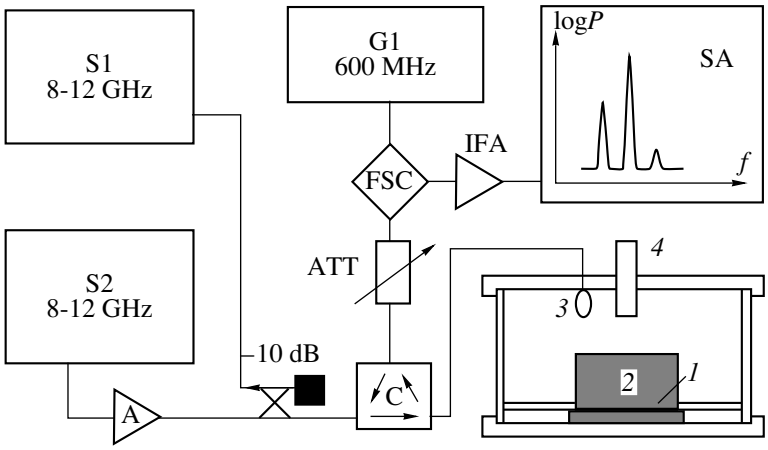

Fig. 1. Block diagram of the experimental setup: (*1*) film sample; (*2*) dielectric (LaAlO); (*3*) coupling element; (*4*) adjusting rod. Notation: A, an amplifier, ATT, attenuator, C, circulator, IFA, intermediate-frequency amplifier, G1, a G4-164 oscillator, SA, S4-74 spectrum analyzer, FSC, stroboscopic frequency converter, S1, signal source 1, and S2, signal source 2.

ating at the combination frequency was verified by replacing the film with a copper plate. The measurements were carried out in a liquid nitrogen environment.

Unfortunately, high-power pumping signals are coupled into the output path besides the signals at the combination frequencies. In this context, let us consider the factors that determine the sensitivity of the setup, namely, the minimum measurable power at a given magnetic field strength on the film surface. First, the signal from the resonator must be weak so as to avoid generating unwanted combination-frequency signals in FSC. Second, due to a nonzero linewidth at $f_{\text{comb}1}$ and $f_{\text{comb}2}$, the lowest level of the input signal is greater than zero: it was measured to be –60 dB against the input signal power at the source central frequency.

Thus, in order to increase the sensitivity, care should be taken to attenuate the pumping signal in the output path at a given magnetic field on the film surface. With a two-port resonator, this is usually achieved by raising the resonator Q over 10^6 [1, 5]. However, this approach tightens up requirements to the equipment materially. Using a one-port resonator increases the sensitivity by a factor of R (equal to the resonator reflection coefficient). The resonator thus serves as a combination frequency filter. Our setup offered $R < -20$ dB.

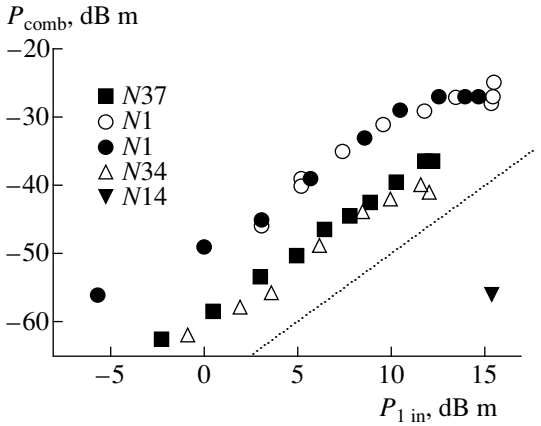

Fig. 2. Intermodulation power vs. input power at P_2 = 9.3 dB m. The dotted line depicts the dependence $P_{\text{comb}}(P_{\text{in}}) = (P_{1\text{in}})^2 P_{2\text{in}}$.

Figure 2 shows the measured dependences of P_{comb} on $P_{1\text{in}}$ for films differing in thickness and performance. Note that all films comply with the law $P_{\text{comb}} \sim (P_{1\text{in}})^2 P_{2\text{in}}$. This fact allowed us to compute the intermodulation characteristic magnetic field H_{im} suggested in [8] as characterizing nonlinearity of a film regardless of the measuring system.

This study was supported by the State Program "Current Problems of the Physics of Condensed Matter: Superconductivity," project no. 98064.

REFERENCES

1. W. Diete, M. Getta, M. Hein, *et al.*, IEEE Trans. Appl. Supercond. **5**, 1236 (1997).
2. C. Wilker, Zhi-Yan Shen, P. Pang, *et al.*, IEEE Trans. Appl. Supercond. **5**, 1665 (1995).
3. A. Lauder, C. Wilker, Zhi-Yan Shen, *et al.*, in *Proceedings of International Wires & Cable Symposium, 1994*, p. 155.
4. D. E. Oates, P. P. Nguyen, G. Dresselhaus, *et al.*, J. Supercond. **8**, 725 (1995).
5. Zhi-Yan Shen and C. Wilker, Reprinted from Microwaves RF No. 4 (l994) (Cleveland, Penton Publishing).
6. Yu. N. Nozdrin, P. P. Visheslavtzev, I. D. Tokman, *et al.*, IEEE Trans. Appl. Supercond. **5**, 1424 (1995).
7. A. Ya. Basovich, R. K. Belov, V. A. Markelov, *et al.*, J. Supercond. **5**, 1614 (1992).
8. E. A. Vopilkin, A. E. Parafin, and A. N. Reznik, Zh. Tekh. Fiz. (2000) (in press).
9. A. V. Varganov, E. A. Vopilkin, P. P. Vysheslavtsev, *et al.*, Pis'ma Zh. Éksp. Teor. Fiz. **63**, 608 (1996) [JETP Lett. **63**, 644 (1996)].

Translated by A. A. Sharshakov

Technical Physics Letters, Vol. 26, No. 4, 2000, pp. 354–356. Translated from Pis'ma v Zhurnal Tekhnicheskoĭ Fiziki, Vol. 26, No. 8, 2000, pp. 88–94.

Effect of Synthesis Conditions on the Phase Composition and Critical Current Density of $Bi_{1.6}Pb_{0.4}Sr_{2-x}K_xCa_2Cu_3F_{0.8}O_y$

V. V. Petrashko, B. V. Novysh, N. A. Prytkova, E. M. Gololobov, and L. A. Kurochkin

Institute of Solid State and Semiconductor Physics, National Academy of Sciences of Belarus, Minsk, Belarus

Received December 21, 1999

Abstract—Effects of the temperature–time schedule on the phase composition, critical current density j_c, critical temperature T_c, and electric resistance in the normal state (ρ) of the samples of $Bi_{1.6}Pb_{0.4}Sr_{2-x}K_xCa_2Cu_3F_{0.8}O_y$ ($x = 0$ or 0.02) compositions were studied by X-ray diffraction analysis and by measuring resistances and current–voltage characteristics of the samples. The values of j_c = of 583.6 A/cm^2 (at 77.4 K) and $T_c(R = 0) = 107.1$ K were obtained in the samples with $x = 0.02$ upon partial fusion. In order to obtain high j_c values, the samples must be synthesized (sintered) prior to the fusion stage. © *2000 MAIK "Nauka/Interperiodica".*

Effects of the partial fluorine substitution for oxygen on the structure and superconducting properties of the (Bi, Pb)-2223 compositions studied in [1–6] showed that fluorine additives decrease the temperatures of melting and formation of the 2223 phase, accelerate the crystallization and growth of this phase, modify the electron structure and chemical bonding, and markedly improve the superconducting properties of materials belonging to the (Bi, Pb)–Sr–Ca–Cu–O system. It was found that simultaneous introduction of the potassium and fluorine additives into this composition increases the yield of the 2223 phase to even greater extent [7].

As is known, one of the major problems restricting the application of some polycrystalline bulk high-temperature superconductor (HTSC) materials is their low critical current densities (j_c). In this context, systematic investigations aimed at establishing optimum parameters for the synthesis of materials with high j_c values are of current importance in HTSC physics and technology.

Previously we have synthesized HTSC samples with a base composition of $Bi_{1.6}Pb_{0.4}Sr_{1.98}K_{0.02}Ca_2Cu_3F_{0.8}O_y$ possessing $T_c(R = 0) = 112.8$ K and studied stability of this phase in the temperature interval from 845 to 890°C [8].

The purpose of this work was to study effects of the temperature–time process schedule on the phase composition, j_c, T_c, and electric resistance in the normal state (ρ) of the samples of $Bi_{1.6}P_{0.4}Sr_{2-x}K_xCa_2Cu_3F_{0.8}O_y$ ($x = 0$ or 0.02) compositions. The samples were prepared by solid state synthesis in air using the special-purity grade powders of Bi_2O_3, PbO, $SrCO_3$, $CaCO_3$, K_2CO_3, and PbF_2. The initial powders were thoroughly mixed, triturated, and calcined for 16 h at 750°C. The calcined mixtures were triturated and used to press disks with a diameter of 12.8 mm. This was followed by synthesis in one of the five standard regimes according to the following schedules:

(A) 800°C, 56 h + 830.5°C, 24 h + 835°C, 120 h;

(B) (A) + 836.5°C, 70.5 h;

(C) 811°C, 48 h + 835.5°C, 120 h;

(D) = (C) + 836°C, 68 h + 849°C, 2 min (partial fusion);

(E) = (C) + 860°C, 16 min + at 834.5°C, 97.5 h (annealing).

The samples treated in regimes A–E were crushed and triturated upon synthesis, after which the disks were pressed anew and subjected to annealing in air at the corresponding temperatures, followed by slow cooling with furnace from the temperature of synthesis to room temperature.

The phase compositions of the synthesized materials were studied, using the samples triturated at room temperature, by the X-ray diffraction measurements on a DRON-3 diffractometer (CuK_α radiation). The superconducting phases were identified and determined by measuring the intensities of reflections (0010) and (008) corresponding to the 2223 and 2212 phases, respectively [9]. The superconducting properties were evaluated by measuring the sample resistances and current–voltage (I–V) characteristics at various temperatures. The temperature dependence of the sample resistance and the critical current density at liquid nitrogen temperature were measured by the dc four-point-probe

1063-7850/00/2604-0354$20.00 © 2000 MAIK "Nauka/Interperiodica"

technique. The electric field criterion for the j_c measurements was selected at 1 μV/cm.

Analysis of the X-ray diffraction patterns for the samples synthesized at 800°C/56 h and 830.5°C/24 h (regime A) and 811°C/48 h (regime C) showed that the main superconducting phase in these samples is 2212. Also present as impurity phases are the small amounts of 2201, Ca_2PbO_4, and $(Sr, Ca)_2CuO_3$. Traces of the superconducting 2223 phase were found only in the samples annealed at 830.5°C for 24 h. These samples had the critical temperatures $T_c(R= 0) = 84.2$ K ($x = 0$), 88.5 K ($x = 0.02$) and the critical current densities $j_c = 0$ for both compositions.

A significant increase in the 2223 phase content and in the superconducting properties was observed in the samples synthesized at higher temperatures (see table). According to the X-ray diffraction data, all samples synthesized in the regimes A–E possess multiphase structures comprising predominantly the two main superconducting phases, 2223 (dominating) and 2212, and a small amount of impurities representing the 2201 phase and the compounds Ca_2PbO_4, $(Sr, Ca)_2CuO_3$, and $(Ca, Sr)_2PbO_4$. A minimum amount of $(Sr, Ca)_2CuO_3$ was found in the samples synthesized in regime E. However, these samples exhibited a maximum content of the 2212 phase among all the samples studied.

In the samples containing potassium, the content of the HTSC phase (2223) and the j_c value increased, and the amount of the 2212 phase decreased, as compared to those in the samples with $x = 0$. The only exclusion was for the samples obtained in regime E, where content of the 2223 phase was somewhat lower in the samples with potassium. We believe that this is related to the fact that the samples containing both potassium and fluorine possess a lower melting temperature as compared to that of the samples containing fluorine alone. As a result, the treatment at 860°C leads to a more intensive decomposition of the 2223 phase in the former samples.

The maximum values of the critical current density ($j_c = 583.6$ A/cm^2 at 77.4 K) and critical temperature ($T_c(R = 0) = 107.1$ K) were observed for the samples with potassium synthesized in regime D. These samples still contain about 6.3% of the 2212 phase and possess a comparatively low electric resistance in the normal state (see figure). Here, the samples free of potassium are characterized by the same $T_c(R = 0) = 107.1$ K, but exhibit a somewhat lower values of the critical current density ($j_c = 320$ A/cm^2). A comparison of the data for regimes B and D indicates that a short-time increase in the synthesis temperature (to 849°C) favorably affects both the phase composition and the superconducting properties of the final material.

It should be noted that the samples synthesized in regime D were preliminarily sintered for 18 h at 836°C. In the course of sintering, some grains of the superconducting phases grow together at the sites of contact to form a spatial structure. The short-time treatment of the samples at 849°C leads to the appearance of a small amount of liquid phase, (as noted above, the presence of fluorine and potassium decreases the melting temperature [2, 10], so that the temperature $T = 849$°C falls within the region of existence of the liquid phase [11]). As a result, the area of contact between the grains increases (due to liquid phase filling the intergranular space) and the subsequent sintering at 836.5°C is

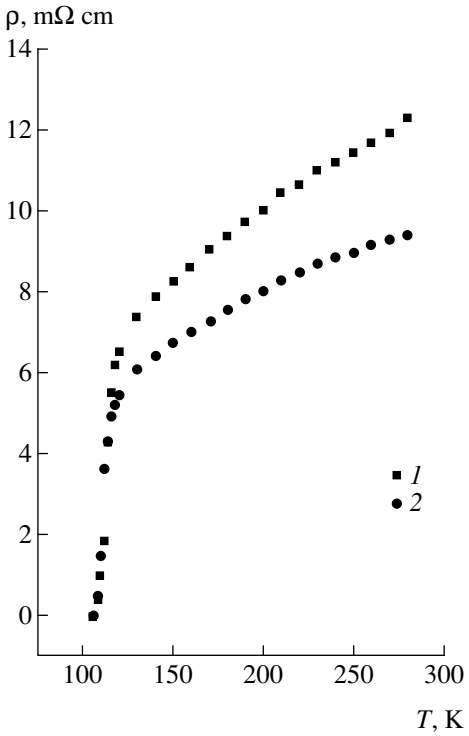

Temperature variation of the electric resistance of the $Bi_{1.6}Pb_{0.4}Sr_{2-x}K_xCa_2Cu_3F_{0.8}O_y$ samples with $x = 0$ (*1*) and 0.02 (*2*).

Phase structure and superconducting characteristics of the samples $Bi_{1.6}Pb_{0.4}Sr_{2-x}K_xCa_2Cu_3F_{0.8}O_y$ ($x = 0$ or 0.02) synthesized in various regimes

Regime	x	Phase 2223, %	Phase 2212, %	$T_c(R = 0)$, K	j_c(77.4 K), A/cm^2
A	0.0	83.0	17.0	105.8	3.1
	0.02	89.6	10.4	110.5	6.0
B	0.0	90.5	9.5	104.0	17.5
	0.02	90.8	9.2	101.3	26.9
C	0.0	91.5	8.5	93.0	1.5
	0.02	93.0	7.0	101.0	2.7
D	0.0	92.8	7.2	107.1	320.0
	0.02	93.7	6.3	107.1	583.6
E	0.0	61.9	39.1	102.7	4.9
	0.02	55.4	44.6	100.5	3.5

accompanied by intensive formation of the 2223 phase with improved contact between the superconducting phase grains. We believe that this is just what accounts for the increase in j_c and a decrease in the electric resistance in the normal state. The increase in the temperature of sintering to 860°C without preliminary sintering at a lower temperature (regime E) leads to partial decomposition of the 2223 phase into 2212 and 2201 phases, and even the following annealing at 834.5°C for 97.5 h did not improve the phase composition. Partial irreversible degradation of the 2223 phase probably accounts for the low j_c values in these samples.

The temperature variation of the electric resistance of samples synthesized in regime D is presented in the figure. As seen, the $\rho(T)$ curves exhibit a superconducting transition in the region of 110 K, which is related to the presence of the 2223 phase with $T_c(R = 0) = 107.1$ K in both compositions studied. The sample with potassium possesses a somewhat lower resistance in the normal state as compared to the sample with $x = 0$. This indicates that adding potassium improves the intergranular contacts, which probably also favorably affects the superconducting properties.

Thus, the results of our investigations showed that the critical current density j_c of high-temperature superconductors of the $Bi_{1.6}Pb_{0.4}Sr_{2-x}K_xCa_2Cu_3F_{0.8}O_y$ ($x = 0$ or 0.02) compositions are very sensitive with respect to the preparation conditions. The values of j_c = of 583.6 A/cm^2 (at 77.4 K) were obtained in the samples with potassium ($x = 0.02$) upon the synthesis at 836°C followed by short-time partial fusion. The samples without potassium ($x = 0$), synthesized and studied under the same conditions, are characterized by j_c = 320 A/cm^2. Potassium added to $x = 0.02$ favors the growth of the 2223 phase, increases the critical current density, and decreases the electric resistance of samples in the normal state. In order to obtain high j_c values, the samples must be synthesized (sintered) prior to the partial fusion stage.

The work was supported by the Belarus Republic Foundation for Basic Research.

REFERENCES

1. X. H. Gao, S. F. Jiang, D. Gao, *et al.*, Physica C **245**, 66 (1995).
2. X. G. Wang, P. Y. Hu, Z. M. Huang, *et al.*, Physica C **233**, 327 (1994).
3. S. Horiuchi, K. Shoda, H. Nozaki, *et al.*, Jpn. J. Appl. Phys. **28**, L621 (1989).
4. Z. T. Nang, S. J. Wang, and X. H. Gao, Phys. Rev. B **50**, 3209 (1994).
5. S. Y. Lee, S. Suehara, and S. Horiuchi, Physica C **185-189**, 477 (1991).
6. X. H. Gao, X. L. Wu, and H. Yan, Mod. Phys. Lett. B **4**, 137 (1990).
7. V. V. Petrashko, N. D. Zhigadlo, B. V. Novysh, *et al.*, Pis'ma Zh. Tekh. Fiz. **24**, 8 (1998) [Tech. Phys. Lett. **24**, 374 (1998)].
8. N. D. Zhigadlo, V. V. Petrashko, Yu. A. Semenenko, and N. A. Prytkova, Pis'ma Zh. Tekh. Fiz. **23**, 30 (1997) [Tech. Phys. Lett. **23**, 548 (1997)].
9. Y. E. Lu, X. Z. Wu, Q. J. Dong, *et al.*, Phys. Status Solidi A **141**, 175 (1994).
10. T. Honda, T. Wada, M. Sakai, *et al.*, Jpn. J. Appl. Phys. **27**, L545 (1988).
11. M. P. Chudzik, B. J. Polizin, R. Thayer, *et al.*, IEEE Trans. Appl. Supercond. **7**, 2102 (1997).

Translated by P. Pozdeev